Dissertation zur Erlangung des Doktorgrades
der Fakultät für Chemie und Pharmazie
der Ludwig-Maximilians-Universität München

Structural basis of regulatory ribosome arrest by VemP and rescue of aberrant translational stalling by Vms1

Ting Su
aus
Shanghai, China

2021

Erklärung

Diese Dissertation wurde im Sinne von § 7 der Promotionsordnung vom 28. November 2011 von Herrn Prof. Dr. Roland Beckmann betreut.

Eidesstattliche Versicherung

Diese Dissertation wurde eigenständig und ohne unerlaubte Hilfe erarbeitet.

Hallbergmoos, 12.04.2021

Ting Su

Dissertation eingereicht am: 14.12.2020

1. Gutachter: Prof. Dr. Roland Beckmann

2. Gutachter: Prof. Dr. Daniel N. Wilson

Mündliche Prüfung am: 02.02.2021

List of Publications

"Structure and function of Vms1 and Arb1 in RQC and mitochondrial proteome homeostasis"

Su T*, Izawa T*, Thoms M, Yamashita Y, Cheng J, Berninghausen O, Hartl FU, Inada T, Neupert W** and Beckmann R**

Published in **Nature** 570:538–542. 2019. doi:10.1038/s41586-019-1307-z

"Folding pathway of an Ig domain is conserved on and off the ribosome"

Tian P*, Steward A*, Kudva R*, **Su T***, Shilling PJ, Nickson AA, Hollins JJ, Beckmann R, Heijne G von**, Clarke J**, Best RB**

Published in **Proc National Acad Sci** 115:201810523. 2018. doi:10.1073/pnas.1810523115

"The force-sensing peptide VemP employs extreme compaction and secondary structure formation to induce ribosomal stalling"

Su T, Cheng J, Sohmen D, Hedman R, Berninghausen O, Heijne G von, Wilson DN**, Beckmann R**

Published in **eLife** 6:e25642. 2017. doi:10.7554/elife.25642

* These authors contribute equally to the work
** Corresponding Author

Summary

Regulation of translation directly controls gene expression levels from mRNA to protein in the translation cycle steps. Ribosome arrest peptides (RAPs) are often conditional modulators interacting with the ribosomal tunnel and induce translational stalling to regulate downstream gene expression in cis to fulfill real-time cellular needs. The ribosomal tunnel also provides a protected environment for initial protein folding. This dissertation's first publication presents a 2.9 Å cryo-electron microscopy structure of a ribosome stalled during translation of the extremely compacted VemP nascent chain. The nascent chain forms two α-helices connected by an α-turn and a loop, enabling a total of 37 amino acids to be observed within the first 50–55 Å of the ribosomal tunnel.

The structure reveals how α-helix formation directly within the peptidyltransferase center (PTC) of the ribosome interferes with aminoacyl-tRNA (A-tRNA) accommodation, suggesting that for canonical translation, a significant role of the ribosomal tunnel is to prevent excessive secondary structure formation that can interfere with the peptidyltransferase activity of the ribosome. On the other hand, secondary structure formation at the PTC could also be used by the ribosome for specific nascent proteins like RAPs to modulate the rate of translation, which could have significant downstream consequences for co-translational protein targeting and folding.

Relief of VemP-mediated ribosome stalling is proposed to result from the translocon pulling force exerted on VemP nascent chain's N-terminal signal sequence. For VemP, force application would inevitably prevent the formation of the extensive secondary structure during translation or lead to an unraveling of any secondary structure that does form within the tunnel, thereby eventually allowing the sterical transition into the induced conformation of the PTC. This work obtained novel insights into the underlying mechanisms of RAP-mediated ribosome force sensing.

A translating ribosome can also be stalled on the mRNA owing to defective translational components such as non-stop/no-go mRNAs. To maintain ribosome and protein homeostasis, the ribosome-associated quality control (RQC) system has evolved to rescue the stalled ribosome and release the incomplete nascent protein for degradation through disassembling the translation machinery in eukaryotic cells. After dissociation of ribosomes, the stalled tRNA-bound peptide remains associated with the 60S subunit and extended by Rqc2 by adding C-terminal alanyl and threonyl residues (CAT tails), whereas Vms1 catalyzes cleavage and release of the peptidyl-tRNA before or after addition of CAT tails. In doing so, Vms1 counteracts CAT-tailing of nuclear-encoded mitochondrial proteins that otherwise drive aggregation and compromise mitochondrial and cellular homeostasis.

This dissertation's second publication presents structural and functional insights into the interaction of Saccharomyces cerevisiae Vms1 with 60S subunits in pre- and post-peptidyl-tRNA cleavage states. Vms1 binds to 60S subunits with its Vms1-like release factor 1 (VLRF1), zinc finger, and ankyrin domains. VLRF1 overlaps with the Rqc2 A-tRNA position and interacts with the ribosomal A-site, projecting its catalytic GSQ motif towards the CCA end of the tRNA, its Y285 residue dislodging the tRNA base 73 for nucleolytic cleavage. Moreover, in the pre-state, ABCF-type ATPase Arb1 was found in the ribosomal E-site, which stabilizes the delocalized base 73 of the peptidyl-tRNA and stimulates Vms1-dependent tRNA cleavage. These structural analyses provided mechanistic insights into the interplay of the RQC factors Vms1, Rqc2, and Arb1 and their role in protecting mitochondria from the aggregation of toxic proteins.

Contents

Chapter 1

Introduction

Proteins are macromolecules consisting of long chains of amino acid residues. They are involved in every biological process within organisms, including providing structure to cells, catalyzing reactions, and communicating chemical signals.

1.1 Translation and Ribosome

Translation is the process of biological protein synthesis from the genetic information of a messenger RNA (mRNA) template. An mRNA is a sequence of nucleotide triplets known as codons, determining when translation should start and terminate, as well as the order of amino acids to be added to the nascent polypeptide. Ribosomes are the macromolecular machines to decode mRNA information into the polypeptide chain by catalyzing peptide bonds between amino acids.

Ribosomes are comprised of ribosomal RNA (rRNA) and ribosomal proteins (r-proteins), and each ribosome consists of a small and a large subunit. The small subunit contains the mRNA tunnel and the decoding center to assign codon matching transfer RNAs (tRNAs) charged with particular amino acids. The large subunit possesses the peptidyl-transferase center (PTC) that forms peptide bonds, and harbors the ribosomal tunnel elongating from PTC to the solvent side of the subunit for the nascent polypeptide chain to pass through. The space between the small and large subunits comprises three tRNA binding sites, namely aminoacyl, peptidyl, and exit sites (A-, P-, and E-sites).

The core features and functions of ribosomes are conserved through kingdoms of lives. However, through evolution, ribosomes layered more rRNA and r-proteins upon the core architecture and therefore became larger. The molecular weight of an *Escherichia coli* (*E. coli*) ribosome is 2.3 MDa, while it is 3.3 MDa for yeast. Based on the sedimentation coefficient in Svedberg units (S), bacterial cells contain 70S formed by the small subunit 30S and the large subunit 50S, whereas eukaryotic cells have 80S formed by the small subunit 40S and large subunit 60S (Wilson and Cate, 2012; Melnikov et al., 2012). Eukaryotic ribosomes contain extra rRNAs expanding like "tentacles," known as expansion segments (ES). In particular, ES27 in *Saccharomyces cerevisiae* has been shown to adopt in two distinct conformations and can interact with factors binding to the exit of the ribosomal tunnel (Beckmann et al., 2001; Knorr et al., 2019).

1.2 Translation cycle

Translation of mRNA to polypeptides by the ribosome is a highly coordinated cycle, which can be divided into four steps: initiation, elongation, termination, and recycling.

1.2.1 Initiation

Despite broad conservation of the core mechanisms for translational machinery through kingdoms of lives, translation initiation is distinct in prokaryotes and eukaryotes due to the distinct cell partition. In prokaryotes, as no nucleus to segregate the transcription and translation, ribosomes can initiate co-transcriptionally, i.e., as long as the start sites in an mRNA are available (Gualerzi and Pon, 2015; Buskirk and Green, 2017). By contrast, eukaryotic ribosomes only engage with completed mRNAs possessing a cap and a poly-A tail. In bacteria, three initiation factors (IFs), IF1, IF2, and IF3, together with the Shine Dalgarno (SD) sequence locating upstream of the start codon (Shine and Dalgarno, 1974), establish base-pair interactions with the anti-SD

sequence on the 16S rRNA to accommodate the start codon in the P-site (Kaminishi et al., 2007; Korostelev et al., 2007). On the other hand, eukaryotes form a 43S preinitiation complex to bind the cap feature at the 5′-end of eukaryotic mRNA and scan from 5′ to 3′ until reaching the start codon. The preinitiation complex consists of at least twelve IFs, the small subunit, and the initiator tRNA (Met-tRNAi) (Jackson, Hellen, and Pestova, 2010). When the start codon is in place, the large subunit joins, and elongation starts upon release of IFs (Jackson, Hellen, and Pestova, 2010).

1.2.2 Elongation

During elongation, the ribosome translates the mRNA continuously from 5′ to 3′ with elongation factors (EFs). EF-Tu in bacteria or its homolog, eukaryotic EF1 (eEF1), delivers aminoacyl-tRNAs (aa-tRNA) to the A-site (Noble and Song, 2008; Agirrezabala and Frank, 2009; Dever and Green, 2012). When a cognate tRNA is bound to the mRNA codon at the A-site, EF-Tu/eEF1 hydrolyses guanosine triphosphate (GTP) to dissociate from the aa-tRNA, allowing the tRNA to accommodate at the A-site. Next, the ribosome transfers the nascent chain to the aa-tRNA by forming a peptide bond at the PTC. Subsequently, EF-G in bacteria or eEF2 in eukaryotes binds to the ribosome and translocates the mRNA by one codon, causing the current P-site deacylated tRNA to move to the E-site and the A-site peptidyl-tRNA to the P-site (Dever and Green, 2012). This translocation is a dynamic process (Blanchard et al., 2004): a. the tRNAs move with respect to the large subunit resulting in A/P and P/E hybrid states (the first letter indicates the respective position of the tRNA on the small subunit and the latter indicates the large subunit); b. this hybrid states is coupled to the rotation of the ribosome subunits relative to one another, and EF-G/eEF2 preferentially binds to the rotated ribosome (Frank and Agrawal, 2000; Dever and Green, 2012). After EF-G/eEF2 hydrolyses GTP and leaves the ribosome, the A-site is vacant again for the next aa-tRNA to bind (Noller et al., 2002). This elongation cycle is repeated until a stop codon is reached to terminate the translation.

1.2.3 Termination

When the signal of translation termination, a stop codon, reaches the A-site, it is recognized by a class-I release factor (RF) instead of any tRNA to release the nascent chain from the ribosome (Korostelev et al., 2008; Weixlbaumer et al., 2008; Dever and Green, 2012; Preis et al., 2014; Brown et al., 2015; Matheisl et al., 2015). Although the three standard stop codons, UAA, UAG, and UGA, are universal through kingdoms of lives, bacteria and eukaryotes possess structurally unrelated class-I RFs. Bacterial RF1 is responsible for recognizing UAA and UAG, and RF2 recognizes UAA and UGA, whereas eukaryotic RF1 (eRF1) can recognize all three stop codons. Studies have shown that eRF1 recognizes a quadruplet codon, contributing to forming a UNR-type U-tern for the N-terminus of eRF1 to recognize (Matheisl et al., 2015; Brown et al., 2015). Despite the structural distinction, RF1/RF2 and eRF1 all display a universally conserved GGQ motif that precisely positions one water molecule at the PTC, hydrolyzing the peptidyl-tRNA ester bond by a nucleophilic attack, and thus releasing the nascent chain from the ribosome (Song et al., 2000; Kisselev, Ehrenberg, and Frolova, 2003; Korostelev, 2011). Apart from class-I RFs, various class-II RFs are also needed to assist termination. Bacterial RF3 releases RF1/RF2 from the ribosome (Zavialov et al., 2002), while eukaryotic RF2 (eRF2) delivers eRF1 to the ribosome and promotes its activity (Preis et al., 2014; Shao and Hegde, 2016).

1.2.4 Recycling

After the release of NC, the ribosome needs to be recycled into subunits for the next round of translation. In bacteria, the ribosome recycling factor (RRF) and EF-G split the post-termination complex, a ribosome bound to the mRNA and a deacetylated tRNA in the P-site, into the 50S and a 30S-tRNA-mRNA complex, followed by IF3 disassociating the tRNA and mRNA off the 30S (Zavialov et al., 2002; Peske, Rodnina, and Wintermeyer, 2005). In eukaryotes, however, termination is coupled with ribosome recycling through the combined action of the splitting factor

ABCE1 and eRF1 (Pisarev, Hellen, and Pestova, 2007; Becker et al., 2012; Franckenberg, Becker, and Beckmann, 2012). ABCE1 is an adenosine triphosphate (ATP)-binding cassette sub-family E (ABCE)-type ATPase with two nucleotide-binding domains (NBDs) linked by a domain containing a conserved iron-sulfur cluster (FeS) (Karcher, Schele, and Hopfner, 2008). Upon binding to the termination complex, ribosome bound to the mRNA, a peptidyl-tRNA in the P-site, and eRF1 in the A-site, ABCE1 hydrolyzes ATP to close the NBDs for pushing the FeS domain into the inter-subunit cleft, thereby splitting the 80S (Becker et al., 2012; Preis et al., 2014; Heuer et al., 2017).

1.3 Ribosome arrest peptides (RAPs)

1.3.1 *Cis*-regulatory elements of translation

Regulation of translation directly controls gene expression levels from mRNA to protein in the translation cycle steps. Increasing number of RAPs often encoded in upstream open reading frames (uORF) or mRNA 5' leaders have been identified to be modulators interfering with ribosomes to adjust their downstream gene expression in *cis* throughout kingdoms of lives (Lovett and Rogers, 1996; Wilson and Beckmann, 2011; Cruz-Vera et al., 2011; Ito and Chiba, 2013; Wethmar, 2014; Wilson, Arenz, and Beckmann, 2016)

An elongating RAP passing through the ribosomal tunnel conditionally or naturally interacts with critical components in the tunnel to induce the ribosome stalling on the RAP mRNA. A stalling ribosome's position on the mRNA is usually precise to the codon level, thereby accurately triggering a consequence affecting the translation of the following gene (Ito and Chiba, 2013). In bacteria, a RAP-stalled ribosome typically upregulates the downstream gene expression. One classic approach to achieve this is that such stalled ribosome, by its physical presence, alters the mRNA secondary structure, thereby exposing the downstream gene's SD sequence to other

free ribosomes (Ito and Chiba, 2013). When the stalling is relieved upon changing conditions, the canonical translation cycle ensues, i.e., ribosomes rapidly leave the mRNA after translating the RAP, leading to the fast refolding of the mRNA, and thus repressing the following gene's expression due to the mostly hidden SD sequence (Ito and Chiba, 2013).

From the perspective of the conditions to induce/release ribosome stalling, RAPs, together with the ribosomes, can be seen to work as sensors responding to distinct cues. According to the cue types, RAPs can be divided into:

1. small molecule sensors, such as the tryptophan sensor TnaC (Seidelt et al., 2009; Gong and Yanofsky, 2001; Gong and Yanofsky, 2002; Bischoff, Berninghausen, and Beckmann, 2014; Wilson, Arenz, and Beckmann, 2016) and the antibiotic sensors (Ramu, Mankin, and Vazquez-Laslop, 2009), ErmBL (Shivakumar et al., 1980; Horinouchi and Weisblum, 1980; Arenz et al., 2016) and ErmCL (Vazquez-Laslop, Thum, and Mankin, 2008; Arenz et al., 2014; Johansson et al., 2014; Wilson, Arenz, and Beckmann, 2016);

2. mechanical force sensors, SecM (Nakatogawa and Ito, 2001; Nakatogawa and Ito, 2002; Gao et al., 2015), MifM (Chiba, Lamsa, and Pogliano, 2009; Chiba et al., 2011; Sohmen et al., 2015; Wilson, Arenz, and Beckmann, 2016), and the recently identified VemP (Ishii et al., 2015);

3. and no relieving non-sensors like the viral RAP hCMV (Degnin et al., 1993; Bhushan et al., 2010; Matheisl et al., 2015; Wilson, Arenz, and Beckmann, 2016).

The force sensors SecM and VemP are both destined to be exported by Sec-mediated protein secretion (SecA for SecM and SecDF for VemP). When the membrane-associated Sec machinery applies a pulling force to their nascent polypeptide chain, the translation operates canonically. However, when there is a lack of force, they stall the ribosome to allow their downstream motor gene (SecA for SecM and SecDF2 for VemP) to be expressed (McNicholas, Salavati, and Oliver, 1997; Ishii et al., 2015) and resume the translation upon sensing the presence of force again (Butkus, Prundeanu, and Oliver, 2003; Gumbart et al., 2012; Ismail et al., 2012). Similarly, MifM

is destined to be integrated into the membrane by the membrane protein insertase YidC1 or YidC2, and induces YidC2 expression when sensing the absence of force (Chiba et al., 2011).

More RAP sequences are being discovered in nature may indicate that *cis*-regulation of translation is commonly utilized by cells to respond to changes in the intracellular or extracellular environment. Along those lines, the ribosomal tunnel is proven not to be a passive conduit for a nascent chain to pass through but provides a framework to modulate the translation rate directly and rapidly, especially compared to the transcriptional regulation.

The ribosomal tunnel is approximately 100 Angstroms (Å) in length and 10 to 20 Å in diameter; starting from the PTC, it constricts around the middle region (constriction site) and becomes broad at the tunnel exit (vestibule). At the PTC, critical bases such as U2585 and U2506 (*E. coli* numbering) are often stabilized in the uninduced state by RAPs upon stalling (Ito and Chiba, 2013; Wilson, Arenz, and Beckmann, 2016). In the interior, the tunnel's surface consists mainly of rRNA, but residues from uL4 and uL22 also contribute as key discriminators at the constriction site (Ito and Chiba, 2013; Wilson, Arenz, and Beckmann, 2016). Although the inner surface is largely hydrophilic and uncharged, RAPs can usually form critical interactions to strengthen the stalling, mainly between the PTC and the constriction site. Notably, MifM stalls ribosomes in *Bacillus subtilis* (*B. subtilis*) but not in *E. coli*, demonstrating a species-sensitive regulatory mechanism fine-tuned by one single amino acid within uL22 (Sohmen et al., 2015). Apart from the vestibule possessing space for small domains to fold, the rest of the ribosomal tunnel, especially the constriction site, has been considered not allowing folds larger than helices to form (Voss et al., 2006).

VemP (*Vibrio* export monitoring polypeptide) is one of the most recently discovered force-sensing arrest peptides allowing *Vibrio alginolyticus* (*V. alginolyticus*) to adapt to salinity changes by modulating the expression of SecDF2, the components of the Sec machinery (Ishii et al., 2015). *V. alginolyticus* has two paralogs

of SecDF (SecDF1 and SecDF2) to enhance protein export in cooperation with the SecYEG translocon. In Na^+-rich environments, V. alginolyticus utilizes the Na^+-dependent SecDF1, whereas, in Na^+-limiting environments, it switches to the Na^+-independent SecDF2. The VemP stalling activity facilitates this switch. In Na^+-rich environments, VemP is targeted by its signal sequence to the SecDF1-SecYEG translocon. The force applied to VemP during translocation prevents VemP-dependent ribosome stalling, and under such conditions, the expression of SecDF2 is repressed. In Na^+-limiting environments, however, the inactive SecDF1-SecYEG translocon cannot translocate VemP. The absence of force on the VemP nascent chain then leads to ribosome stalling and induces the expression of Na^+-independent SecDF2 (Ishii et al., 2015).

In comparing the identified amino acid residues contributing to the ribosome stalling, VemP has the largest counts for crucial residues: 17 amino acid residues, versus, for instance, nine for *E. coli* SecM, five for *Mannheimia succiniciproducens* SecM, and ten for *B. subtilis* MifM (Ishii et al., 2015). However, the mechanisms of how VemP senses force and why needing the longest RAP stretch is unknown.

1.3.2 Aim of the Publication 1

In this thesis, the aim was to use cryo-electron microscopy to solve the structure of the VemP-stalled ribosome complex at the atomic level to gain novel insights into the underlying mechanisms of RAP-mediated ribosome force sensing.

1.4 Ribosome-associated protein quality control (RQC)

1.4.1 Saving cells from aberrant stalling of translation

A translating ribosome can be stalled on the mRNA owing to defective translational components such as non-stop/no-go mRNAs (Brandman and Hegde, 2016; Joazeiro, 2015). To maintain ribosome and protein homeostasis, mRNA surveillance

and RQC systems have evolved to degrade the faulty mRNA, rescue the stalled ribosome and release the incomplete nascent protein for degradation.

Recent work showed that recognizing such an aberrant stall due is initiated by ribosome collision, which initiates quality control pathways. In yeast, stalled ribosomes can be dissociated into 60S and 40S subunits by Hbs1 (Hbs1L and Gtpbp2 in mammals) and Dom34 (Pelota in mammals) in concert with the ABC-ATPase ABCE1 (Shoemaker, Eyler, and Green, 2010; Pisareva et al., 2011; Becker et al., 2012; Tsuboi et al., 2012). After splitting, the peptidyl-tRNA remains associated with the 60S subunit to which the RQC components Rqc1, Ltn1, Rqc2 (Tae2), and Cdc48 bind. Ltn1 (Listerin) is an E3 ligase and ubiquitylates the faulty polypeptides as they emerge from the ribosomal tunnel exit (Bengtson and Joazeiro, 2010). The AAA-ATPase Cdc48 functions in extracting the stalled polypeptides from the ribosome and delivers them to the ubiquitin-proteasome system (UPS) for degradation (Verma et al., 2013). Rqc1 is involved in ubiquitylation and delivery to the UPS, and Rqc2 stabilizes Ltn1 on the 60S subunit (Brandman et al., 2012; Defenouillère et al., 2013; Lyumkis et al., 2014; Shao et al., 2015; Shen et al., 2015). The primary function of Rqc2, however, is its ability to elongate the nascent peptide chains on the 60S subunit by the addition of alanyl and threonyl residues of the stalled polypeptide chains, so-called CAT tails, by an mRNA independent mechanism (Shen et al., 2015). The role of Rqc2 is only incompletely understood, particularly the process of elongating the peptidyl chain. One function of this elongation is to expose lysine residues at the ribosomal tunnel exit to enable their ubiquitylation and thereby facilitate UPS-mediated degradation (Kostova et al., 2017).

Notably, CAT-tails' presence can cause aggregation of the released peptides and other proteins in the cytosol and mitochondria (Choe et al., 2016; Defenouillère et al., 2016; Yonashiro et al., 2016; Izawa et al., 2017). In contrast to cytosolic proteins, however, clearance of stalled nuclear-encoded mitochondrial proteins is confounded by the fact that their transport across the mitochondrial membranes can

proceed co-translationally, which occurs preferentially when the translation is retarded or stalled. Consequently, ribosomes accumulate at the mitochondrial surface, and the stalled mitochondrial polypeptides tend to be protected from ubiquitylation by Ltn1, thereby escaping proteasomal degradation. This favors CAT-tailing of these proteins by Rqc2, which, once imported, form highly toxic aggregates within the mitochondria: Co-aggregation and sequestration of critical mitochondrial chaperones results in defective assembly of respiratory chain complexes and mitochondrial dysfunction (Izawa et al., 2017).

The protein Vms1 (valosin-containing protein/Cdc48-associated mitochondrial stress-responsive 1) was shown to have a protective role in mitochondrial homeostasis. Vms1 was originally described as a cytosolic protein that interacts with Cdc48 and associates with mitochondria upon oxidative stress and the endoplasmic reticulum (Heo et al., 2010; Tran, Tomsic, and Brodsky, 2011; Nielson et al., 2017). Its deletion was observed to cause respiratory dysfunction when yeast cells reach the stationary phase and impair cells' growth defective in exosome-mediated mRNA degradation. More recently, Vms1 was reported to bind to 60S subunits at the mitochondrial surface and antagonize Rqc2 binding to 60S ribosomes (Izawa et al., 2017). Vms1 may reduce the efficiency of Rqc2 activity by increasing the speed of protein import into the mitochondria. This requires a rapid release of the stalled polypeptide from the 60S subunit through hydrolysis of the peptidyl-tRNA.

Indeed, Vms1 was recently reported to stimulate the cleavage of peptidyl-tRNA (Verma et al., 2018; Rendón et al., 2018; Kuroha et al., 2018). However, the molecular mechanisms by which Vms1 antagonizes Rqc2 acts as tRNA hydrolase or nuclease and rescues mitochondrial homeostasis are only poorly understood.

1.4.2 Aim of the Publication 2

In this thesis, the goal was to analyze the interaction of Vms1 with 60S subunits and study its function using combined cryo-electron microscopy, genetic, and biochemical approaches with yeast as a model system. This structural study aimed at gaining mechanistic insights into the interplay of the RQC factors and their role in protecting mitochondria from the aggregation of toxic proteins.

Chapter 2

Publications of this Dissertation

2.1 Publication 1 | The force-sensing peptide VemP employs extreme compaction and secondary structure formation to induce ribosomal stalling

eLIFE elifesciences.org

RESEARCH ARTICLE

The force-sensing peptide VemP employs extreme compaction and secondary structure formation to induce ribosomal stalling

Ting Su[1], Jingdong Cheng[1], Daniel Sohmen[1], Rickard Hedman[2], Otto Berninghausen[1], Gunnar von Heijne[2,3], Daniel N Wilson[1,4]*, Roland Beckmann[1]*

[1]Gene Center, Department of Biochemistry and Center for integrated Protein Science Munich, Ludwig Maximilian University of Munich, Munich, Germany; [2]Department of Biochemistry and Biophysics, Stockholm University, Stockholm, Sweden; [3]Science for Life Laboratory Stockholm University, Solna, Sweden; [4]Institute for Biochemistry and Molecular Biology, University of Hamburg, Hamburg, Germany

Abstract Interaction between the nascent polypeptide chain and the ribosomal exit tunnel can modulate the rate of translation and induce translational arrest to regulate expression of downstream genes. The ribosomal tunnel also provides a protected environment for initial protein folding events. Here, we present a 2.9 Å cryo-electron microscopy structure of a ribosome stalled during translation of the extremely compacted VemP nascent chain. The nascent chain forms two α-helices connected by an α-turn and a loop, enabling a total of 37 amino acids to be observed within the first 50–55 Å of the exit tunnel. The structure reveals how α-helix formation directly within the peptidyltransferase center of the ribosome interferes with aminoacyl-tRNA accommodation, suggesting that during canonical translation, a major role of the exit tunnel is to prevent excessive secondary structure formation that can interfere with the peptidyltransferase activity of the ribosome.

DOI: 10.7554/eLife.25642.001

***For correspondence:** Daniel.Wilson@chemie.uni-hamburg.de (DNW); beckmann@genzentrum.lmu.de (RB)

Competing interests: The authors declare that no competing interests exist.

Funding: See page 14

Received: 01 February 2017
Accepted: 22 May 2017
Published: 30 May 2017

Reviewing editor: Rachel Green, Johns Hopkins School of Medicine, United States

Introduction

Many diverse nascent chain sequences have been identified that act as *cis*-regulatory polypeptides to promote ribosome stalling and thereby regulate gene expression. One of the most recently discovered examples is the Vibrio export monitoring polypeptide (VemP) that allows *Vibrio alginolyticus* to adapt to changes in salinity by modulating expression of components of the protein targeting machinery (***Ishii et al., 2015***). *V. alginolyticus* is a Gram-negative marine-estuarine bacterium that, unlike most bacteria, has two paralogs of SecDF (SecDF1 and SecDF2) to enhance protein export in cooperation with the SecYEG translocon. In Na^+-rich environments, *V. alginolyticus* utilizes the Na^+-dependent SecDF1; however, in Na^+-limiting environments *V. alginolyticus* switches to the Na^+-independent (presumably H^+-dependent) SecDF2 (***Ishii et al., 2015***). The switch between SecDF1 and SecDF2 is facilitated by the stalling activity of VemP. In Na^+-rich environments, VemP is targeted by its signal sequence (SS) to the SecDF1-SecYEG translocon (***Ishii et al., 2015***). The force applied to VemP during protein translocation prevents VemP-dependent ribosome stalling, thereby enabling the complete VemP to be translated and released from the ribosome. Under such conditions, SecDF2 expression is repressed due to sequestration of the ribosome-binding site (RBS) of *secDF2*

within a stem-loop structure in the mRNA (***Figure 1a***). In Na^+-limiting environments, however, VemP is not translocated due to the inactivity of SecDF1, and the resulting lack of force on the VemP nascent chain leads to ribosomal stalling (***Figure 1a***). Ribosome stalling dissolves the stem-loop structure within the mRNA, exposes the RBS and thereby induces expression of Na^+-independent SecDF2 (***Figure 1a***). In brief, the mechanisms by which VemP switches protein synthesis between the SecDF1 and SecDF2 paralogs is dependent on the application of a force to the signal sequence containing VemP nascent chain. This force serves as a direct indicator of the SecDF-SecYEG protein translocation activity, which in turn is dependent on the environmental conditions.

Biochemical studies have demonstrated that VemP-dependent stalling occurs when Q156 is in the P-site of the ribosome and that distinct amino acid residues within a 19aa window (138–156) of VemP are critical for efficient ribosome stalling (***Figure 1a***) (***Ishii et al., 2015***). Although VemP-

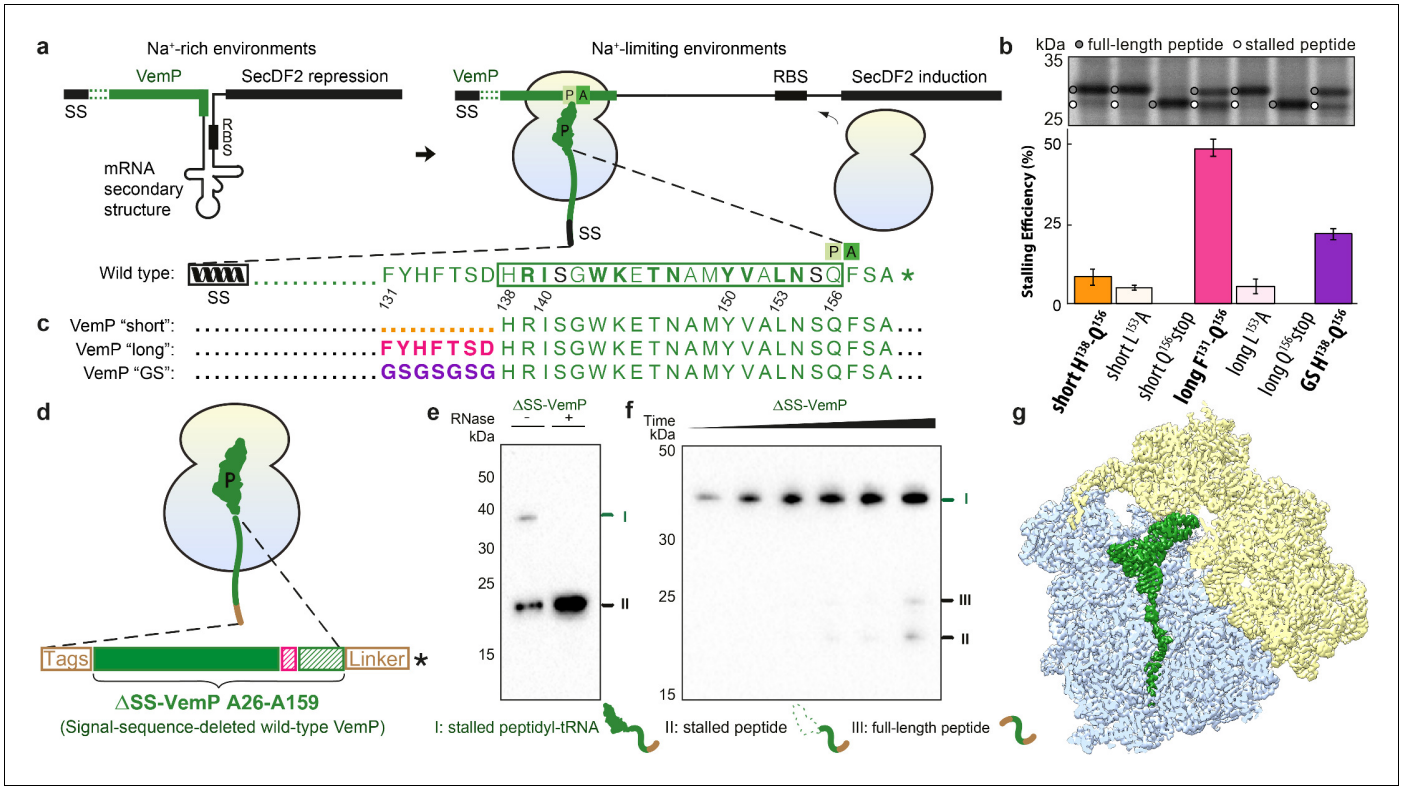

Figure 1. Biochemical and structural analysis of VemP stalling. (**a**) Schematic representation of the VemP-SecDF2 mRNA encoding VemP leader peptide with N-terminal signal sequence (SS) and C-terminal stalling region (green), followed by a stem-loop structure that sequesters the ribosome-binding site (RBS) of the SecDF2 gene (left). The translation arrest of VemP maintains the unfolded conformation of the mRNA allowing ribosome binding and induction of SecDF2 expression. The VemP stalling window H138–Q156 (boxed) is shown with critical (green bold) and important (green) residues highlighted (***Ishii et al., 2015***), and an asterisk indicating the stop codon (right). (**b–c**) In vivo pulse-chase analysis with different VemP constructs; VemP 'short' (H138–Q156, orange), VemP 'long' (F131–Q156, pink), VemP 'GS' (purple) and VemP mutants L153A and Q156*. (**d**) Schematic of the VemP-SRC used for cryo-EM. (**e–f**) Western blot against the N-terminal HA-tag of in vitro translated ΔSS-VemP detecting stalled peptidyl-tRNA (I), stalled free peptide (II) or full-length free peptide (III), (**e**) in the absence and presence of RNase A treatment, or (**f**) as a function of time (25, 40, 55, 70, 85, 100 min). (**g**) Transverse section of cryo-EM structure of the VemP-SRC showing the peptidyl-tRNA (green), with small and large subunits coloured in yellow and blue, respectively.

DOI: 10.7554/eLife.25642.002

The following figure supplements are available for figure 1:

Figure supplement 1. Triplicates of the pulse-chase analysis.

DOI: 10.7554/eLife.25642.003

Figure supplement 2. Classification of the VemP-SRC.

DOI: 10.7554/eLife.25642.004

Figure supplement 3. Resolution of the VemP-SRC.

DOI: 10.7554/eLife.25642.005

mediated regulation of SecDF2 expression is reminiscent of other peptide-stalling regulatory systems (**Ito and Chiba, 2013**; **Wilson et al., 2016**), such as SecM (**Nakatogawa and Ito, 2001**) and MifM (**Chiba et al., 2009**), the VemP stalling sequence and force-sensing mechanism appears to be completely distinct (**Ishii et al., 2015**; **Ito and Chiba, 2013**).

Results

Analysis of VemP sequence on efficiency of stalling

To ensure the stalling efficiency of the VemP constructs before initiating the structural analysis, we engineered three LepB-based constructs carrying C-terminal VemP residues, termed VemP 'short', 'long' and 'GS', respectively (**Figure 1b,c**). VemP 'short' carries the 19 amino acid segment that Ishii *et al* had chosen as the target for alanine scanning mutagenesis from VemP (138–156) (**Ishii et al., 2015**). VemP 'long' carries a 26 amino acid long segment including seven additional N-terminal residues of VemP (131–156), whereas VemP 'GS' is similar to the former two, except that residues 131–138 were substituted with a glycine-serine (GS) linker (**Figure 1b,c**). VemP 'short', 'long' and 'GS' were expressed in pulse-chase experiments in *E. coli* without any N-terminal signal sequence (see Material and methods). Using this assay, the major product observed to accumulate for VemP 'short' was full-length LepB-VemP fusion protein, whereas relatively little (10%) stalled peptide was detected (**Figure 1b,c** and **Figure 1—figure supplement 1**). In contrast, VemP 'long' containing the extended stalling window dramatically increased the stalling efficiency (**Figure 1b,c**). As expected, mutations previously reported to abrogate ribosome stalling (**Ishii et al., 2015**), L153A and Q156stop, led to a reduction in stalling efficiency for the VemP 'short' and particularly for the VemP 'long' constructs. VemP 'GS' also had a reduced stalling efficiency (**Figure 1b,c**). Taken together, these fusion proteins proved to be ineffective at inducing elongation arrest to the full extent in vivo. The influence of residues 131–138 on ribosome stalling and SecDF2 induction was not so extensively characterized in the previous study, where only mutation of residues 132 and 136–138 to alanine were reported to have little or no effect (**Ishii et al., 2015**). Thus, our results suggest that residues beyond the previously characterized 19-aa stalling window of VemP contribute to the efficiency of VemP-mediated translation arrest.

Cryo-EM structure of the VemP-SRC

In order to investigate which residues of VemP are involved in establishing interactions with the exit tunnel during ribosome stalling, and in particular to decipher the molecular mechanism of force-sensitive ribosome stalling by VemP, we used cryo-EM to determine the structure of a VemP-stalled ribosome-nascent chain complex (VemP-SRC). Since we observed a contribution of the amino acids in VemP beyond the initially identified stalling window and to ensure the maximum ribosome stalling efficiency, the wildtype VemP sequence lacking only the signal sequence (residues 26–159, ΔSS-VemP), rather than a shorter stalling window, was used (**Figure 1d**). Translation of the ΔSS-VemP construct in an *E. coli* lysate-based translation system led to the accumulation of VemP-peptidyl-tRNA (about 40 kDa), of which the size was reduced to the expected free peptide (18 kDa) upon RNase treatment (**Figure 1e**). The robustness of stalling of the wildtype ΔSS-VemP was evident from the persistence of the VemP-peptidyl-tRNA, even with incubation times of up to 100 min where only minor fractions of full-length VemP were produced (**Figure 1f**). The VemP-SRC was purified using sucrose density gradient centrifugation and N-terminal affinity tags and subjected to cryo-EM analysis (see Materials and methods). *In silico* sorting of the VemP-SRC dataset yielded a major subpopulation of ribosomal particles that contained stoichiometric occupancy of the P-tRNA (**Figure 1—figure supplement 2**). Subsequent refinement resulted in a final reconstruction of the VemP-SRC (**Figure 1g**) with an average resolution of 2.9 Å and a local resolution of 2.5 Å within the core of the ribosome (**Figure 1—figure supplement 3** and **Table 1**). The electron density for the majority of the VemP nascent chain was well resolved within the exit tunnel, with local resolution ranging between 3.0 and 3.5 Å (**Figure 1—figure supplement 3**), thus enabling a molecular model for residues 120–156 of VemP to be built *de novo* (**Figure 2** and **Videos 1** and **2**).

Table 1. Refinement and Model Statistics.

Data collection	
Particles	400,024
Pixel size (Å)	1.084
Defocus range (μm)	1–2.5
Voltage (kV)	300
Electron dose ($e^-/Å^{-2}$)	25
Model Composition	
Protein residues	5615
RNA bases	4641
Refinement	
Resolution (Å, 0.143 FSC)	2.93
Map sharpening B factor ($Å^2$)	-162.55
$FSC_{Average}$	0.90
Validation	
rmsd, bonds	0.016
rmsd, angles	1.66
Rotamers outliers (%)	1.45
Ramachandran outliers (%)	1.00
Ramachandran favoured (%)	90.29
Correct sugar puckers (%)	98.77
Good backbone conformations (%)	81.74
Scores	
MolProbity	1.96
Clash score, all atoms	5.45

DOI: 10.7554/eLife.25642.007

Extreme compaction of the VemP nascent chain in the ribosomal tunnel

The VemP nascent chain adopts an extremely compacted conformation within the exit tunnel comprising two α-helices, located in the upper and lower regions of the tunnel, connected by an α-turn and loop (***Figure 2a–d*** and ***Video 1***). The α-helix located in the upper region of the tunnel is comprised of the C-terminal 10 residues (N147–Q156) of VemP and is directly linked to the P-tRNA and thereby located directly in the peptidyltransferase center (PTC) of the ribosome (***Figure 2a,b***). The α-helix located in the lower region of the tunnel is comprised of the N-terminal 10 residues (M120–S129) of VemP for which density is clearly visualized. We note that the N-terminal stretch of the VemP nascent chain from the lower α-helix to tunnel exit is less well resolved (***Figure 1—figure supplement 3***). The formation of α-helical secondary structure within the upper and lower regions of the exit tunnel is generally consistent with previous biochemical and structural studies (***Bhushan et al., 2010a***; ***Kosolapov and Deutsch, 2009***; ***Lu and Deutsch, 2005***; ***Matheisl et al., 2015***; ***Woolhead et al., 2004***). The linker between the two α-helices is located within the constriction of the exit tunnel, adjacent to ribosomal proteins uL4 and uL22 (***Figure 2a–d***). The linker is composed of 17 residues (130–146) that form two consecutive turns: one connecting the C-terminal α-helix which is a canonical α-turn (I140–K144), followed by a less well-ordered turn without hydrogen bonding (***Figure 2a–d*** and ***Video 2***). Protein folding events have been demonstrated to occur within the ribosomal exit tunnel (***Holtkamp et al., 2015***; ***Lin et al., 2012***; ***Marino et al., 2016***; ***Nilsson et al., 2015***; ***Tu et al., 2014***); (***Bhushan et al., 2010b***; ***Matheisl et al., 2015***); Of those so far characterized, folding was shown to occur within the lower region of the tunnel, e.g. ADR1 (***Nilsson et al., 2015***) and within the vestibule at the periphery where the exit tunnel widens (***Cabrita et al., 2016***; ***Nilsson et al., 2017***; ***Trovato and O'Brien, 2016***; ***Tu et al., 2014***).

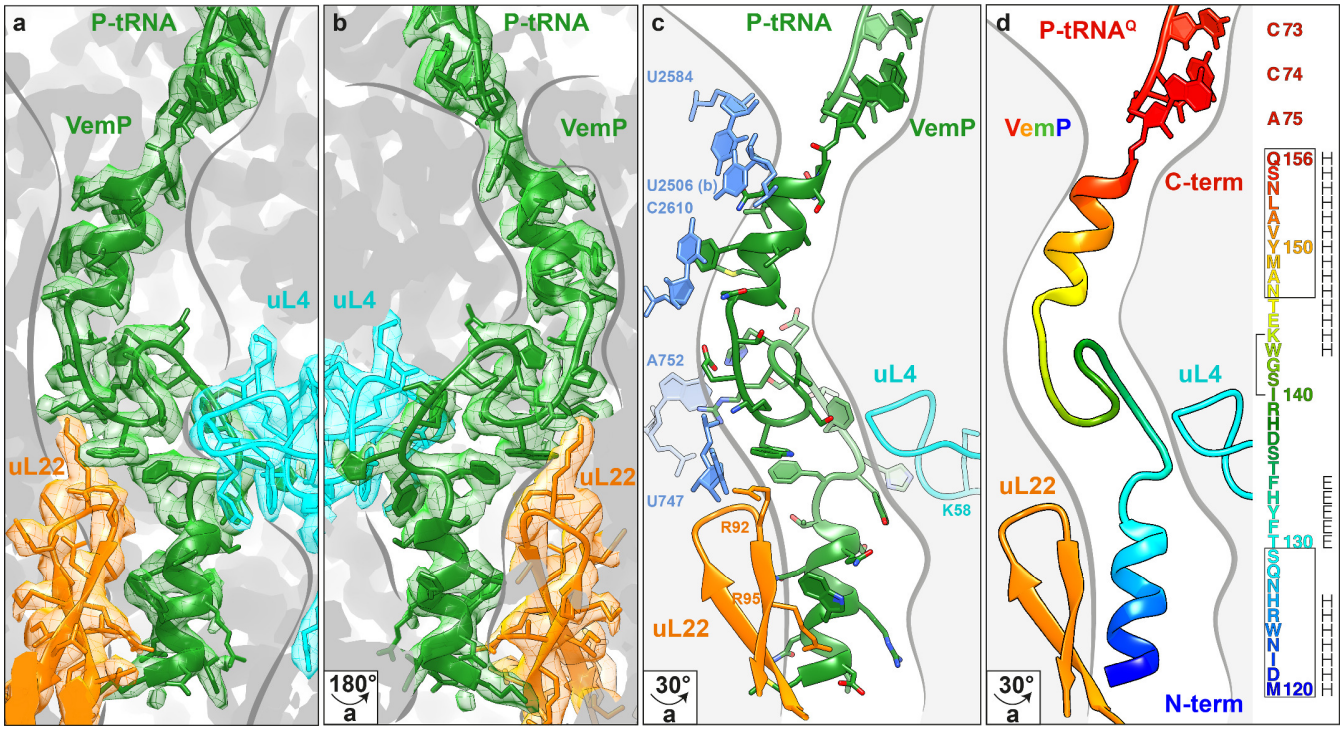

Figure 2. Overview of the VemP nascent chain in the ribosomal tunnel. (**a–b**) Isolated electron density and molecular model for the VemP nascent chain connected to the P-tRNA (green) in the ribosomal tunnel (grey) with ribosomal proteins uL4 (cyan) and uL22 (orange) highlighted. (b) is the same as (a) but rotated by 180˚. (**c**) Model of the VemP nascent chain in the ribosomal tunnel highlighting ribosomal components that interact with VemP, namely, nucleotides of the 23S rRNA (blue) and ribosomal proteins uL4 (cyan) and uL22 (orange). (**d**) Rainbow representation of the VemP nascent chain with sequence coloured accordingly. The upper and lower α-helices of VemP are boxed and the α-turn in the linking loop region is bracketed. Secondary structure predictions for VemP are indicated with H (helix) and E (loop region).

DOI: 10.7554/eLife.25642.006

Additionally, in the hCMV stalling peptide a C-terminal α-helix was also observed in the upper region of the tunnel in a similar yet slightly shifted position compared to the C-terminal helix of VemP (***Figure 3***) (***Bhushan et al., 2010b***; ***Matheisl et al., 2015***). Structurally, the extensive compaction and secondary structure formation of VemP results in an unprecedented total of 37 residues being housed within the upper two thirds (approximately 50–55 Å) of the ribosomal exit tunnel, which contrasts with the 21–33 aa that were visualized within the exit tunnel for other stalling peptides, such as SecM (***Bhushan et al., 2011***; ***Zhang et al., 2015***), MifM (***Sohmen et al., 2015***), TnaC (***Bischoff et al., 2014***; ***Seidelt et al., 2009***) and CMV (***Bhushan et al., 2010b***; ***Matheisl et al., 2015***) (***Figure 3***). When calculating the theoretical minimal number of residues for the VemP peptide chain to stretch all the way from the PTC to the tunnel exit, it would require at least

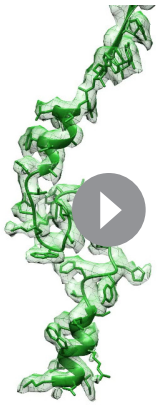

Video 1. Cryo-EM density and model for the VemP nascent chain. Video showing the quality of the cryo-EM density (green mesh) and fit of the molecular model (green ribbon) of the VemP nascent chain and CCA-end of the P-tRNA.

DOI: 10.7554/eLife.25642.008

51 aa, which is in stark contrast to only 31 aa for MifM and 34 for SecM due to lack of compaction.

Interaction of VemP within the ribosomal exit tunnel

Alanine scanning mutagenesis of VemP identified 10 residues that are critical for ribosome stalling, as well as an additional seven residues that significantly reduced stalling when mutated (***Ishii et al., 2015***). These residues encompass 17 of the 19-aa stalling window of VemP 'Short', with only the mutations of either S141A and S155A having no influence on ribosome stalling. Many of these residues establish specific interactions with components of the ribosomal exit tunnel, which is likely to explain their importance for ribosomal stalling (***Figure 4a–f***). For example, the sidechains of N154 and Y150, which are located in the upper C-terminal α-helix of VemP, can stack on the nucleobases of U2506 (***Figure 4a***) and C2610 (***Figure 4c***), respectively, of the 23S rRNA. Additionally, N154 comes within hydrogen bonding distance of U2584 (***Figure 4b***). Within the α-turn of VemP, K144 can hydrogen bond with the non-bridging phosphate-oxygen of U747 (***Figure 4d***), whereas W143 can stack upon the R92 sidechain located the tip of the β-hairpin of uL22 (***Figure 4e***). Consistently, alterations in uL22 have been shown to reduce the efficiency of VemP-mediated ribosome stalling (***Ishii et al., 2015***). The α-turn of VemP is additionally stabilized by stacking interactions between R139 of VemP and A752 of the 23S rRNA (***Figure 4f***). The seven residues (131–137) within the loop linking the α-turn of VemP to the lower N-terminal α-helix map within the VemP 'Long' region. As mentioned, alanine mutagenesis (Y132A, S136–H138A) suggested that the identity of some of these residues is not important for ribosome stalling, with the exception of the H138A mutation that had a modest effect on arrest efficiency (***Ishii et al., 2015***). Consistently, in the VemP-SRC structure, residues 135–138 of loop are less well-resolved and no sidechain interactions with the exit tunnel are observed. By contrast, the remaining loop residues (130–134) are better resolved. The sidechain of H133 comes within hydrogen bonding distance of the backbone of K58 of uL4 (***Figure 4g***), which may contribute to the improved stalling efficiency of the VemP 'Long' over the VemP 'Short' observed in ***Figure 1b***. Additionally, the sidechain of W124, which is located in the lower N-terminal α-helix of VemP, stacks on the R95 sidechain of uL22 (***Figure 4h***). Collectively, the interactions observed in the VemP-SRC structure are consistent with previous biochemical and mutational analysis indicating that the majority of critical residues and interactions are located in the upper region of the tunnel, but that the additional residues within the lower region of the tunnel can also contribute to the efficiency of stalling.

Silencing of the PTC by the C-terminal α-helix of VemP

Biochemical analysis indicates that VemP-stalled ribosomes arrest translation because peptide bond formation cannot occur between Gln156 of the VemP-peptidyl-tRNA in the P-site and Phe157 of the incoming aminoacyl-tRNA of the A-site (***Ishii et al., 2015***). Comparison of the conformation of nucleotides at the PTC of the VemP-stalled ribosomes revealed two nucleotides of the 23S rRNA, U2585 and U2506, which adopt conformations incompatible with peptide bond formation (***Figure 5a***). Accommodation of an aminoacyl-tRNA at the A-site of the PTC requires a transition of the PTC from an uninduced to an induced state, which involves a shift in the position of U2585 (***Figure 5b***) (***Schmeing et al., 2005***; ***Youngman et al., 2004***). In the VemP-SRC, U2585 adopts a unique conformation, distinct from both the uninduced and induced U2585 conformations (***Figure 5b***). Moreover, the upper α-helix of VemP extends into the PTC and thereby directly prevents the transition of U2585 from the uninduced to the induced state, due to steric clashes with Asn154 of VemP (***Figure 5c***). In contrast to VemP, the hCMV helix does not directly prevent the analogous human nucleotide U4493 (*E. coli* U2585) from adopting the induced state. It is rather hCMV's penultimate Pro21, which is not part of the helix, that prevents this transition (***Figure 5d***). Additionally, U2506 is observed to adopt two distinct conformations, U2506(a) and U2506(b) in the VemP-SRC (***Figure 5a***). The U2506(a) conformation would sterically clash with the aminoacyl moiety of A-tRNA (***Figure 5e***) and is likely to contribute to prevent aminoacyl-tRNA accommodation at the A-site of the PTC. The induced state of the PTC also involves a shift in the position of U2506 (***Schmeing et al., 2005***; ***Youngman et al., 2004***) (***Figure 5f***), which cannot occur in the VemP-SRC because the upper α-helix of VemP blocks the induced conformation of U2506 (***Figure 5g***), analogously to that observed for U2585 (***Figure 5c***). Unlike VemP, hCMV does not retain an uninduced conformation of human U4414 (*E. coli* U2506) but allows the induced conformation of U4414 since it

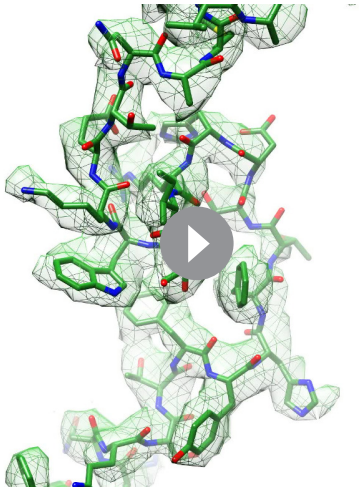

Video 2. Cryo-EM density and model for α-turn and loop of the VemP nascent chain. Video showing a zoom of the cryo-EM density (green mesh) and fit of the molecular model (stick representation) of the α-turn and loop of the VemP nascent chain.
DOI: 10.7554/eLife.25642.009

is sterically less constrained by the more distant hCMV helix (***Figure 5h***) (***Matheisl et al., 2015***). Taken together, although α-helix formation has also been observed in the upper tunnel of an hCMV-stalled ribosome (***Matheisl et al., 2015***), the CMV α-helix did not directly extend into the PTC as seen here for VemP (***Figure 3f–g*** and ***Figure 5d,h***). Indeed, the two C-terminal proline residues of the CMV stalling peptide appeared to be more important for inactivating the PTC and inducing translation arrest (***Matheisl et al., 2015***). Notably, translation arrest via stabilization of the uninduced state has also been observed for other force-sensing stalling peptides on the ribosome, such as SecM (***Zhang et al., 2015***) and MifM (***Sohmen et al., 2015***). However, the mechanism is different since both, SecM and MifM, adopt entirely extended conformations within the tunnel, unlike VemP (***Figure 3***).

Discussion

Collectively, the VemP-SRC structure reveals that VemP adopts an extremely compacted conformation within the ribosomal exit tunnel, comprising an upper and a lower α-helix connected by an α-turn and a loop. On the stalled ribosome, the upper α-helix of VemP encroaches directly upon the PTC and stabilizes an uninduced state of the PTC that prevents accommodation of the incoming A-tRNA and thereby promotes translation arrest (***Figure 6a***). These findings suggest that formation of secondary structure, such as an α-helix, directly at the PTC is likely to be detrimental for peptide bond formation and, therefore, for translation efficiency. Thus, the PTC of the ribosome and its immediate tunnel context must have evolved to generally disfavour excessive secondary structure formation. However, it also raises the question as to whether secondary structure formation at the PTC is used by the ribosome for specific nascent proteins to modulate the rate of translation, which could have important downstream consequences for co-translational protein folding and targeting events.

Relief of VemP-mediated ribosome stalling is proposed to result from the force exerted on the nascent chain during membrane insertion of the N-terminal signal sequence (***Ishii et al., 2015***). It is easy to imagine how, in the case of VemP, force application would inevitably prevent the formation of extensive secondary structure formation during translation, or at least lead to an unraveling of any secondary structure that does form within the tunnel, and thereby eventually allowing sterically the transition into the induced conformation of the PTC. As a result, peptide bond formation would be promoted again and translation elongation continued (***Figure 6b***). Interestingly, all three molecularly characterized force-sensing stallers employ the mechanism of preventing the adoption of the catalytically required induced state of the PTC by steric hindrance. This may be the favoured mechanism because the conformational trajectory from the uninduced to the induced state coincides with the direction of force applied to the nascent peptide (***Figure 6b***). Yet, it is surprising that the stalling peptides use completely different modes by which they interact with the ribosomal tunnel in a force-sensitive manner to achieve this goal.

Materials and methods

DNA manipulations

To test the effect of adding the extra C-terminal VemP sequence to the identified 19aa stalling window (***Ishii et al., 2015***), the VemP 'short' plasmid was constructed from a previously designed

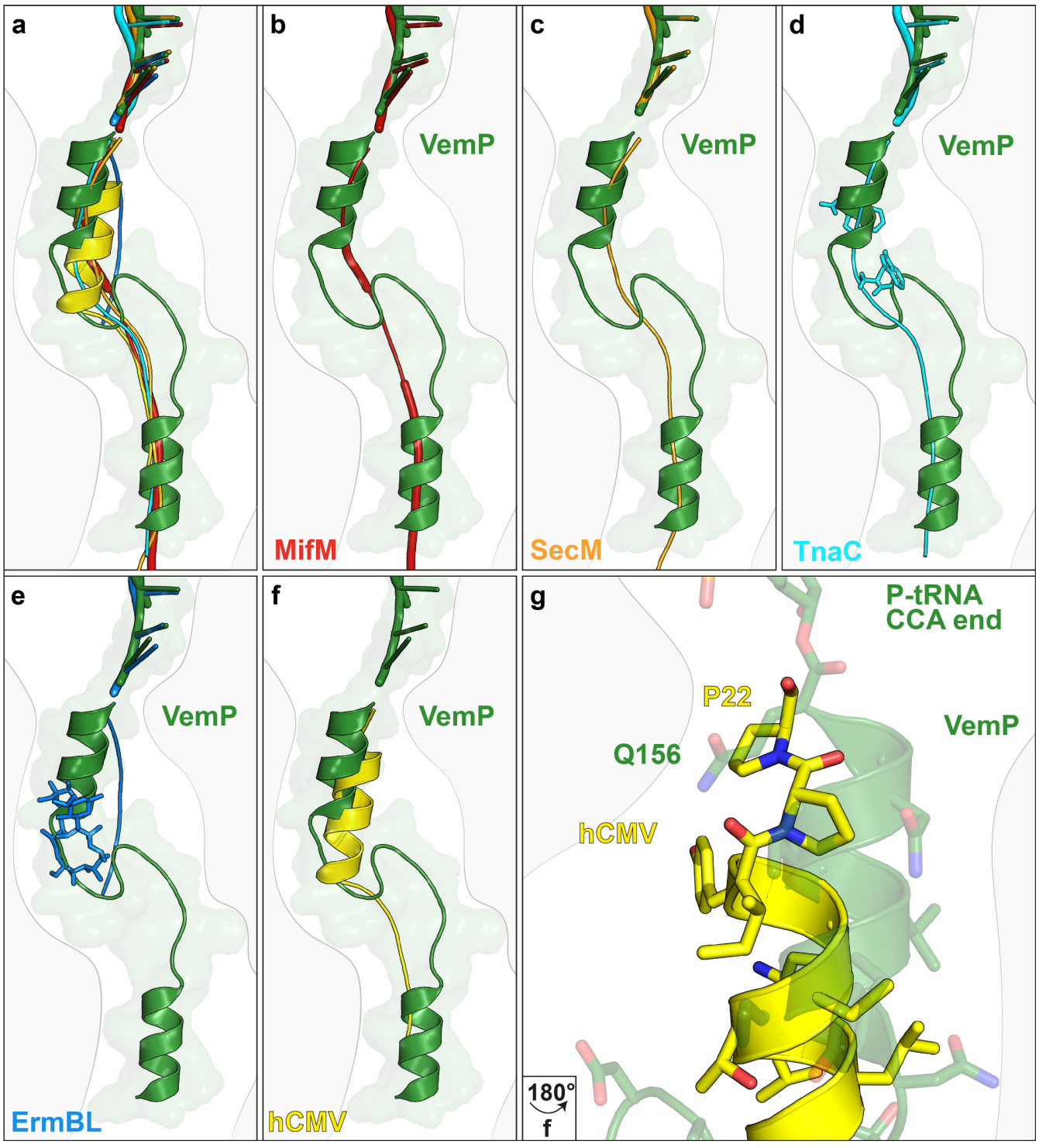

Figure 3. Comparison of the VemP nascent chain in the ribosomal tunnel with other stalling peptides. (**a**) Overall superposition of VemP (model in green, surface in light green) with MifM (red, PDB ID 3J9W) (***Sohmen et al., 2015***), SecM (orange, PDB ID 3JBU) (***Zhang et al., 2015***), hCMV (yellow, PDB ID 5A8L) (***Matheisl et al., 2015***), TnaC (cyan, PDB ID 4UY8) (***Bischoff et al., 2014***) and ErmBL (blue, PDB ID 5JU8)(***Arenz et al., 2016***) in the ribosomal tunnel (light grey). The CCA-end of the P-tRNA is shown for reference. The ribosomal tunnel is shown schematically in grey. (**b–f**) Superposition of VemP (green) with each arrest peptide described above. For (**d**) TnaC and (**e**) ErmBL, the two tryptophans (cyan) and the one

Figure 3 continued on next page

Figure 3 continued

erythromycin (blue) molecule are shown, respectively. (**g**) A zoomed-in view of (**f**) showing the superposition of VemP (green) and hCMV (yellow) in the C-terminal helical part including the side chains. The last residue, Q156 in case of VemP and P22 in case of hCMV, connecting to the CCA end of tRNA is labelled.

DOI: 10.7554/eLife.25642.010

pING1 plasmid carrying a *lepB*-based construct harboring a SecM arrest peptide (***Ismail et al., 2012***). In order to produce a soluble, non-membrane targeted variant, transmembrane helix 1 and 2 of Lep were deleted using PCR. To replace the SecM arrest peptide with the VemP arrest sequence, the plasmid was amplified using a primer pair producing a linear plasmid lacking the SecM arrest peptide. Gibson assembly (***Gibson et al., 2009***) was then used to ligate synthesized oligonucleotides corresponding to the VemP arrest peptide (in bold) and its following three residues, **HRISGWKETNAMYVALNSQ**FSA, into the plasmid. Overlap PCR (***Liu and Naismith, 2008***) was used to replace the seven Lep residues just upstream of the VemP 'short' arrest peptide with the corresponding seven residues from the native VemP and by GSGSGSG to generate VemP 'long', FYHFTSDHRISG WKETNAMYVALNSQFSA, and VemP 'GS', GSGSGSGHRISGWKETNAMYVALNSQFSA, respectively. Overlap PCR was also used to generate other variants of VemP used in pulse-labelling analysis.

For in vitro translation and cryo-grid sample preparation, the full VemP gene without the signal sequence (ΔSS-VemP, A26-A159) was cloned from synthesized *V. alginolyticus* genome by KOD XtremeTM Hot-Start DNA Polymerase (Novagen, MA, USA), and subsequently inserted to modified plasmid p7XNH3 by FX cloning method (***Geertsma, 2014***). The complete construct contains an N-terminal His-tag for purification, a FLAG-tag for detection and a TEV-protease cleavage site as a linker sequence. The C-terminus following the ΔSS-VemP comprises a spacer containing a 3C-protease cleavage site and an HA-tag.

MPWIYLRKLILLLFAMVLLPVHVSAAQIDHKAHVPHFSKLQPFVAVSVSPNSSVDFSEASEESSQSPVSE-GHASLDSVALFNSQRWTSYLREGLDDEHVDFVGDLTTPFYADAGYAYSLMDINWRHNQSTFYHFTSDHRI SGWKETNAMYVALNSQFSA(TAA-Stop x2) is the total amino acid sequence of the construct.

In vivo pulse-labelling

E. coli MC1061 carrying plasmids with the different *lepB*-based constructs described in the paper were cultured overnight at 37°C in M9 minimal medium supplemented with 19 natural amino acids (1 µg/ml; no methionine, 100 µg/ml thiamine, 0.1 mM $CaCl_2$, 2 mM $MgSO_4$, 0.4% (w/v) fructose, and 100 µg/ml ampicillin). Overnight cultures were back-diluted to OD_{600} ~0.05–0.1 and grown 2.5 to 3.5 hr to an OD_{600} of 0.2–0.35. Protein expression was induced with 0.2% (w/v) arabinose for 5 min, whereafter expressed proteins were radiolabelled with [^{35}S]methionine for 2 min at 37°C. Ice-cold trichloroacetic acid (TCA) was added to a final concentration of 10% and the samples were incubated on ice for 30 min. The samples were centrifuged for 5 min at 20,800 x g at 4°C and the precipitates were washed with cold acetone, and spun again for 5 min at 20,800 x g at 4°C. The precipitates were resolubilized in Tris-SDS solution (10 mM Tris-HCl, pH 7.5, and 2% SDS) at 95°C for 10 min and spun for 5 min at room temperature. The protein of interest was then immunoprecipitated using anti-LepB antibody and the resulting samples were prepared for SDS-PAGE analysis with Laemmli sample buffer supplemented with 400 µg/ml RNase A. Gels were analyzed with a Fuji FLA-3000 phosphorimager and ImageGauge V4.23 software. Quantification of protein bands was performed using EasyQuant (in-house developed software). The fraction of full-length values (fFL) was calculated using the formula fFL = IFL / (IFL+IA), where IFL is the quantified intensity of the full-length protein band and IA is the quantified intensity of the arrested protein band. Experiments were repeated in triplicate and standard errors of the mean were calculated.

In vitro transcription and translation

For the RNase treatment assay and the final large scale purification for cryo-grid, RTS 100 *E.coli* HY Kit (5 PRIME) was used (transcription and translation coupled). 500 µL reaction was incubated at 30°C for 35 min with 12.6 pmol PCR-product template generated upon the ΔSS-VemP construct. RNase was added to the reaction where indicated, and incubated at 30°C for an additional 10 min. For the time course, the same amount of PCR-product template was used with the PURExpress In Vitro Protein Synthesis Kit (New England Biolabs #E6800S, transcription and translation coupled).

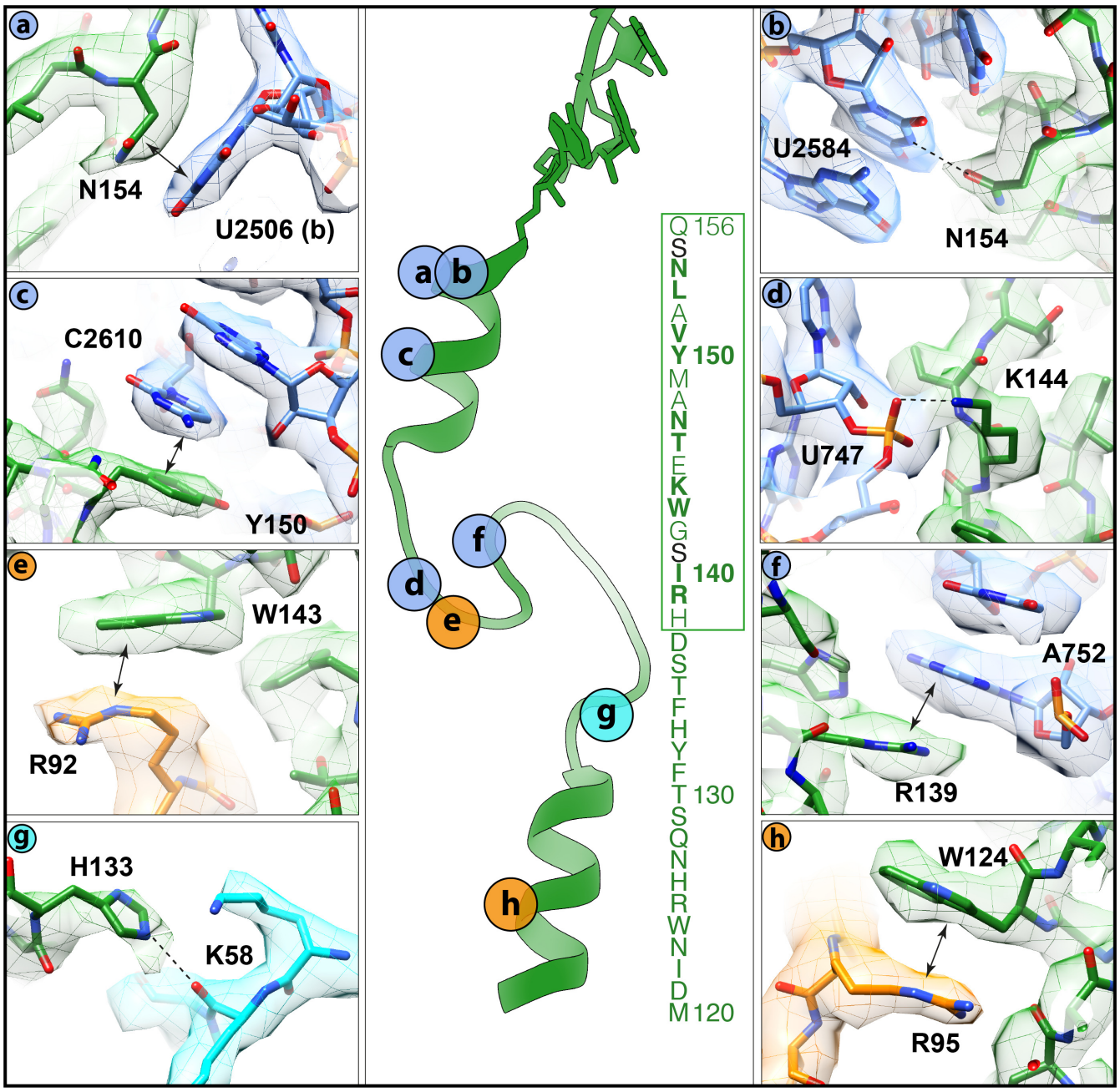

Figure 4. Interactions of the VemP nascent chain with the ribosomal tunnel (with density shown). (**a**) N154 of VemP (green) stacks upon U2506(b) of the 23S rRNA (blue). (**b**) N154 of VemP is within hydrogen bond distance of nucleotide U2584. (**c**) Y150 of VemP stacks upon C2610. (**d**) K144 of VemP forms a salt bridge with U747. (**e**) W143 of VemP stacks with R92 of uL22 (orange). (**f**) R139 of VemP stacks upon A752. (**g**) W124 of VemP stacks upon R95 of uL22. (**h**) H133 of VemP interacts with K58 of uL4 (cyan). The middle panel maps the approximate locations of the interactions and includes the sequence of VemP with critical (bold) and important (boxed green) residues highlighted (***Ishii et al., 2015***). In panels (**a–h**) the electron density for the VemP-SRC map (mesh) is coloured according to either VemP (green), 23S rRNA (blue), uL4 (cyan) or uL22 (orange).
DOI: 10.7554/eLife.25642.011

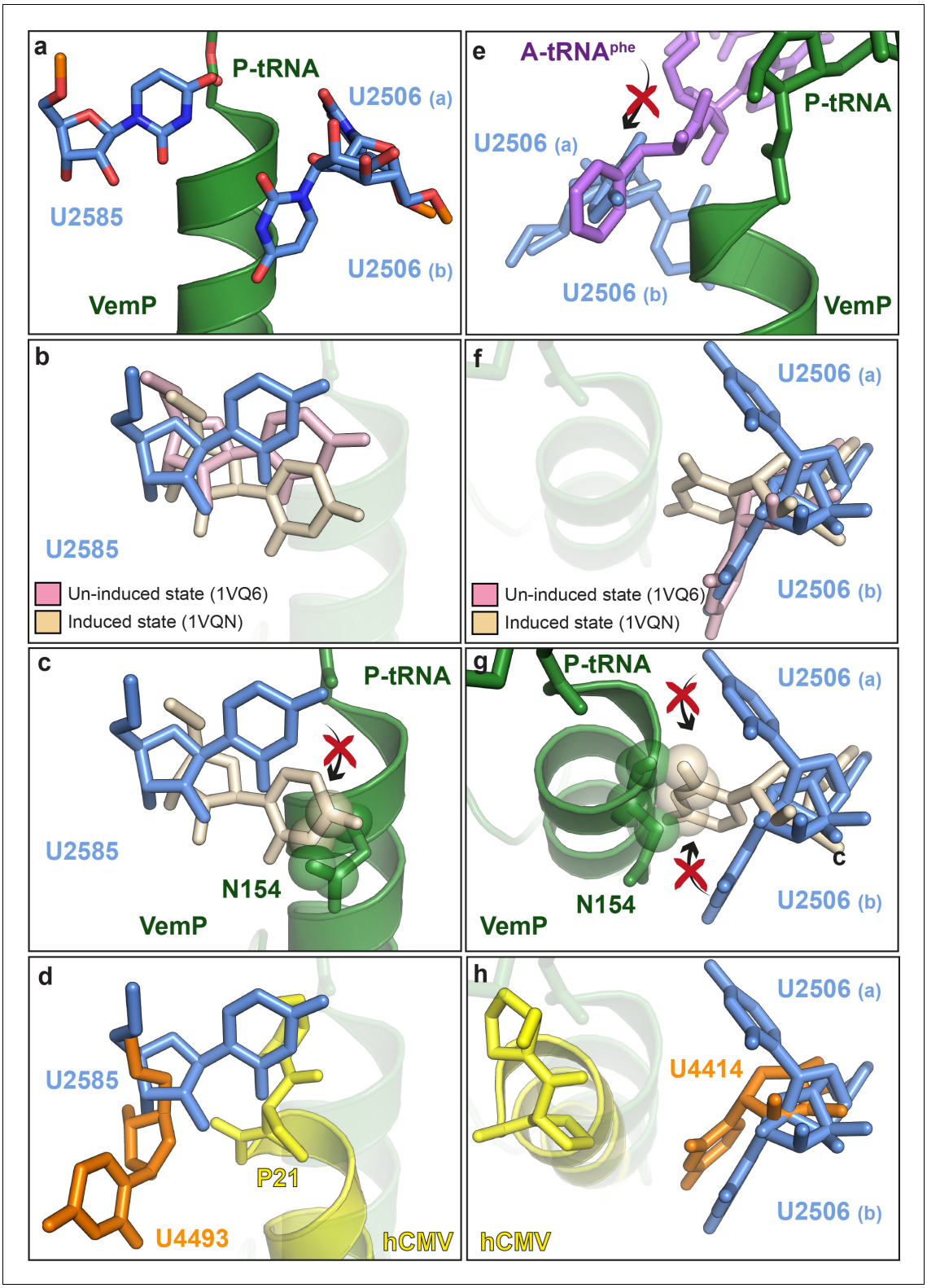

Figure 5. VemP stabilizes the uninduced state of the PTC to inhibit A-tRNA accommodation. (**a**) Conformation of U2585 and U2506 relative to VemP (green) at the PTC of the VemP-SRC. (**b**) Conformation of U2585 (blue) in the VemP-SRC compared with the uninduced (pink, PDB ID 1VQ6) and induced (tan, PDB ID 1VQN) states (***Schmeing et al., 2005***). (**c**) N154 of the upper α-helix of VemP clashes (indicated by spheres) with the induced conformation of U2585 (***Schmeing et al., 2005***). (**d**) Conformation of human U4493 (orange, numbering according to PDB ID 5A8L and 5AJ0, being

Figure 5 continued on next page

Figure 5 continued

equivalent to U4531 in PDB ID 4UG0 and 4V6X) in the hCMV-SRC compared with *E. coli* U2585 (blue) in the VemP-SRC. (**e**) The U2506(a) conformation overlaps the binding position of an accommodated Phe-tRNA (purple) at the A-site of the PTC (***Schmeing et al., 2005***). (**f**) Conformation of U2506 in the VemP-SRC (blue) compared with the uninduced (pink) and induced (tan) states (***Schmeing et al., 2005***). (**g**) N154 of the upper α-helix of VemP clashes (indicated by spheres) with the induced conformation of U2506 (***Schmeing et al., 2005***). (**h**) Conformation of human U4414 (orange, numbering according to PDB ID 5A8L and 5AJ0, being equivalent to U4452 in PDB ID 4UG0 and 4V6X) in the hCMV-SRC compared with U2506 (blue) in the VemP-SRC. hCMV stalling peptide is shown in yellow in (**d**) and (**h**).

DOI: 10.7554/eLife.25642.012

Reactions were incubated at 37˚C for various times (25/40/55/70/85/100 min). For western blotting, reaction products were separated by either home-made or commercial NuPAGE 12% Bis-Tris gels (Invitrogen, CA, USA) with 1x MOPS buffer. Proteins were blotted to nitrocellulose membrane (Carl Roth, Germany), incubated with mouse anti FLAG M2 HRP (Sigma, Germany) and visualized by ChemiDoc MP System (Bio-Rad).

Purification of the VemP-SRC

500 µL in vitro translation reaction was loaded onto 10–50% sucrose gradient prepared with Buffer C (25 mM pH 7.2 HEPES-KOH, 100 mM KOAc, 10 mM $Mg(OAc)_2$, 0.01% DDM, 1/1,000 complete protease inhibitor (Roche, Germany), 0.2 U/mL RNase, 2 mM 2-mercaptoethanol) and centrifuged for 3 hr in a Beckman coulter SW40 Ti swinging bucket rotor with 35,000 r.p.m. at 4˚C. Gradients were separated on a Biocomp Gradient Station and fractions containing 70S ribosomal particles were collected and loaded onto a Talon metal affinity chromatography column (1.5 ml resin) pre-equilibrated in 10 mL buffer C containing 10 µg/mL bulk tRNA. The column was washed with 25 ml buffer C until no significant absorption (OD_{260}) could be detected in the wash fractions. The VemP-SRC, bound to the Talon matrix by the VemP N-terminal His-tag, was eluted in 750 µL buffer C containing 150 mM imidazole. The elution was pelleted for 4 hr 20 min in a Beckman Coulter TLA 120.2 fixed-angle rotor with 51,000 r.p.m. at 4˚C. 15.6 pmol VemP-SRC pellet was resuspended in ice-cold buffer C without DDM, aliquoted and snap-frozen.

Cryo-electron microscopy and single particle reconstruction

E. coli VemP-SRC (6 OD_{260}/mL) was applied to 2 nm pre-coated Quantifoil R3/3 holey carbon supported grids and vitrified using Vitrobot Mark IV (FEI). Data collection was performed using EM-TOOLS (TVIPS GmbH) on a Titan Krios transmission electron microscope equipped with a Falcon II direct electron detector (FEI) at 300kV at a pixel size of 1.084 Å and a defocus range of 1–2.5 µm. 10 frames (dose per frame of 2.5 $e^-/Å^2$) were aligned using MotionCor2 (***Li et al., 2013***). Power-spectra, defocus values and astigmatism were determined with CTFFIND4 software (***Rohou and Grigorieff, 2015***). 5735 micrographs were manually inspected in real space and in the meantime filtered by threshold of resolution at 4.5 Å and astigmatism at 5% resulting in 4849 micrographs. 850,433 particles were automatically picked by Gautomatch (http://www.mrc-lmb.cam.ac.uk/kzhang/) and single particles were processed using RELION 1.4 (***Scheres, 2012***). After 2D classification, 789,006 particles were subjected to 3D refinement using *E. coli* 70S ribosome as reference structure, followed by several further rounds of 3D classifications, including tRNA-focused sorting (64 rounds) and sorting (58 rounds) with a ribosome mask (***Figure 1—figure supplement 2***). One major class containing 400,024 particles (62%) was further refined, resulting in a final reconstruction with an average resolution of 2.9 Å (0.143 FSC) (***Figure 1—figure supplement 3***). The map was subsequently B-factored by EMBfactor (***Fernández et al., 2008***) with the FSC. Finally, the local resolution was calculated using ResMap (***Kucukelbir et al., 2014***).

Molecular modeling and refinement of the VemP-SRC

The molecular model for the ribosomal proteins and rRNA of the 70S ribosome of the VemP-SRC was based on the molecular model from cryo-EM reconstruction of the *E. coli* 70S ribosome (PDB ID 5JU8) (***Arenz et al., 2016***), except that the bL31 was based on the (PDB ID 5LZD) (***Fischer et al., 2016***). The molecular model for Gln-tRNA was based on a crystal structure (PDB ID 1GSG) (***Rould et al., 1989***). The molecular models were initially fitted as a rigid body into the cryo-EM density map of the corresponding stalled complex using UCSF Chimera (***Pettersen et al., 2004***). The

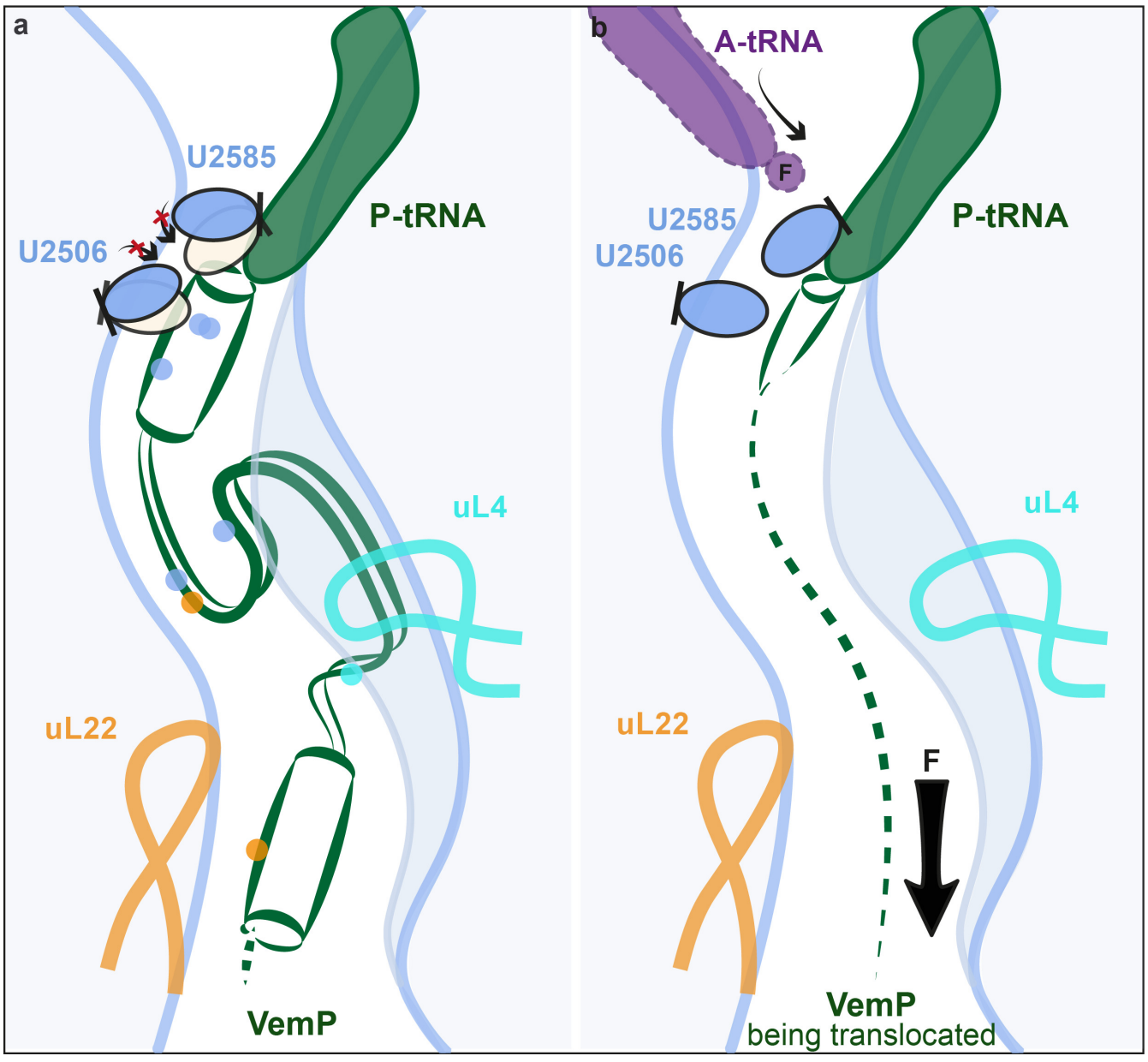

Figure 6. Model for VemP-mediated translation stalling and relief. (**a–b**) Schematic summarizing the molecular basis for (**a**) VemP-dependent translation arrest and (**b**) relief of arrest via the pulling-force (indicated by arrow) on VemP protein translocation.
DOI: 10.7554/eLife.25642.013

complete atomic model of the VemP-SRC was manually adjusted using Coot (***Emsley and Cowtan, 2004***) and refined using phenix.real_space_refine with restraints obtained by phenix.secondary_-structure_restraints (***Adams et al., 2010***). The Phenix refined model was further refined using REFMAC (***Vagin et al., 2004***) to validate the overfitting as previously described (***Brown et al., 2015***) (***Figure 1—figure supplement 3***). The statistics of the refined model were calculated using Molprobity (***Chen et al., 2010***) are presented in ***Table 1***.

Figure preparation

The protein secondary structure prediction of the native VemP sequence was performed using the MPI bioinformatics Toolkit (***Alva et al., 2016***) with the prediction method written by B. Rost (***Rost, 2001***). Figures showing electron densities and atomic models were generated using either UCSF Chimera (***Pettersen et al., 2004***) or PyMol Molecular Graphics Systems (Version 1.8 Schrödinger, LLC,).

Accession codes

The cryo-electron microscopy map for the VemP-SRC has been deposited in the EMDataBank with the accession code EMD-3713. The respective coordinates for electron-microscopy-based model of the VemP-SRC are deposited in the ProteinDataBank (5NWY).

Acknowledgements

We thank our technical team, especially Charlotte Ungewickell, and IT support, particularly André Heuer and Christian Schmidt. This research was supported by grants from the Deutsche Forschungsgemeinschaft GRK 1721 and FOR1805 (to RB and DNW), a DFG fellowship through the Graduate School of Quantitative Biosciences Munich (QBM, to TS) and the European Research Council (Advanced Grant CRYOTRANSLATION to RB), and the Swedish Cancer Foundation, the Swedish Research Council and the Knut and Alice Wallenberg Foundation (to GvH).

Additional information

Funding

Funder	Grant reference number	Author
Graduate School of Quantitative Biosciences Munich	Graduate Student Fellowship	Ting Su
Cancerfonden		Gunnar von Heijne
Vetenskapsrådet		Gunnar von Heijne
Knut och Alice Wallenbergs Stiftelse		Gunnar von Heijne
Deutsche Forschungsgemeinschaft	FOR1805	Daniel N Wilson
Deutsche Forschungsgemeinschaft	FOR1805	Roland Beckmann
European Research Council		Roland Beckmann
Deutsche Forschungsgemeinschaft	GRK1721	Roland Beckmann

The funders had no role in study design, data collection and interpretation, or the decision to submit the work for publication.

Author contributions

TS, Writing—original draft, Writing—review and editing, Sample preparation, Cryo-EM data processing, model building and refinement; JC, Cryo-EM model building and refinement; DS, Helped with sample preparation, cryo-EM data processing and model building; RH, Pulse-labeling analysis; OB, cryo-EM data collection; GvH, Supervision, Writing—original draft, Writing—review and editing; DNW, Conceptualization, Supervision, Validation, Writing—original draft, Project administration, Writing—review and editing; RB, Conceptualization, Supervision, Funding acquisition, Validation, Writing—original draft, Project administration, Writing—review and editing

Author ORCIDs

Ting Su, http://orcid.org/0000-0002-3185-8144
Jingdong Cheng, http://orcid.org/0000-0003-4442-377X

Gunnar von Heijne, http://orcid.org/0000-0002-4490-8569
Daniel N Wilson, http://orcid.org/0000-0003-3816-3828
Roland Beckmann, http://orcid.org/0000-0003-4291-3898

Additional files

Major datasets

The following dataset was generated:

Author(s)	Year	Dataset title	Dataset URL	Database, license, and accessibility information
Su T, Cheng J, Sohmen D, Hedman R, Berninghausen O, von Heijne G, Wilson DN, Beckmann R	2017	2.9 A cryo-EM structure of VemP-stalled ribosome-nascent chain complex	http://www.rcsb.org/pdb/explore/explore.do?structureId=5NWY	Publicly available at the RCSBProtein Data Bank (accession no: 5NWY)

References

Adams PD, Afonine PV, Bunkóczi G, Chen VB, Davis IW, Echols N, Headd JJ, Hung LW, Kapral GJ, Grosse-Kunstleve RW, McCoy AJ, Moriarty NW, Oeffner R, Read RJ, Richardson DC, Richardson JS, Terwilliger TC, Zwart PH. 2010. *PHENIX*: a comprehensive Python-based system for macromolecular structure solution. *Acta Crystallographica Section D Biological Crystallography* **66**:213–221. doi: 10.1107/S0907444909052925, PMID: 20124702

Alva V, Nam SZ, Söding J, Lupas AN. 2016. The MPI bioinformatics toolkit as an integrative platform for advanced protein sequence and structure analysis. *Nucleic Acids Research* **44**:W410–W415. doi: 10.1093/nar/gkw348, PMID: 27131380

Arenz S, Bock LV, Graf M, Innis CA, Beckmann R, Grubmüller H, Vaiana AC, Wilson DN. 2016. A combined cryo-EM and molecular dynamics approach reveals the mechanism of ErmBL-mediated translation arrest. *Nature Communications* **7**:12026. doi: 10.1038/ncomms12026, PMID: 27380950

Bhushan S, Gartmann M, Halic M, Armache JP, Jarasch A, Mielke T, Berninghausen O, Wilson DN, Beckmann R. 2010a. alpha-Helical nascent polypeptide chains visualized within distinct regions of the ribosomal exit tunnel. *Nature Structural and Molecular Biology* **17**:313–317. doi: 10.1038/nsmb.1756, PMID: 20139981

Bhushan S, Meyer H, Starosta AL, Becker T, Mielke T, Berninghausen O, Sattler M, Wilson DN, Beckmann R. 2010b. Structural basis for translational stalling by human cytomegalovirus and fungal arginine attenuator peptide. *Molecular Cell* **40**:138–146. doi: 10.1016/j.molcel.2010.09.009, PMID: 20932481

Bhushan S, Hoffmann T, Seidelt B, Frauenfeld J, Mielke T, Berninghausen O, Wilson DN, Beckmann R. 2011. SecM-stalled ribosomes adopt an altered geometry at the peptidyl transferase center. *PLoS Biology* **9**: e1000581. doi: 10.1371/journal.pbio.1000581, PMID: 21267063

Bischoff L, Berninghausen O, Beckmann R. 2014. Molecular basis for the ribosome functioning as an L-tryptophan sensor. *Cell Reports* **9**:469–475. doi: 10.1016/j.celrep.2014.09.011, PMID: 25310980

Brown A, Long F, Nicholls RA, Toots J, Emsley P, Murshudov G. 2015. Tools for macromolecular model building and refinement into electron cryo-microscopy reconstructions. *Acta Crystallographica Section D Biological Crystallography* **71**:136–153. doi: 10.1107/S1399004714021683, PMID: 25615868

Cabrita LD, Cassaignau AM, Launay HM, Waudby CA, Wlodarski T, Camilloni C, Karyadi ME, Robertson AL, Wang X, Wentink AS, Goodsell LS, Woolhead CA, Vendruscolo M, Dobson CM, Christodoulou J. 2016. A structural ensemble of a ribosome-nascent chain complex during cotranslational protein folding. *Nature Structural and Molecular Biology* **23**:278–285. doi: 10.1038/nsmb.3182, PMID: 26926436

Chen VB, Arendall WB, Headd JJ, Keedy DA, Immormino RM, Kapral GJ, Murray LW, Richardson JS, Richardson DC. 2010. MolProbity: all-atom structure validation for macromolecular crystallography. *Acta Crystallographica Section D Biological Crystallography* **66**:12–21. doi: 10.1107/S0907444909042073, PMID: 20057044

Chiba S, Lamsa A, Pogliano K. 2009. A ribosome-nascent chain sensor of membrane protein biogenesis in *Bacillus subtilis*. *The EMBO Journal* **28**:3461–3475. doi: 10.1038/emboj.2009.280, PMID: 19779460

Emsley P, Cowtan K. 2004. *Coot*: model-building tools for molecular graphics. *Acta Crystallographica Section D Biological Crystallography* **60**:2126–2132. doi: 10.1107/S0907444904019158, PMID: 15572765

Fernández JJ, Luque D, Castón JR, Carrascosa JL. 2008. Sharpening high resolution information in single particle electron cryomicroscopy. *Journal of Structural Biology* **164**:170–175. doi: 10.1016/j.jsb.2008.05.010, PMID: 18614378

Fischer N, Neumann P, Bock LV, Maracci C, Wang Z, Paleskava A, Konevega AL, Schröder GF, Grubmüller H, Ficner R, Rodnina MV, Stark H. 2016. The pathway to GTPase activation of elongation factor SelB on the ribosome. *Nature* **540**:80–85. doi: 10.1038/nature20560, PMID: 27842381

Geertsma ER. 2014. FX cloning: a simple and robust high-throughput cloning method for protein expression. *Methods in Molecular Biology* **1116**:153–164. doi: 10.1007/978-1-62703-764-8_11, PMID: 24395363

Gibson DG, Young L, Chuang RY, Venter JC, Hutchison CA, Smith HO. 2009. Enzymatic assembly of DNA molecules up to several hundred kilobases. *Nature Methods* **6**:343–345. doi: 10.1038/nmeth.1318, PMID: 19363495

Holtkamp W, Kokic G, Jäger M, Mittelstaet J, Komar AA, Rodnina MV. 2015. Cotranslational protein folding on the ribosome monitored in real time. *Science* **350**:1104–1107. doi: 10.1126/science.aad0344, PMID: 26612953

Ishii E, Chiba S, Hashimoto N, Kojima S, Homma M, Ito K, Akiyama Y, Mori H. 2015. Nascent chain-monitored remodeling of the Sec machinery for salinity adaptation of marine bacteria. *PNAS* **112**:E5513–E5522. doi: 10.1073/pnas.1513001112, PMID: 26392525

Ismail N, Hedman R, Schiller N, von Heijne G. 2012. A biphasic pulling force acts on transmembrane helices during translocon-mediated membrane integration. *Nature Structural and Molecular Biology* **19**:1018–1022. doi: 10.1038/nsmb.2376, PMID: 23001004

Ito K, Chiba S. 2013. Arrest peptides: cis-acting modulators of translation. *Annual Review of Biochemistry* **82**:171–202. doi: 10.1146/annurev-biochem-080211-105026, PMID: 23746254

Kosolapov A, Deutsch C. 2009. Tertiary interactions within the ribosomal exit tunnel. *Nature Structural and Molecular Biology* **16**:405–411. doi: 10.1038/nsmb.1571, PMID: 19270700

Kucukelbir A, Sigworth FJ, Tagare HD. 2014. Quantifying the local resolution of cryo-EM density maps. *Nature Methods* **11**:63–65. doi: 10.1038/nmeth.2727, PMID: 24213166

Li X, Mooney P, Zheng S, Booth CR, Braunfeld MB, Gubbens S, Agard DA, Cheng Y. 2013. Electron counting and beam-induced motion correction enable near-atomic-resolution single-particle cryo-EM. *Nature Methods* **10**:584–590. doi: 10.1038/nmeth.2472, PMID: 23644547

Lin KF, Sun CS, Huang YC, Chan SI, Koubek J, Wu TH, Huang JJ. 2012. Cotranslational protein folding within the ribosome tunnel influences trigger-factor recruitment. *Biophysical Journal* **102**:2818–2827. doi: 10.1016/j.bpj.2012.04.048, PMID: 22735532

Liu H, Naismith JH. 2008. An efficient one-step site-directed deletion, insertion, single and multiple-site plasmid mutagenesis protocol. *BMC Biotechnology* **8**:91. doi: 10.1186/1472-6750-8-91, PMID: 19055817

Lu J, Deutsch C. 2005. Folding zones inside the ribosomal exit tunnel. *Nature Structural and Molecular Biology* **12**:1123–1129. doi: 10.1038/nsmb1021, PMID: 16299515

Marino J, von Heijne G, Beckmann R. 2016. Small protein domains fold inside the ribosome exit tunnel. *FEBS Letters* **590**:655–660. doi: 10.1002/1873-3468.12098, PMID: 26879042

Matheisl S, Berninghausen O, Becker T, Beckmann R. 2015. Structure of a human translation termination complex. *Nucleic Acids Research* **43**:8615–8626. doi: 10.1093/nar/gkv909, PMID: 26384426

Nakatogawa H, Ito K. 2001. Secretion monitor, SecM, undergoes self-translation arrest in the cytosol. *Molecular Cell* **7**:185–192. doi: 10.1016/S1097-2765(01)00166-6, PMID: 11172723

Nilsson OB, Hedman R, Marino J, Wickles S, Bischoff L, Johansson M, Müller-Lucks A, Trovato F, Puglisi JD, O'Brien EP, Beckmann R, von Heijne G. 2015. Cotranslational protein folding inside the Ribosome exit tunnel. *Cell Reports* **12**:1533–1540. doi: 10.1016/j.celrep.2015.07.065, PMID: 26321634

Nilsson OB, Nickson AA, Hollins JJ, Wickles S, Steward A, Beckmann R, von Heijne G, Clarke J. 2017. Cotranslational folding of spectrin domains via partially structured states. *Nature Structural and Molecular Biology* **24**:221–225. doi: 10.1038/nsmb.3355, PMID: 28112730

Pettersen EF, Goddard TD, Huang CC, Couch GS, Greenblatt DM, Meng EC, Ferrin TE. 2004. UCSF Chimera–a visualization system for exploratory research and analysis. *Journal of Computational Chemistry* **25**:1605–1612. doi: 10.1002/jcc.20084, PMID: 15264254

Rohou A, Grigorieff N. 2015. CTFFIND4: fast and accurate defocus estimation from electron micrographs. *Journal of Structural Biology* **192**:216–221. doi: 10.1016/j.jsb.2015.08.008, PMID: 26278980

Rost B. 2001. Review: protein secondary structure prediction continues to rise. *Journal of Structural Biology* **134**:204–218. doi: 10.1006/jsbi.2001.4336, PMID: 11551180

Rould MA, Perona JJ, Söll D, Steitz TA. 1989. Structure of E. coli glutaminyl-tRNA synthetase complexed with tRNA(Gln) and ATP at 2.8 A resolution. *Science* **246**:1135–1142. doi: 10.1126/science.2479982, PMID: 2479982

Scheres SH. 2012. RELION: implementation of a bayesian approach to cryo-EM structure determination. *Journal of Structural Biology* **180**:519–530. doi: 10.1016/j.jsb.2012.09.006, PMID: 23000701

Schmeing TM, Huang KS, Strobel SA, Steitz TA. 2005. An induced-fit mechanism to promote peptide bond formation and exclude hydrolysis of peptidyl-tRNA. *Nature* **438**:520–524. doi: 10.1038/nature04152, PMID: 16306996

Seidelt B, Innis CA, Wilson DN, Gartmann M, Armache JP, Villa E, Trabuco LG, Becker T, Mielke T, Schulten K, Steitz TA, Beckmann R. 2009. Structural insight into nascent polypeptide chain-mediated translational stalling. *Science* **326**:1412–1415. doi: 10.1126/science.1177662, PMID: 19933110

Sohmen D, Chiba S, Shimokawa-Chiba N, Innis CA, Berninghausen O, Beckmann R, Ito K, Wilson DN. 2015. Structure of the Bacillus subtilis 70S ribosome reveals the basis for species-specific stalling. *Nature Communications* **6**:6941. doi: 10.1038/ncomms7941, PMID: 25903689

Trovato F, O'Brien EP. 2016. Insights into Cotranslational Nascent protein behavior from computer simulations. *Annual Review of Biophysics* **45**:345–369. doi: 10.1146/annurev-biophys-070915-094153, PMID: 27297399

Tu L, Khanna P, Deutsch C. 2014. Transmembrane segments form tertiary hairpins in the folding vestibule of the ribosome. *Journal of Molecular Biology* **426**:185–198. doi: 10.1016/j.jmb.2013.09.013, PMID: 24055377

Vagin AA, Steiner RA, Lebedev AA, Potterton L, McNicholas S, Long F, Murshudov GN. 2004. *REFMAC* 5 dictionary: organization of prior chemical knowledge and guidelines for its use. *Acta Crystallographica Section D Biological Crystallography* **60**:2184–2195. doi: 10.1107/S0907444904023510

Wilson DN, Arenz S, Beckmann R. 2016. Translation regulation via nascent polypeptide-mediated ribosome stalling. *Current Opinion in Structural Biology* **37**:123–133. doi: 10.1016/j.sbi.2016.01.008, PMID: 26859868

Woolhead CA, McCormick PJ, Johnson AE. 2004. Nascent membrane and secretory proteins differ in FRET-detected folding far inside the ribosome and in their exposure to ribosomal proteins. *Cell* **116**:725–736. doi: 10.1016/S0092-8674(04)00169-2, PMID: 15006354

Youngman EM, Brunelle JL, Kochaniak AB, Green R. 2004. The active site of the ribosome is composed of two layers of conserved nucleotides with distinct roles in peptide bond formation and peptide release. *Cell* **117**: 589–599. doi: 10.1016/S0092-8674(04)00411-8, PMID: 15163407

Zhang J, Pan X, Yan K, Sun S, Gao N, Sui SF. 2015. Mechanisms of ribosome stalling by SecM at multiple elongation steps. *eLife* **4**:e09684. doi: 10.7554/eLife.09684, PMID: 26670735

2.2 Publication 2 | Structure and function of Vms1 and Arb1 in RQC and mitochondrial proteome homeostasis

LETTER

Corrected: Publisher Correction

https://doi.org/10.1038/s41586-019-1307-z

Structure and function of Vms1 and Arb1 in RQC and mitochondrial proteome homeostasis

Ting Su[1,6], Toshiaki Izawa[2,3,4,6], Matthias Thoms[1], Yui Yamashita[5], Jingdong Cheng[1], Otto Berninghausen[1], F. Ulrich Hartl[3], Toshifumi Inada[4], Walter Neupert[2,3]* & Roland Beckmann[1]*

Ribosome-associated quality control (RQC) provides a rescue pathway for eukaryotic cells to process faulty proteins after translational stalling of cytoplasmic ribosomes[1–6]. After dissociation of ribosomes, the stalled tRNA-bound peptide remains associated with the 60S subunit and extended by Rqc2 by addition of C-terminal alanyl and threonyl residues (CAT tails)[7–9], whereas Vms1 catalyses cleavage and release of the peptidyl-tRNA before or after addition of CAT tails[10–12]. In doing so, Vms1 counteracts CAT-tailing of nuclear-encoded mitochondrial proteins that otherwise drive aggregation and compromise mitochondrial and cellular homeostasis[13]. Here we present structural and functional insights into the interaction of *Saccharomyces cerevisiae* Vms1 with 60S subunits in pre- and post-peptidyl-tRNA cleavage states. Vms1 binds to 60S subunits with its Vms1-like release factor 1 (VLRF1), zinc finger and ankyrin domains. VLRF1 overlaps with the Rqc2 A-tRNA position and interacts with the ribosomal A-site, projecting its catalytic GSQ motif towards the CCA end of the tRNA, its Y285 residue dislodging the tRNA A73 for nucleolytic cleavage. Moreover, in the pre-state, we found the ABCF-type ATPase Arb1 in the ribosomal E-site, which stabilizes the delocalized A73 of the peptidyl-tRNA and stimulates Vms1-dependent tRNA cleavage. Our structural analysis provides mechanistic insights into the interplay of the RQC factors Vms1, Rqc2 and Arb1 and their role in the protection of mitochondria from the aggregation of toxic proteins.

Translational stalling in the cytoplasm of eukaryotes results in the dissociation of ribosomes with the peptidyl-tRNA remaining bound to the large subunit (60S), to which the RQC components Rqc1, listerin (Ltn1 in yeast), Rqc2, Cdc48 and the anti-association factor eIF6 (Tif6 in yeast) bind[1–7]. Rqc2 adds CAT tails, and the E3 ligase Ltn1 ubiquitylates the nascent peptide[1,7–9]. As a result, stalled polypeptides are extracted from the ribosome by the AAA-ATPase Cdc48 and delivered to the proteasome system for degradation[2–4]. However, the presence of CAT tails can cause aggregation of the released peptides with other proteins in the cytosol and also in mitochondria, where they have toxic effects[13–16]. Vms1 cleaves peptidyl-tRNA before or after CAT-tailing and has been shown to antagonize CAT-tail-dependent mitochondrial toxicity[10–13]. However, the molecular mechanisms by which Vms1 antagonizes Rqc2 and acts as a peptidyl-tRNA hydrolase are poorly understood.

We affinity-purified Vms1–60S complexes from *vms1*Δ cells expressing Myc-tagged Vms1 lacking the C-terminal VIM domain, as this Cdc48-recruiting domain is dispensable for the protective and release activity of Vms1[10,13]. To functionally characterize the role of the GSQ motif, which was suggested to be central for Vms1 peptidyl-tRNA cleavage activity, we used Vms1(ΔVIM) and Vms1(ΔVIM/Q295L), which has largely impaired cleavage activity[10,11]. The purified complexes contained Vms1 and 60S ribosomal proteins but, in contrast to complexes with wild-type (WT) Vms1, there was no Cdc48 ATPase (Extended Data Fig. 1a).

Cryo-electron microscopy (cryo-EM) analysis was performed with the purified complexes containing Vms1(ΔVIM) and Vms1(ΔVIM/Q295L); classification (Extended Data Fig. 1b–e and Extended Data Table 1) resulted in two main reconstructions at average resolutions of 3.4 Å (Extended Data Fig. 2a). Both maps showed typical 60S ribosomal subunits with additional densities representing Tif6 near the sarcin–ricin loop (SRL)[17] and distinct Vms1 domains at the intersubunit surface of the 60S subunit (Fig. 1a). Of note, we observed density corresponding to a tRNA and a connected nascent polypeptide chain only in the Vms1(ΔVIM/Q295L) reconstruction. This indicates that the mutated GSQ construct resulted in stabilization and enrichment of the peptidyl-tRNA before cleavage (hereafter, 'pre-state'), whereas the wild-type GSQ construct represented a state after peptidyl-tRNA cleavage and release (hereafter, 'post-state') (Fig. 1a).

The maps enabled identification and molecular model docking or building of three distinct Vms1 domains on the 60S subunit (Fig. 1b and Extended Data Fig. 2b–d). The first domain, recently defined as Vms1-like release factor 1 domain (VLRF1)[11], and the leucine-rich sequence (LRS) bound in and below the A-site, interacting mainly with rRNA helices 69 and 71 (H69 and H71) and the peptidyl-tRNA. The finger-like domain carrying the catalytically active GSQ loop reached towards the CCA end of the tRNA (Fig. 1c). The conformation of the VLRF1 domain is essentially the same in pre- and post-states, with a small shift towards the P site in the presence of peptidyl-tRNA (Extended Data Fig. 2e). The second domain containing a zinc finger domain of Vms1 interacted with Tif6 (Fig. 1d and Extended Data Fig. 2c), and the third domain, consisting of the Vms1 ankyrin-repeat domain (AnkR) and the coiled-coil domain (CC; comprising one helix), bound between the rRNA H101 and the rRNA expansion segment 27 (ES27) (Fig. 1d). The CC domain was only partially visible and pointed towards the ribosomal tunnel exit where the following VIM domain would coordinate the Cdc48 ATPase during peptide extraction (Extended Data Fig. 2f). To test the contribution of the AnkR and CC domains to the Vms1–60S interaction we generated deletion constructs. In contrast to deletion of the CC domain, deletion of the AnkR domain reduced the yield of co-purified 60S subunits, confirming its contribution to the affinity of Vms1 for the 60S subunit (Extended Data Fig. 2g). However, Vms1(ΔAnkR), Vms1(ΔZnF) and the double deletion (Vms1(ΔAnkR/ΔZnF)) could still rescue the growth defect of *vms1*Δ*ltn1*Δ cells under respiratory conditions, prevented formation of SDS-insoluble aggregates of a mitochondrial nonstop GFP (NS-mtGFP) reporter and allowed the maturation of the mitochondrial Rieske protein (Rip1), an indicator of mitochondrial proteome integrity[13] (Extended Data Fig. 2h–j). Although this indicates that the VLRF1 domain alone is sufficient to provide the affinity for functional activity, the canonical Vms1 binding to the 60S subunit is established by a tri-modal interaction pattern consisting mainly of the VLRF1 domain in the ribosomal A-site, assisted by the ZnF and AnkR domains.

[1]Gene Center and Center for Integrated Protein Science Munich, Department of Biochemistry, University of Munich, Munich, Germany. [2]Department of Cell Biology, Medical Faculty, University of Munich, Martinsried, Germany. [3]Department of Cellular Biochemistry, Max Planck Institute of Biochemistry, Martinsried, Germany. [4]Graduate School of Pharmaceutical Sciences, Tohoku University, Sendai, Japan. [5]Graduate School of Agriculture, Hokkaido University, Sapporo, Japan. [6]These authors contributed equally: Ting Su, Toshiaki Izawa. *e-mail: walter.neupert@med.uni-muenchen.de; beckmann@genzentrum.lmu.de

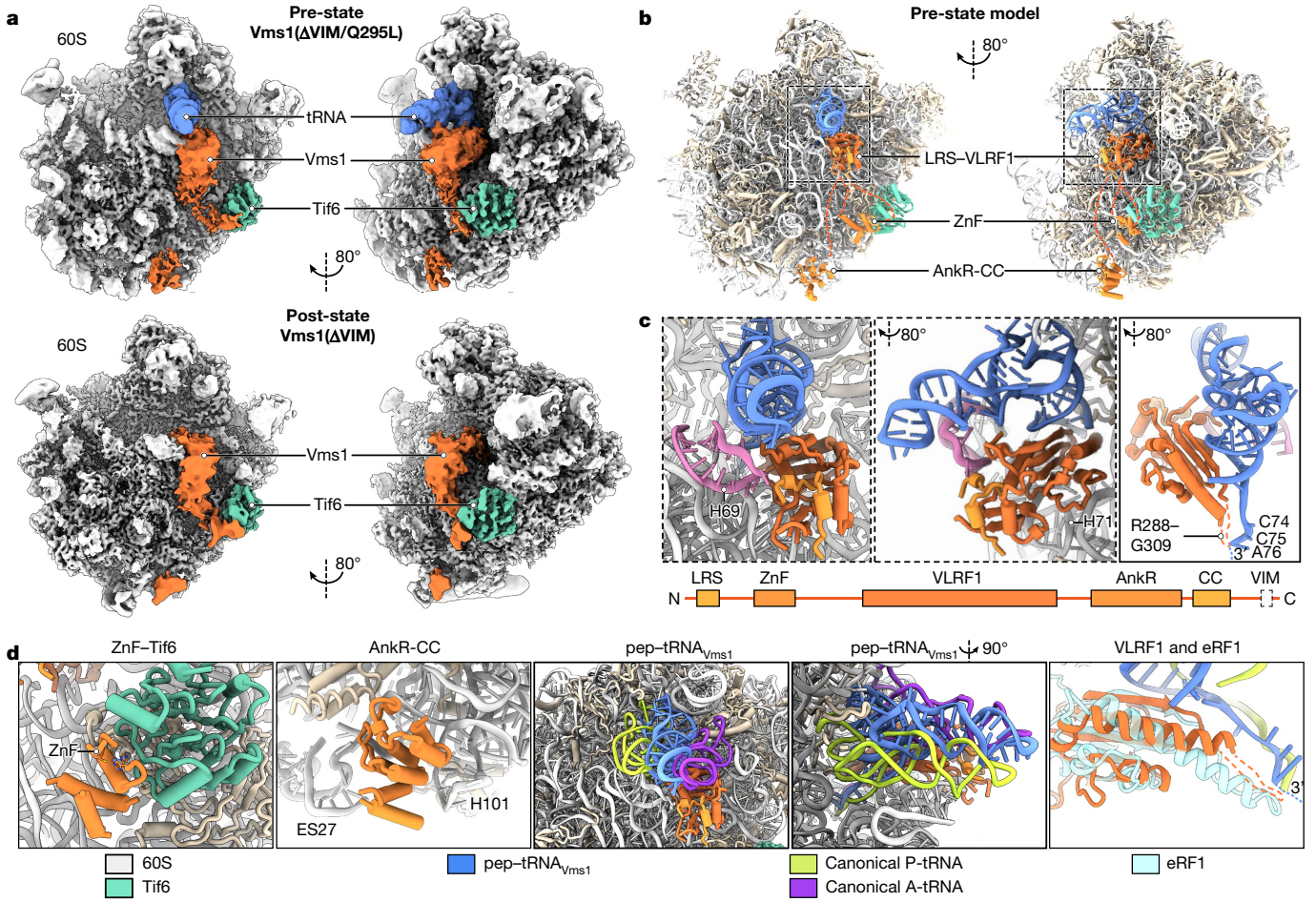

Fig. 1 | Structural analysis of Vms1-bound 60S ribosomal subunits in pre- and post-cleavage states of peptidyl-tRNA. a, Cryo-EM reconstructions of the Vms1–60S particles in two orientations. Top row, the pre-state purified via Vms1(ΔVIM/Q295L); bottom row, the post-state purified via Vms1(ΔVIM). Electron density is displayed at multiple contour levels (see Methods). **b**, Molecular model of the pre-state complex with labelled Vms1 LRS and VLRF1 domains, ZnF, AnkR and CC domains. **c**, Magnified view of the area outlined in **b**, illustrating the interaction of the VLRF1 domain (orange) with peptidyl-tRNA (blue) and 25S rRNA helix H69 (pink) from three angles. The disordered loop harbouring the mutated GSQ motif (R288–G309) is indicated as a dashed line. The domain organization of Vms1 is shown below. **d**, Left to right: interaction of the Vms1 ZnF domain with Tif6; the AnkR-CC domain bound between 25S rRNA helices H101 and ES27; comparison of peptidyl-$tRNA_{Vms1}$ (pep–$tRNA_{Vms1}$) and canonical A-site and P-site tRNA (Protein Data Bank (PDB) ID 5GAK) in two orientations; and superposition of the VLRF1 domain (the disordered loop with the GSQ motif in dashed line) and the release factor eRF1 (PDB ID 5LZU).

The peptidyl-tRNA in the pre-state particle ($tRNA_{Vms1}$) was found between the A- and P-sites (Fig. 1d) with its CCA end coordinated by the ribosomal P loop and clearly connected to a nascent peptide (Extended Data Fig. 2c). Although disordered, the GSQ loop region of the VLRF1 domain (R288–G309) was positioned near the CCA, similar to the canonical termination factor eRF1 (Fig. 1d). However, the catalytic loop of Vms1 displayed a unique interaction with the tRNA, as its conserved Y285 stacked with the tRNA base in position 72 (here C72). As a result, the base in position 73 (in most cases, A73) is displaced and the phosphate backbone is exposed (Fig. 2a, b and Extended Data Fig. 2k). As this tyrosine is missing in canonical release factors (Fig. 2b), we tested its importance in an in vitro release assay[10]. After translation of a non-stop RQC substrate with a 3×Flag tag (NS-3×Flag) in a cell-free extract generated from *vms1*Δ*ski2*Δ cells, the stalled peptidyl-tRNA can be released by the addition of purified recombinant Vms1 (see Methods). As expected, with wild-type Vms1 we observed a decrease of the peptidyl-tRNA substrate signal and detection of a lower-molecular-weight signal representing the released peptide. These combined signals are indicative of peptidyl-tRNA cleavage (Fig. 2c). Compared with wild-type Vms1, Vms1(Q295L) and Vms1(Y285A) mutants displayed reduced release activity (described previously for Q295L[10]). Notably, the Vms1(Q295L/Y285A) double mutation resulted in a complete loss of activity (Fig. 2c). This supports the notion that Y285 contributes to the catalytic activity of Vms1 but in a mechanistically distinct way from canonical release factors. Notably, the human homologue ANKZF1 was recently discovered to display tRNA nuclease activity[12], which releases the polypeptide with some nucleotides still attached. Therefore, we tested Vms1 for nuclease activity by adding RNase A in our in vitro assay to degrade any remaining peptide-bound oligonucleotide. Peptidyl-tRNA and peptide signals disappeared and collapsed to the molecular weight of the free peptide (Fig. 2d). Consistent with a recent report[18], this shows that Vms1 is also a tRNA nuclease, and that its cleavage mechanism involves remodelling and cleavage of the ribose-phosphate backbone of the tRNA by Y285 and the GSQ motif, respectively.

In vivo, the function of Vms1 in protecting mitochondria is dependent on its Rqc2-antagonizing activity. Overexpression of Vms1 triggers displacement of Rqc2 from ribosomal subunits[13], and we observed a direct steric clash between the Rqc2 A-tRNA (A-$tRNA_{Rqc2}$) complex and the Vms1 VLRF1 domain with the $tRNA_{Vms1}$ (Fig. 2e). Therefore, we tested in vivo whether the Vms1(Q295L), Vms1(Y285A) or Vms1(Q295L/Y285A) mutants were able to rescue the growth defect of *vms1*Δ*ltn1*Δ cells under respiratory conditions. Indeed, Vms1(Q295L) and Vms1(Y285A) rescued the growth defect and enabled maturation of the mitochondrial Rip1 protein; however, Vms1(Q295L/Y285A), which completely lacked release activity, could not rescue the growth

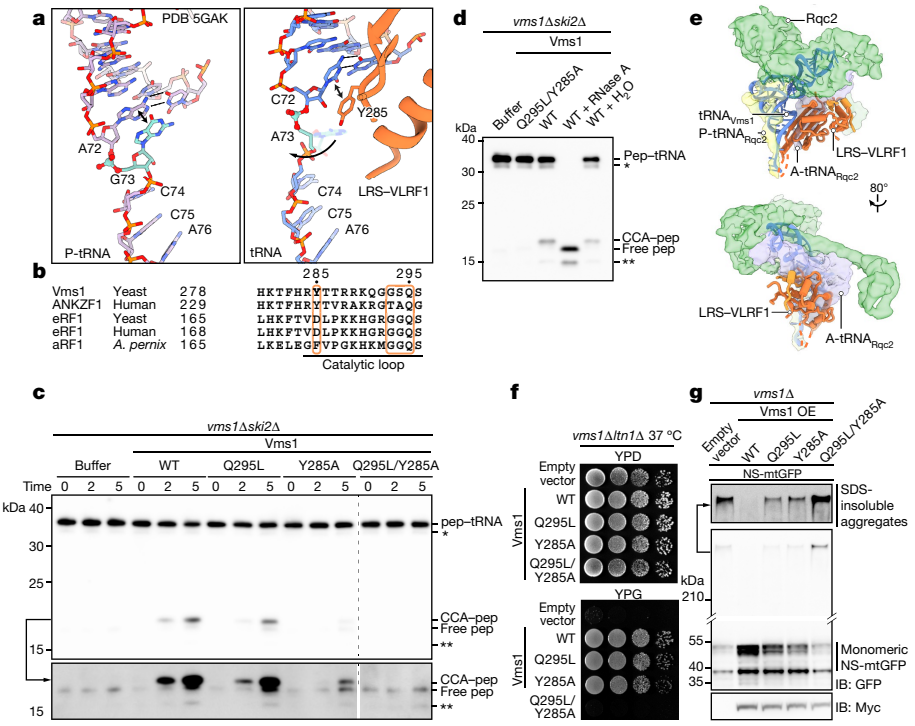

Fig. 2 | Vms1 exhibits nuclease activity, which is required to antagonize Rqc2. a, Comparison of a canonical P-tRNA from eIF5A-bound ribosomes (left) and the $tRNA_{Vms1}$ in the pre-state (right). **b**, Sequence alignment of yeast Vms1, human ANKZF1, yeast eRF1, human eRF1 and *Aeropyrum pernix* aRF1, starting at the indicated residue number. The catalytic loop and residues Y285 and Q295 are outlined. **c**, Yeast in vitro release reaction of the arrested peptides translated from a non-stop RQC reporter mRNA NS-3×Flag in lysate from *vms1Δski2Δ* cells. Buffer, Vms1(WT) or the indicated Vms1 mutants were added to a cycloheximide-treated (stopped) translation reaction and incubated for 0, 2 or 5 min at 25 °C. Top, samples were analysed by immunoblotting with Flag antibody. Bottom, a longer exposure of the low molecular weight region of the same blot. CCA, CCA from the tRNA 3′ end; pep, peptide; * and ** indicate peptidyl-tRNA and free peptide from the colliding ribosome, respectively. **d**, Yeast in vitro release reaction as described in **c**. Samples were incubated with buffer, Vms1(Q295L/Y285A) or Vms1(WT) at 25 °C for 5 min. The Vms1(WT) samples were further incubated with either RNase A or H_2O for 5 min at room temperature. **e**, Model illustrating the steric clash of the Vms1 VLRF1 domain and $tRNA_{Vms1}$ with Rqc2, P-$tRNA_{Rqc2}$ and A-$tRNA_{Rqc2}$ (Electron Microscopy Data Bank 2812) on the 60S subunit. **f**, The *vms1Δltn1Δ* strain was transformed with empty vector or constructs expressing Vms1(WT) or the indicated mutants expressed from the endogenous *VMS1* promoter. Cells were spotted on YPD or YPG plates and grown at 37 °C. **g**, *Vms1Δ* cells expressing the NS-mtGFP reporter and overexpressing (OE) indicated Myc-tagged Vms1 constructs from the *GPD1* promoter. Cell extracts were analysed by immunoblotting with the indicated antibodies. SDS-insoluble aggregates are shown with a longer exposure (top).

defect and prevented maturation of Rip1 (Fig. 2f and Extended Data Fig. 2j). Consistently, the formation of SDS-insoluble aggregates of the NS-mtGFP reporter in *vms1Δ* cells could be fully prevented by overexpression of wild-type Vms1 and partially prevented by Vms1(Q295L) or Vms1(Y285A); however, Vms1(Q295L/Y285A) did not prevent formation of the aggregates (Fig. 2g and Extended Data Fig. 2g). Taken together, the Rqc2-antagonizing activity of Vms1 in mitochondrial RQC may be partially provided by steric competition with Rqc2; however, it also requires peptide-release activity.

Surprisingly, a large class of the Vms1 pre-state particles contained an additional protein, identified as the ABCF-type ATPase Arb1 (Fig. 3a and Extended Data Figs. 1d, 3a–c), which is known to be involved in ribosome biogenesis and to co-purify with Vms1[19]. Its two nucleotide-binding domains (NBDs) were located in the ribosomal E-site and its leg domain (LD) protruded towards the tRNA CCA end (Fig. 3a–e and Extended Data Fig. 3d), similar to bacterial ABCF-type ATPases on 70S ribosomes[20–22]. Arb1 NBD1 contacted the L1 stalk (mainly uL1) whereas NBD2 interacted with uL5, and both NBDs interacted with eL42. The LD ran parallel to rRNA H68 and its loop reached the acceptor arm of the tRNA opposite the Vms1 GSQ loop (Fig. 3b, c). The two NBDs adopted a flexible but clearly open-state conformation (Extended Data Fig. 3e, f); nevertheless, it was possible to build a de novo molecular model of the LD (Fig. 3b, c and Extended Data Fig. 3c, d). Similar to Vms1, Arb1 would sterically clash with Rqc2 (Extended Data Fig. 3g), however, overexpression of Arb1 did not dissociate Rqc2 from ribosomes[13] (Extended Data Fig. 3h).

Arb1 interacted with the $tRNA_{Vms1}$ by forming an unusual triple stack comprising Y346 in the loop (A343–Y346) of the Arb1 LD, the nucleobase 73 of the tRNA (here A73) and A2971 of the 25S rRNA (A2602 in *Escherichia coli*) (Fig. 3d, e and Extended Data Fig. 3i). This requires rotation of A2971 by about 180° and stabilizes the dislocated A73 of the tRNA in a distinct position (Extended Data Fig. 3j). The tRNA phosphate backbone is thereby exposed to Vms1 VLRF1 and to the conformation-altered loop S103–Q111 of uL16 near T345 of Arb1 (Extended Data Fig. 3o). To test whether Arb1 contributes to peptide release, we used our in vitro assay with recombinant Arb1 and cell extracts from either *vms1Δski2Δ* or *vms1Δ arb1* degron cells[23] (Fig. 3f and Extended Data Fig. 3k, l). Addition of Arb1 to varying amounts of Vms1 increased release of peptide, indicating that Arb1 can indeed stimulate the release activity of Vms1 (Fig. 3f and Extended Data Fig. 3l). Next, we tested the function of Arb1 in the context of mitochondrial RQC in vivo. Overexpression of wild-type Arb1, but not of mutant constructs deficient in ATP binding (Arb1(G229D/G230E/G519D); hereafter, Arb1(DED))[19] or carrying a truncated LD domain (Arb1(Δ343–348)), or Arb1(Y346A), could rescue the growth defect and the Rip1 maturation defect of *vms1Δltn1Δ* cells (Fig. 3g, h). These results support a function of Arb1 in mitochondrial RQC. Furthermore, as the assays were also performed in vivo in *vms1Δ* cells, they also suggest that Arb1 has Vms1-independent Rqc2-antagonizing activity. To test for a role of Arb1 in cytosolic RQC, we used an in vivo reporter assay, in which expression of a nonstop cytoplasmic GFP (NS-cGFP) construct in *ltn1Δ* and *vms1Δltn1Δ* cells results in the formation of aggregates. Consistent with a general role in RQC, the

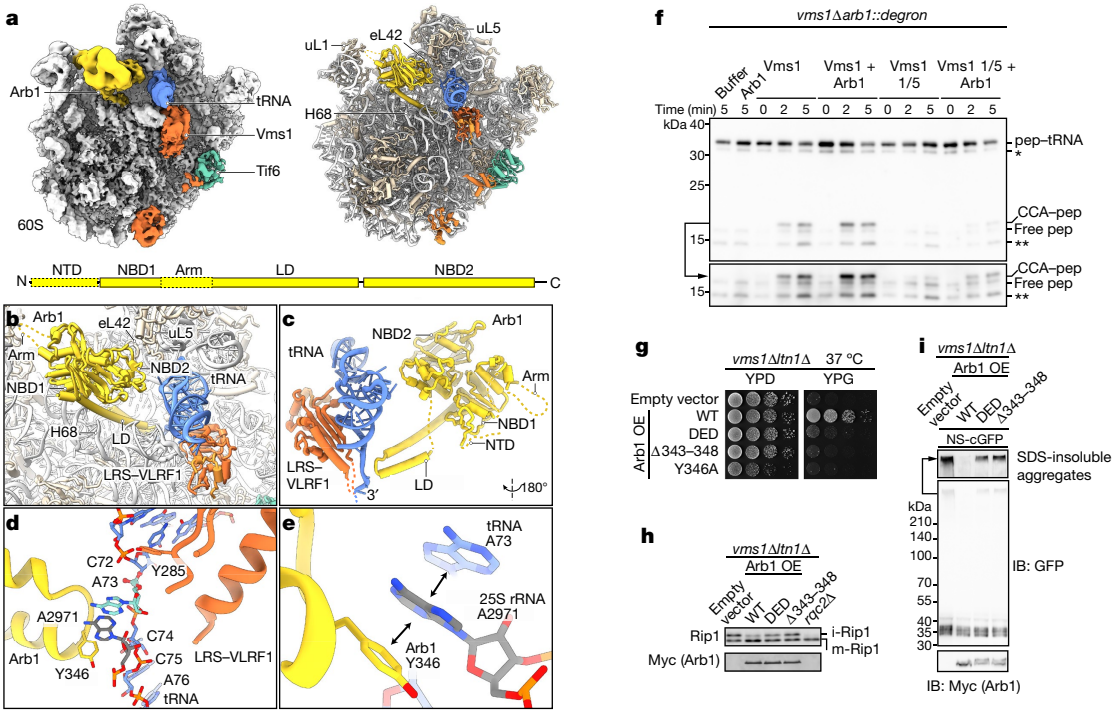

Fig. 3 | Arb1 is genetically and physically linked to RQC and stimulates the nuclease activity of Vms1. a, Cryo-EM reconstruction (top left) and molecular model (top right) of pre-state Vms1–60S particles containing Arb1. See Methods for density contour levels used. Bottom, domain organization of Arb1. NTD, N-terminal domain. **b**, Positioning and interaction of Arb1 with the 60S subunit. **c**, Same as **b**, rotated 180° and shown without the 60S model. The Arb1 LD loop near the tRNA CCA end juxtaposed with the Vms1 GSL loop. **d**, $tRNA_{Vms1}$ in the presence of Arb1. **e**, Triple-stack model of Arb1 Y346, 25S rRNA A2971 and tRNA nucleobase A73. **f**, Yeast in vitro release reaction of the arrested peptides translated from the NS-3×Flag reporter mRNA in a *vms1Δ arb1*::degron lysate depleted for Arb1, incubated for 0, 2 or 5 min at 25 °C. Vms1 and Arb1 were added at 1 to 5 (Vms1 + Arb1) or 1 to 25 (Vms1 1/5 + Arb1) molar ratios. Bottom, same blot with a longer exposure. **g**, *vms1Δltn1Δ* cells overexpressing indicated Arb1–Myc constructs from the *GPD1* promoter were grown on YPD or YPG plates at 37 °C. **h**, *vms1Δltn1Δ* cells transformed with indicated Arb1–Myc constructs (see **g**) or *vms1Δltn1Δrqc2Δ* cells were grown at 30 °C. Cell extracts were analysed by immunoblotting with indicated antibodies. i-Rip1, intermediate Rip1; m-Rip1, mature Rip1. **i**, *vms1Δltn1Δ* cells expressing the NS-cGFP reporter and overexpressing indicated Arb1–Myc constructs. Cell extracts were analysed by immunoblotting with indicated antibodies. Top blot is a longer exposure of the SDS-insoluble aggregates from the same blot.

overexpression of Arb1 prevented aggregate formation, whereas Arb1(DED) and Arb1(Δ343–348) had very limited effects, despite their interactions with Vms1–60S (Fig. 3i and Extended Data Fig. 3m, n). Notably, the Arb1(Y346A) mutation displayed a dominant-negative phenotype upon overexpression, and was therefore not analysed further. We conclude that Arb1 has a general function in RQC, most likely through stimulation of the peptidyl-tRNA-release activity of Vms1 and by steric interference with Rqc2. Moreover, similar to the

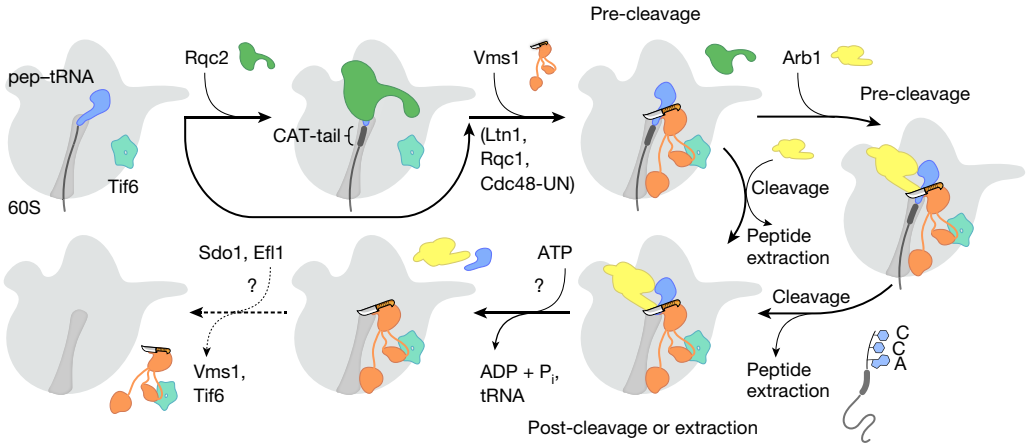

Fig. 4 | Mechanistic model of Vms1, Rqc2 and Arb1 activities in RQC. Clockwise, from top left. After dissociation of the 80S ribosome, the peptidyl-tRNA bound 60S subunit is recognized by Rqc2 to initiate CAT-tailing. This is accompanied by binding of Rqc1 and Ltn1, and recruitment of the Cdc48 peptide extraction machinery (Cdc48-UN). The CAT-tailing process can be terminated at variable points by Vms1 competing with Rqc2 and nucleolytic release of peptidyl-tRNA. This may be aided by positioning and remodelling of the tRNA by Arb1. Accumulation of toxic CAT-tailed proteins in the mitochondrial matrix is prevented by the concerted activity of Ltn1-triggered proteasomal degradation and by the activity of Vms1 on the mitochondrial surface (Extended Data Fig. 4). Arb1 may be able to dislocate the deacylated tRNA and, after dissociation of Vms1 and Tif6, the rescued 60S subunit can be used for another round of translation. Sdo1 and Efl1 are Tif6-release factors in yeast (the human equivalents are SBDS and EFL1, respectively)[24].

bacterial ABCF ATPases MsrE and VmlR[21,22], Arb1 may switch from the observed open state to a closed state on ATP binding and hydrolysis. We therefore speculate that Arb1 may also dislocate tRNA from the 60S subunit and have a role in the extraction of the tRNA before or after cleavage (Extended Data Fig. 3p).

In summary, we suggest a mechanistic model for RQC, in which Rqc2-dependent CAT-tailing can be terminated by nucleolytic Vms1 and Arb1, and these factors cooperate to antagonize CAT-tail-driven mitochondrial toxicity (Fig. 4 and Extended Data Fig. 4).

Online content

Any methods, additional references, Nature Research reporting summaries, source data, extended data, supplementary information, acknowledgements, peer review information; details of author contributions and competing interests; and statements of data and code availability are available at https://doi.org/10.1038/s41586-019-1307-z.

Received: 1 October 2018; Accepted: 16 May 2019;
Published online 12 June 2019.

1. Bengtson, M. H. & Joazeiro, C. A. Role of a ribosome-associated E3 ubiquitin ligase in protein quality control. *Nature* **467**, 470–473 (2010).
2. Brandman, O. et al. A ribosome-bound quality control complex triggers degradation of nascent peptides and signals translation stress. *Cell* **151**, 1042–1054 (2012).
3. Defenouillère, Q. et al. Cdc48-associated complex bound to 60S particles is required for the clearance of aberrant translation products. *Proc. Natl Acad. Sci. USA* **110**, 5046–5051 (2013).
4. Verma, R., Oania, R. S., Kolawa, N. J. & Deshaies, R. J. Cdc48/p97 promotes degradation of aberrant nascent polypeptides bound to the ribosome. *eLife* **2**, e00308 (2013).
5. Brandman, O. & Hegde, R. S. Ribosome-associated protein quality control. *Nat. Struct. Mol. Biol.* **23**, 7–15 (2016).
6. Joazeiro, C. A. P. Mechanisms and functions of ribosome-associated protein quality control. *Nat. Rev. Mol. Cell Biol.* **20**, 368–383 (2019).
7. Shen, P. S. et al. Rqc2p and 60S ribosomal subunits mediate mRNA-independent elongation of nascent chains. *Science* **347**, 75–78 (2015).
8. Kostova, K. K. et al. CAT-tailing as a fail-safe mechanism for efficient degradation of stalled nascent polypeptides. *Science* **357**, 414–417 (2017).
9. Osuna, B. A., Howard, C. J., Kc, S., Frost, A. & Weinberg, D. E. In vitro analysis of RQC activities provides insights into the mechanism and function of CAT tailing. *eLife* **6**, e27949 (2017).
10. Zurita Rendón, O. et al. Vms1p is a release factor for the ribosome-associated quality control complex. *Nat. Commun.* **9**, 2197 (2018).
11. Verma, R. et al. Vms1 and ANKZF1 peptidyl-tRNA hydrolases release nascent chains from stalled ribosomes. *Nature* **557**, 446–451 (2018).
12. Kuroha, K., Zinoviev, A., Hellen, C. U. T. & Pestova, T. V. Release of ubiquitinated and non-ubiquitinated nascent chains from stalled mammalian ribosomal complexes by ANKZF1 and Ptrh1. *Mol. Cell* **72**, 286–302 (2018).
13. Izawa, T., Park, S. H., Zhao, L., Hartl, F. U. & Neupert, W. Cytosolic protein Vms1 links ribosome quality control to mitochondrial and cellular homeostasis. *Cell* **171**, 890–903 (2017).
14. Choe, Y. J. et al. Failure of RQC machinery causes protein aggregation and proteotoxic stress. *Nature* **531**, 191–195 (2016).
15. Defenouillère, Q. et al. Rqc1 and Ltn1 prevent C-terminal alanine-threonine tail (CAT-tail)-induced protein aggregation by efficient recruitment of Cdc48 on stalled 60S subunits. *J. Biol. Chem.* **291**, 12245–12253 (2016).
16. Yonashiro, R. et al. The Rqc2/Tae2 subunit of the ribosome-associated quality control (RQC) complex marks ribosome-stalled nascent polypeptide chains for aggregation. *eLife* **5**, e11794 (2016).
17. Gartmann, M. et al. Mechanism of eIF6-mediated inhibition of ribosomal subunit joining. *J. Biol. Chem.* **285**, 14848–14851 (2010).
18. Yip, M. C. J. et al. Mechanism for recycling tRNAs on stalled ribosomes. *Nat. Struct. Mol. Biol.* **26**, 343–349 (2019).
19. Dong, J., Lai, R., Jennings, J. L., Link, A. J. & Hinnebusch, A. G. The novel ATP-binding cassette protein ARB1 is a shuttling factor that stimulates 40S and 60S ribosome biogenesis. *Mol. Cell. Biol.* **25**, 9859–9873 (2005).
20. Chen, B. et al. EttA regulates translation by binding the ribosomal E site and restricting ribosome-tRNA dynamics. *Nat. Struct. Mol. Biol.* **21**, 152–159 (2014).
21. Crowe-McAuliffe, C. et al. Structural basis for antibiotic resistance mediated by the *Bacillus subtilis* ABCF ATPase VmlR. *Proc. Natl Acad. Sci. USA* **115**, 8978–8983 (2018).
22. Su, W. et al. Ribosome protection by antibiotic resistance ATP-binding cassette protein. *Proc. Natl Acad. Sci. USA* **115**, 5157–5162 (2018).
23. Nishimura, K., Fukagawa, T., Takisawa, H., Kakimoto, T. & Kanemaki, M. An auxin-based degron system for the rapid depletion of proteins in nonplant cells. *Nat. Methods* **6**, 917–922 (2009).
24. Weis, F. et al. Mechanism of eIF6 release from the nascent 60S ribosomal subunit. *Nat. Struct. Mol. Biol.* **22**, 914–919 (2015).

METHODS

Data reporting. No statistical methods were used to predetermine sample size. The experiments were not randomized. The investigators were not blinded to allocation during experiments and outcome assessment.

Yeast strains and growth conditions. Strains used in this study were derived from BY4742 (*MATα his3Δ1 leu2Δ0 lys2Δ0 ura3Δ0*). W303 (*MATα ade2-1 his3-11,15 leu2-3 trp1-1 ura3-1 can1-100*) was used for overexpression and purification of Arb1. Standard gene disruption and tagging methods were applied to generate the *S. cerevisiae* strains[25,26] and strains used in this study are listed in Extended Data Table 2. Cells were grown in YP rich medium or synthetic complete (SC) medium at 30 °C or 37 °C. The respective media contained 2% glucose (YPD, SCD), 3% galactose (YPGal, SCGal), 2% raffinose plus 2% galactose (SCRafGal) or 3% glycerol (YPG).

Growth analysis. Cells were grown in SCD or YPD medium at 30 °C and spotted in tenfold dilution steps on YPD (fermentable carbon source) or YPG plates (non-fermentable carbon source). YPD and YPG plates were incubated for two days and for three-to-four days, respectively.

Plasmid construction. Plasmids were constructed using standard recombinant DNA techniques, Gibson assembly cloning (Gibson Assembly kit, NEB) or FX cloning[27,28] and were verified by sequencing. The *S. cerevisiae* plasmids used and constructed in this study are listed in Extended Data Table 3. The plasmid p7XC3GH (pET26b-based, a gift from R. Dutzler and E. Geertsma (Addgene plasmid 47066)) was used to generate the *E. coli* expression vectors harbouring Vms1(WT), Vms1(Q295L), Vms1(Y285A) or Vms1(Q295L/Y285A) with a C-terminal 3C–GFP–His_{10} tag for protein purification. The plasmid pEX-A2-3FRP was used to generate a linear DNA template for the truncated mRNA harbouring a 3×Flag tag and lacking a stop codon (NS-3×Flag) for the yeast in vitro assays. The construct was based on the reported pEX-A2-His-HA-uL4(1–86)-$(CGA\text{-}CCG)_2$ construct[29] (HA, haemagglutinin). A 3×Flag tag was inserted in the uL4 sequence to generate the His-HA-uL4(1–37)-3×Flag-uL4(38–86)-$(CGA\text{-}CCG)_2$ construct.

Protein expression and purification. The Vms1 constructs fused to a C-terminal 3C–GFP–His_{10} tag were expressed in *E. coli* BL21 (DE3) cells. Cells were grown in LB medium supplemented with kanamycin (35 μg/ml) at 37 °C until they reached an OD_{600} of ~0.6 and were subsequently shifted to 18 °C. Protein expression was induced by the addition of 0.5 mM IPTG and cultures were grown for 15–16 h at 18 °C. Cell pellets were resuspended in lysis buffer containing 20 mM HEPES-NaOH pH 8.0, 300 mM NaCl, 5% glycerol, 0.01% NP40 and supplemented with 20 mM imidazole, cOmplete Protease Inhibitor Cocktail (Roche) and 2 mM ATP and lysed with a M-110L Microfluidizer (Microfluidics). The lysate was cleared by centrifugation at 19,000 r.p.m. for 30 min at 4 °C and the supernatant was incubated with Talon metal-affinity resin (TaKaRa) at 4 °C for 1 h on a turning wheel. The resin was extensively washed with lysis buffer supplemented with 20 mM imidazole. The Talon beads were incubated for 1 h at 4 °C with lysis buffer supplemented with 3C protease. The eluted samples were concentrated with Amicon Ultra centrifugal filter (Millipore) and further purified via size-exclusion chromatography (Superose 6 Increase, GE Healthcare) in buffer containing 20 mM HEPES-KOH pH 7.5, 100 mM KOAc, 2.5 mM $Mg(OAc)_2$, 5% glycerol and 2 mM DTT. Vms1-containing fractions were pooled, concentrated and flash-frozen in liquid nitrogen. Aliquots were stored at −80 °C.

Arb1 was overexpressed in *S. cerevisiae* (W303). Therefore, a YEplac112-Leu2d-*GAL1-10*-Arb1-TEV-ProtA construct was generated. Cell cultures were grown in SCD medium lacking leucine at 30 °C and overexpression was induced by shifting cells to YPGal medium for 20 h at 30 °C. Cells were disrupted by cryo-milling using a 6970EFM Freezer/Mill (SPEX Sample prep) and the cell powder was resuspended in buffer containing 20 mM HEPES pH 7.5, 200 mM NaCl, 10 mM KCl, 5 mM $MgCl_2$, 5% glycerol, 0.01% NP40, 1 mM DTT supplemented with cOmplete Protease Inhibitor Cocktail (Roche). The lysate was cleared by centrifugation at 4,000 r.p.m., 4 °C for 20 min and 17,500 r.p.m., 4 °C for 25 min. IgG Sepharose 6 Fast Flow resin (GE Healthcare) was added to the supernatant and incubated for 2 h at 4 °C on a turning wheel. The beads were extensively washed with lysis buffer and the sample was released from the beads by incubation with TEV protease for 90 min at 23 °C. The eluate was concentrated and further purified by size-exclusion chromatography (Superdex 200 Increase 10/300 GL, GE Healthcare) in buffer containing 20 mM HEPES-KOH pH 7.5, 100 mM KOAc, 2.5 mM $Mg(OAc)_2$, 5% glycerol and 2 mM DTT. Arb1-containing fractions were pooled and concentrated with an Amicon Ultra centrifugal filter (Millipore). Aliquots were flash-frozen in liquid nitrogen and stored at −80 °C.

Yeast in vitro translation and release assay. Extracts were prepared as previously described[29]. The *vms1Δ arb1*::degron culture was treated with 500 μM auxin (final concentration) for 60 min to degrade Arb1–sAid–HA[23]. The linear DNA template for the RQC reporter mRNA NS–3×Flag was prepared by PCR using primers F (GGCCGCAAGCTAATACGACTCAC) and R (AGCCTTTTCAGAAACAGC) and the plasmid 3FRP (see Plasmid construction) as PCR template. The mRNA harbouring His-HA-uL4(1–37)-3×Flag-uL4(38–74) truncation was subsequently generated by T7 mMessage mMachine Kit (Thermo Fisher). The extract was supplemented with 0.8 mM $CaCl_2$ and treated with MNase S7 for 15 min at room temperature. The reaction was stopped by the addition of EGTA to a final concentration of 2 mM. The extract was then supplemented with buffers[29] and 80 ng mRNA per μl extract, and incubated for 45 min at 17 °C. Translation was stopped by adding cycloheximide (100 μg/ml final concentration) to the reaction. The reaction mix was subsequently divided on ice into various tubes containing buffer, Vms1(WT) or Vms1 mutants with or without Arb1. After initial sampling, reaction aliquots were further incubated at 25 °C and sampled at specified time points. When RNase A treatment is indicated, the sample was incubated with 1 μg RNase A (Qiagen) at room temperature for another 5 min. All samples were immediately quenched in Laemmli sample buffer and flash-frozen in liquid nitrogen. Proteins were separated by SDS–PAGE (12% NuPAGE, Thermo Fisher), and 3×Flag-tagged translation products were visualized by immunoblotting with a monoclonal Flag antibody (A8592, Sigma-Aldrich).

Protein sequence alignment. Indicated protein sequences were obtained from Uniprot (P62495, Q9YAF1, Q9H8Y5 and Q04311), aligned via T-Coffee[30,31] followed by manual adjustments and visualized by BoxShade (https://embnet.vital-it.ch/software/BOX_form.html).

Quantification of Vms1 VLRF1 domain displacement. The spatial distance between α-carbon atoms of the same residues in the pre- and post-states of Vms1-VLRF1 models was measured and visualized using the PyMol Molecular Graphics Systems (v.1.8, Schrödinger) modevectors script[32].

Isolation of Vms1–60S complex for cryo-EM. *Vms1Δ* cells expressing Vms1(ΔVIM)–3C–3×Myc or Vms1(ΔVIM/Q295L)–3C–3×Myc from the *GPD1* promoter were grown to log phase in SCD medium at 30 °C. In brief, 300 OD_{600} units of yeast cells (one OD_{600} unit corresponds to the amount of yeast cells present in 1 ml of a culture with an optical density of 1 at 600 nm) were collected and divided into two 2-ml test tubes. Cells in each tube were washed once with ice-cold water and resuspended in 400 μl lysis buffer containing 20 mM HEPES-KOH pH 7.4, 100 mM KOAc, 10 mM $MgCl_2$, 0.5 mM DTT, 1 mM PMSF and cOmplete Protease Inhibitor Cocktail (Roche). Cells were lysed by agitation with glass beads followed by addition of 400 μl lysis buffer containing 1% Triton X-100. After incubation for 10 min on ice, insoluble material was removed by centrifugation at 17,000*g* for 10 min at 4 °C. Lysates (1.3 ml) were collected and incubated with Myc monoclonal antibody (Max Planck Institute of Biochemistry) and 22.5 μl of protein A sepharose CL-4B (GE Healthcare) for 2 h at 4 °C. After removal of supernatant, the immunoprecipitates were washed with 700 μl wash buffer (20 mM HEPES-KOH pH 7.4, 100 mM KOAc, 10 mM $MgCl_2$, 0.5 mM DTT) containing 0.5% Triton X-100. This washing step was repeated four times. The immunoprecipitates were then washed with 400 μl wash buffer. This washing step was repeated three times. Immunoprecipitates were incubated in 40 μl elution buffer containing 20 mM HEPES-KOH pH 7.4, 100 mM KOAc, 10 mM $MgCl_2$, 0.5 mM DTT, 0.1 mM Triton X-100 and 0.4 units of His-PreScission Protease (Max Planck Institute of Biochemistry) for 30 min at 4 °C to elute Vms1–ribosome complexes. The complex was crosslinked with 0.02% glutaraldehyde for 15 min on ice before preparation of the grids for cryo-EM analyses.

SDS–PAGE and immunoblotting. SDS–PAGE and immunoblotting were performed as described previously[13]. The Odyssey imaging system (LI-COR) and Image Studio Lite (LI-COR), ImageQuant LAS 4000 Mini (GE Healthcare) or Amersham Imager 600 (GE Healthcare) were used for signal detection.

Immunoprecipitation of Vms1–60S complex for biochemical analysis. Cells expressing C-terminally Myc tagged Vms1 or its mutant variants from the *GPD1* promoter were grown to log phase in SCD medium at 30 °C. Cells (100 OD_{600} units) were collected, washed once with ice-cold water and resuspended in 500 μl lysis buffer. Cells were lysed by agitation with glass beads followed by addition of 500 μl lysis buffer containing 1% Triton X-100. After incubation for 10 min on ice, insoluble material was removed by centrifugation at 17,000*g* for 10 min at 4 °C. Lysates (800 μl) were collected and incubated with Myc monoclonal antibody (Max Planck Institute of Biochemistry) and 15 μl of protein A sepharose CL-4B (GE healthcare) for 2 h at 4 °C. After removal of supernatant, the immunoprecipitates were washed with 700 μl of wash buffer containing 0.5% Triton X-100. This washing step was repeated four times. The immunoprecipitates were then washed once with 400 μl of wash buffer. Immunoprecipitates were eluted with 40 μl of SDS sample buffer and analysed by SDS–PAGE, Coomassie brilliant blue staining and immunoblotting.

Sucrose density gradient analysis. Sucrose density gradient analysis was performed as described previously[13]. The cells were grown in SCD medium at 30 °C. Proteins were precipitated with trichloroacetic acid, solubilized in urea sample buffer and analysed by SDS–PAGE and immunoblotting.

Electron microscopy and image processing. In brief, 2-nm pre-coated R3/3 holey carbon supported copper grids (Quantifoil) were glow discharged at 2×10^{-1} mbar for 20 s. Vms1(ΔVIM/Q295L) or Vms1(ΔVIM) pullout (3.5 μl) was directly applied onto each grid, blotted for 2–3 s at 4 °C and plunge-frozen in liquid ethane using a Vitrobot Mark IV (FEI Company). Grids were screened for

ice quality and cryo-EM data were acquired on a Titan Krios transmission electron microscope (FEI Company) at 300 kV under low-dose conditions (2.8 e^{-} Å^{-2} per frame) with a nominal pixel size of 1.084 Å per pixel on the object scale using the semi-automated software EM-TOOLS (TVIPS). Micrographs (9,845 and 7,875, respectively) of Vms1(ΔVIM/Q295L) and Vms1(ΔVIM) pullouts were collected on a Falcon II direct electron detector at nominal defocus ranges from −1.1 to −2.3 μm, respectively. Original image stacks of ten frames were aligned, summed and drift-corrected using MotionCor2[33]. Contrast-transfer-function (CTF) parameters and resolution were estimated for each micrograph using Gctf[34]. Micrographs with an estimated resolution better than 5 Å and astigmatism below 5% were manually inspected in real space for ice contamination or carbon rupture, which resulted in 9,642 and 7,361 micrographs for Vms1(ΔVIM/Q295L) and Vms1(ΔVIM) datasets, respectively. An initial particle picking was performed in a template-free manner on 1,000 micrographs of Vms1(ΔVIM) dataset by Gautomatch (http://www.mrc-lmb.cam.ac.uk/kzhang/) followed by a two-dimensional classification using RELION 2.1[35,36]. Class averages from ten various two-dimensional views were subsequently used as templates to pick particles from all inspected micrographs and resulted in 1,293,500 and 757,224 particles for Vms1(ΔVIM) and Vms1(ΔVIM/Q295L) datasets, respectively. These particles were then two-dimensional classified, three-dimensional refined and three-dimensional classified as shown in Extended Data Fig. 1 using RELION v.2.1[35,36].

Model building and refinement. The ribosomal large subunit 60S was built on the basis of the yeast cryo-EM structure (PDB 5GAK). The yeast Vms1 crystal structure containing the LRS–ZnF–VLRF1 domains (PDB 5WHG) was separated to LRS–VLRF1 and ZnF and docked into the corresponding densities. The Vms1 AnkR domain and Arb1 were modelled on the basis of homology structures using SWISS-MODEL[37]; a designed ankyrin repeat protein crystal structure (PDB 6F5E) was used for Vms1 AnkR, and *Pyrrococcus furiosus* RNase-L inhibitor (RLI) crystal structure (PDB 1YQT) and *E. coli* EttA cryo-EM structure (PDB 3J5S) were used for Arb1. Model building was conducted by using Coot[38]. The local resolutions of the RNase H-like fold (β-sheet flanked by helices) within the Vms1 VLRF1 domain and the Arb1 LD were around 4–4.5 Å. In these regions, the density enabled the modelling of side chains, in particular aromatic residues including the Vms1 Y285 and the Arb1 Y346. The Tif6 model (PDB 5T62) was directly docked into its corresponding density with UCSF Chimera[39].

The final models were real-space refined at resolutions of 3.4 Å, 3.6 Å and 3.4 Å for pre-state (Vms1(ΔVIM/Q295L)) without Arb1, pre-state with Arb1 and post-state (Vms1(ΔVIM)) maps, respectively, using PHENIX[40]. Final model evaluations were calculated by MolProbity[41]. Overfitting statistics were calculated by a random displacement of atoms in the model followed by a refinement against one of the half maps. Finally, Fourier shell correlation (FSC) curves are calculated between the volume of the refined model and both half maps using RELION.

Electron-microscopy figure preparation. Figures of electron-microscopy density maps and models were visualized and figures were created with UCSF ChimeraX[42]. Electron densities are displayed at multiple contour levels for optimal feature visualization of various components. Contour levels relative to the standard deviation (σ) of the corresponding full map values were calculated with UCSF Chimera[39]. For the pre-state map (Fig. 1a), the density of 60S is displayed at 2.1σ, and Vms1, Tif6 and tRNA are displayed at 1.33σ. For the post-state map (Fig. 1a), the density of both 60S and Tif6 is displayed at 1.69σ, Vms1 LRS–ZnF–VLRF1 is displayed at 0.76σ, and Vms1 AnkR–CC is displayed at 0.37σ. For the Rqc2 map (EMD-2812, Fig. 2e and Extended Data Fig. 3g), the map was first fitted into the grid of the pre-state map followed by Gaussian filtration with a width of 1.6. The density of P-tRNA$_{Rqc2}$ is displayed at 5.16σ, and Rqc2 and A-tRNA$_{Rqc2}$ are displayed at 3.45σ. For the pre-state map with Arb1 (Fig. 3a), the density of the 60S, Vms1 LRS-VLRF1 and tRNA is displayed at 1.85σ, Arb1 is displayed at 1.73σ, and Vms1 ZnF–AnkR–CC and Tif6 are displayed at 0.89σ. Information regarding contour levels for other extended data figures is described in the corresponding figure legends.

Statistics and reproducibility. Cryo-EM sample preparation and image data collection of Vms1(ΔVIM/Q295L) and Vms1(ΔVIM) pullouts shown in the paper were performed once ($n = 1$). Preparation of Vms1(ΔVIM/Q295L) and Vms1(ΔVIM) pullouts with or without fixing reagent all showed similar results. The quality check of the purified sample (Extended Data Fig. 1a) was performed once ($n = 1$), serving as a confirmation before the cryo-EM analysis. In addition, the absence of Cdc48 in Vms1(ΔVIM) was reported previously[13]. In vitro release assays in Fig. 2c, d represent two biologically independent repeats ($n = 2$); release assays in Fig. 3f and Extended Data Fig. 3l were both performed once ($n = 1$), as the results were similar in the different strains and they each covered two combinations of protein concentrations. In vivo assays in Figs. 2f, g, 3g–i and Extended Data Figs. 2g–j, 3h, m, n represent two biologically independent repeats ($n = 2$). The growth analysis of *vms1*Δ *arb1*::degron strain (Extended Data Fig. 3k, left) represents two biologically independent repeats ($n = 2$), and the Arb1 protein level (Extended Data Fig. 3k, right) was checked once ($n = 1$). For all experiments with $n > 1$, representative data from one experiment are shown in the paper. No statistical analysis has been applied throughout the work.

Reporting Summary. Further information on research design is available in the Nature Research Reporting Summary linked to this paper.

Data availability

The cryo-EM density maps of the pre-state with the absence and presence of Arb1 and the post-state have been deposited in the Electron Microscopy Data Bank under the accession codes EMD-4753, EMD-4751 and EMD-4752. The corresponding atomic models have been deposited in the Protein Data Bank under the accession codes 6R87, 6R84 and 6R86. For gel source images, see Supplementary Fig. 1.

25. Longtine, M. S. et al. Additional modules for versatile and economical PCR-based gene deletion and modification in *Saccharomyces cerevisiae*. *Yeast* **14**, 953–961 (1998).
26. Janke, C. et al. A versatile toolbox for PCR-based tagging of yeast genes: new fluorescent proteins, more markers and promoter substitution cassettes. *Yeast* **21**, 947–962 (2004).
27. Geertsma, E. R. & Dutzler, R. A versatile and efficient high-throughput cloning tool for structural biology. *Biochemistry* **50**, 3272–3278 (2011).
28. Geertsma, E. R. FX cloning: a simple and robust high-throughput cloning method for protein expression. *Methods Mol. Biol.* **1116**, 153–164 (2014).
29. Ikeuchi, K. et al. Collided ribosomes form a unique structural interface to induce Hel2-driven quality control pathways. *EMBO J.* **38**, e100276 (2019).
30. Notredame, C., Higgins, D. G. & Heringa, J. T-Coffee: a novel method for fast and accurate multiple sequence alignment. *J. Mol. Biol.* **302**, 205–217 (2000).
31. Taly, J. F. et al. Using the T-Coffee package to build multiple sequence alignments of protein, RNA, DNA sequences and 3D structures. *Nat. Protoc.* **6**, 1669–1682 (2011).
32. The PyMOL Molecular Graphics System v.1.8 (Schrodinger, 2015).
33. Zheng, S. Q. et al. MotionCor2: anisotropic correction of beam-induced motion for improved cryo-electron microscopy. *Nat. Methods* **14**, 331–332 (2017).
34. Zhang, K. Gctf: real-time CTF determination and correction. *J. Struct. Biol.* **193**, 1–12 (2016).
35. Scheres, S. H. RELION: implementation of a Bayesian approach to cryo-EM structure determination. *J. Struct. Biol.* **180**, 519–530 (2012).
36. Kimanius, D., Forsberg, B. O., Scheres, S. H. & Lindahl, E. Accelerated cryo-EM structure determination with parallelisation using GPUs in RELION-2. *eLife* **5**, e18722 (2016).
37. Biasini, M. et al. SWISS-MODEL: modelling protein tertiary and quaternary structure using evolutionary information. *Nucleic Acids Res.* **42**, W252–W258 (2014).
38. Emsley, P. & Cowtan, K. Coot: model-building tools for molecular graphics. *Acta Crystallogr. D* **60**, 2126–2132 (2004).
39. Pettersen, E. F. et al. UCSF Chimera–a visualization system for exploratory research and analysis. *J. Comput. Chem.* **25**, 1605–1612 (2004).
40. Adams, P. D. et al. PHENIX: a comprehensive Python-based system for macromolecular structure solution. *Acta Crystallogr. D* **66**, 213–221 (2010).
41. Chen, V. B. et al. MolProbity: all-atom structure validation for macromolecular crystallography. *Acta Crystallogr. D* **66**, 12–21 (2010).
42. Goddard, T. D. et al. UCSF ChimeraX: Meeting modern challenges in visualization and analysis. *Protein Sci.* **27**, 14–25 (2018).

Acknowledgements W.N. acknowledges funding from the Deutsche Forschungsgemeinschaft (NE 101/28-1) and from the Carl Friedrich von Siemens Foundation and thanks M. Kiebler for providing laboratory space and facilities. The authors thank S. Rieder and C. Ungewickel for technical assistance and M. Esaki for the Rip1 antibody. This research was supported by a grant from the Deutsche Forschungsgemeinschaft (GRK1721 to R.B.) and by Grants-in-Aid for Scientific Research (KAKENHI) from the Japan Society for the Promotion of Science (grant numbers 26116003 to T. Inada and 19K16052 to T. Izawa). T.S. is supported by a DFG fellowship through the Graduate School of Quantitative Biosciences Munich (QBM).

Author contributions T.S., T. Izawa, M.T., Y.Y., F.U.H., T. Inada, W.N. and R.B. designed the study and T.S., T. Izawa, M.T., W.N. and R.B. wrote the manuscript. T. Izawa purified Vms1–60S complexes. T.S., T. Izawa and M.T. performed genetic and biochemical experiments. T.S., T. Izawa and Y.Y. prepared the cryo-EM samples and O.B. collected cryo-EM data. T.S. processed the cryo-EM data with contribution from Y.Y., and together with J.C. built the models and analysed the structures. All authors interpreted the data and contributed to the final manuscript.

Competing interests The authors declare no competing interests.

Additional information

Supplementary information. is available for this paper at https://doi.org/10.1038/s41586-019-1307-z.

Correspondence and requests for materials should be addressed to W.N. or R.B.

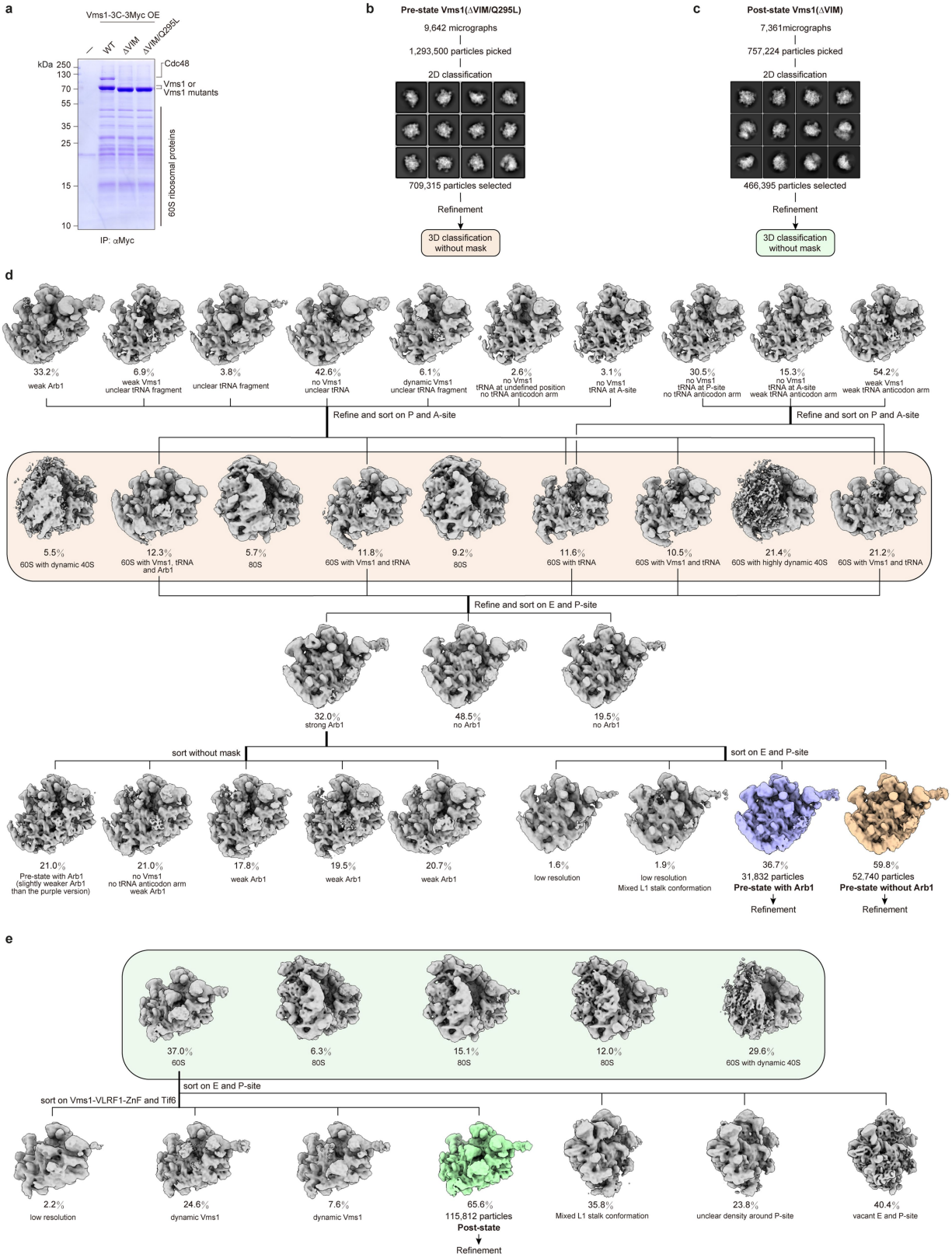

Extended Data Fig. 1 | Sample preparation and cryo-EM analysis of Vms1–60S ribosomal subunit particles. a, Vms1 and Vms1 mutants were immunoprecipitated from the lysates of *vms1*Δ cells expressing Vms1–3C–3×Myc or indicated Vms1 mutants from the *GPD1* promoter. The precipitates were eluted by 3C cleavage and analysed by SDS–PAGE and Coomassie brilliant blue staining. **b**, Two-dimensional classification of Vms1(ΔVIM/Q295L)–60S particles (pre-state). **c**, Two-dimensional classification of Vms1(ΔVIM)–60S particles (post-state). **d**, Three-dimensional classification of Vms1(ΔVIM/Q295L)–60S ribosome particles (pre-state). Reconstruction in blue and yellow mark final maps. **e**, Three-dimensional classification of Vms1(ΔVIM)–60S particles (post-state). Reconstruction in green marks final map.

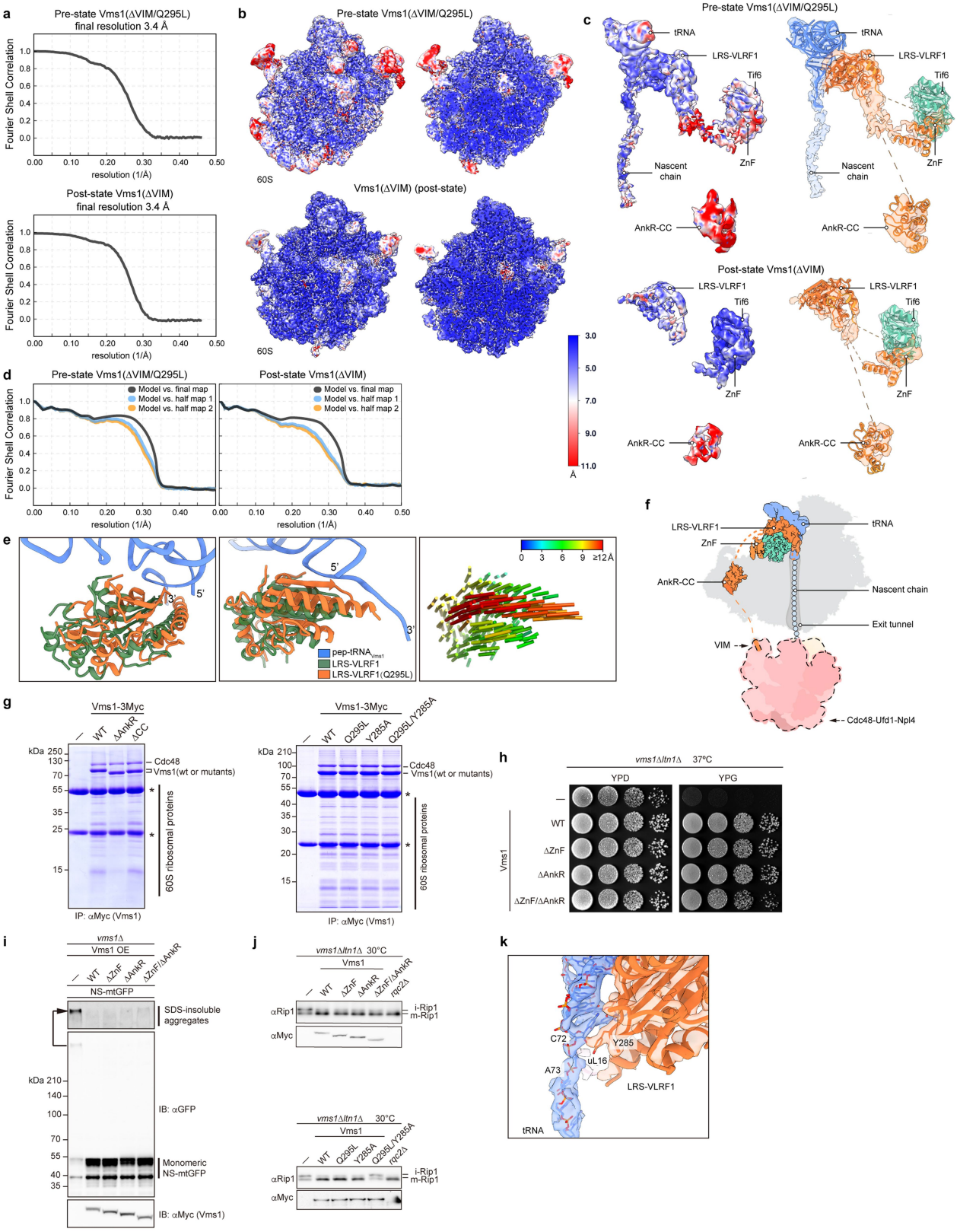

Extended Data Fig. 2 | See next page for caption.

Extended Data Fig. 2 | Resolution of Vms1 domains and their roles in ribosome binding, rescuing growth and preventing mitochondrial toxicity. a, Final resolution of Vms1 pre-state and post-state 60S ribosome particles. **b**, Local resolution of Vms1 pre-state and post-state. Left, overviews; right, transverse views. The electron density for the pre-state is displayed at 1.68σ and for the post-state at 1.83σ. **c**, Tri-model position of Vms1 and its interaction with peptidyl-tRNA (pre-state, top; density of Vms1 LRS–VLRF1 and tRNA is displayed at 3.23σ, Vms1 AnkR–CC at 2.20σ, nascent chain at 2.10σ, and Vms1 ZnF and Tif6 at 1.29σ) and interaction with Tif6 (post-state, bottom; density of Vms1 LRS–ZnF–VLRF1 and Tif6 is displayed at 2.15σ, and Vms1 AnkR–CC at 0.75σ). Left, local resolution; right, density with docked models. **d**, Fit of models to maps. FSC curves calculated between the refined model and the final map (black), with the self- and cross-validated correlations in blue and orange, respectively. **e**, Comparison between pre- and post-state of VLRF1 in two views (left and middle). Atom-to-atom quantification of the VLRF1 state difference (right). **f**, Prospective transverse model for interaction of the Vms1 VIM domain and Cdc48 on the 60S ribosomal subunit. **g**, Vms1 and Vms1 mutants were immunoprecipitated from the lysates of *vms1*Δ cells expressing Vms1–3×Myc or indicated Vms1 mutants from the *GPD1* promoter. The precipitates were analysed by SDS–PAGE and Coomassie brilliant blue staining. Asterisks indicate IgG heavy and light chains. **h**, Rescue of growth of *vms1*Δ*ltn1*Δ cells by expression of Vms1, Vms1(ΔZnF), Vms1(ΔAnkR) or Vms1(ΔZnF/ΔAnkR) from the *VMS1* promoter. Cells were grown at 37 °C on YPD or YPG plates. **i**, Prevention of aggregation of the NS-mtGFP reporter in *vms1*Δ cells by overexpression of Vms1–3×Myc or indicated Vms1 mutants from the *GPD1* promoter. The cell extracts were analysed by immunoblotting with the indicated antibodies. **j**, Analysis of the mitochondrial indicator protein Rip1 in *vms1*Δ*ltn1*Δ cells by expression of Vms1–3×Myc or the indicated Vms1 mutants from the *VMS1* promoter. The cells were grown at 30 °C. Cell lysates were analysed by immunoblotting using Rip1 and Myc antibodies. **k**, Density and molecular models of Vms1, $tRNA_{Vms1}$, and uL16 loop in the pre-state. The density of uL16 is displayed at 4.06σ, tRNA at 3.76σ and Vms1 at 3.57σ. See Supplementary Fig. 1 for gel source images.

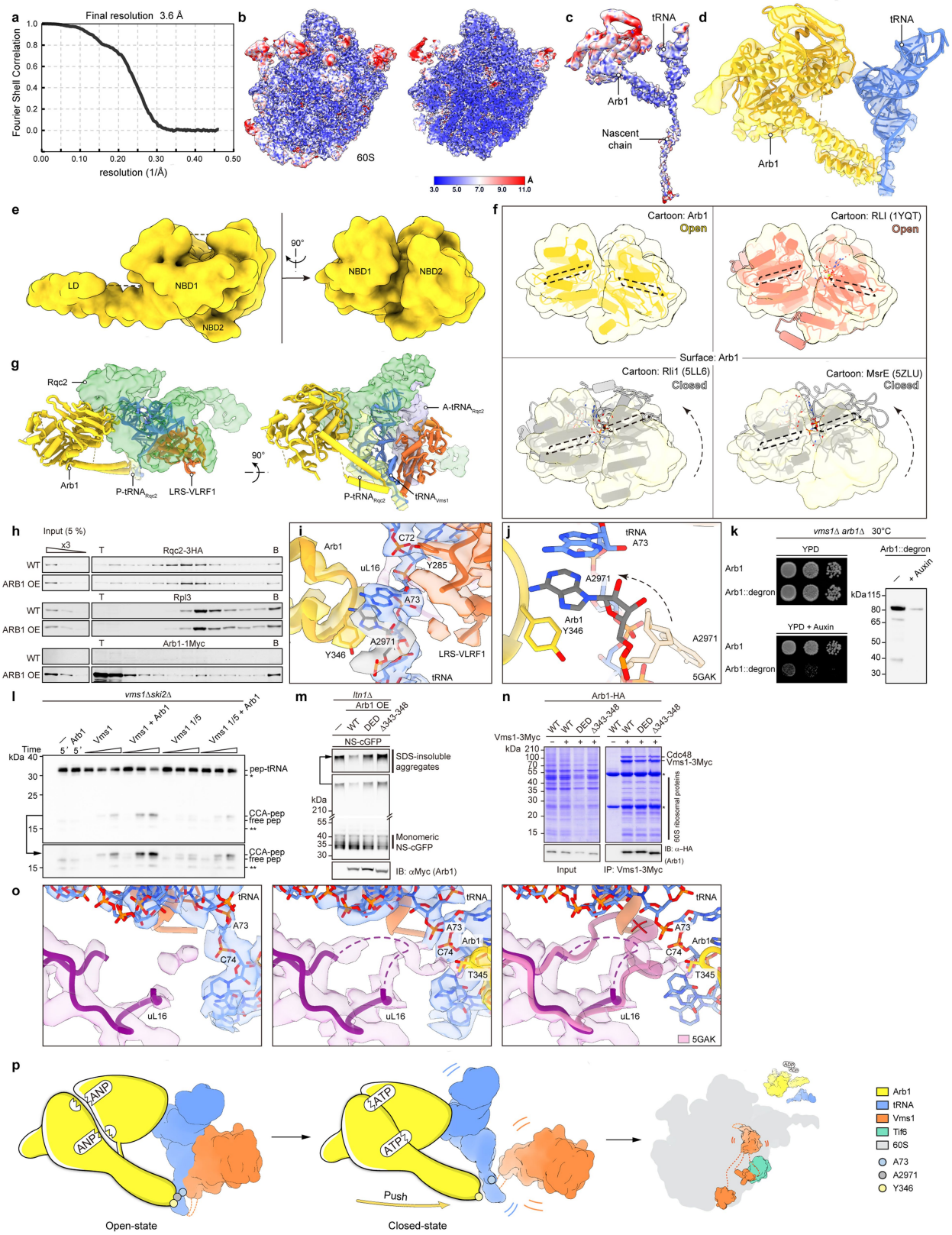

Extended Data Fig. 3 | See next page for caption.

Extended Data Fig. 3 | Interaction of Arb1 with Vms1–60S ribosomal subunit complex. a, Final resolution of the Vms1(ΔVIM/Q295L) pre-state in the presence of Arb1. **b**, Local resolution map of the pre-state in the presence of Arb1. Left, overview; right, transverse view. The electron density is displayed at 2.21σ. **c**, Local resolution map of Arb1 with peptidyl-tRNA. **d**, Density and docked models of Arb1 and tRNA in yellow and blue, respectively. The tRNA density in **c**, **d** is displayed at 3.59σ and the rest remains at 2.21σ. **e**, View of the Arb1 model surface in two orientations. The nucleotide binding domains (NBD1 and 2) and the LD are indicated. **f**, Comparison of Arb1 with ABCF-type ATPases in open and closed states. The models of the ADP-bound RLI from *P. furiosus* (PDB 1YQT), the AMP-PNP bound Rli1 from *S. cerevisiae* (PDB 5LL6) and the AMP-PNP bound MsrE from *Pseudomonas aeruginosa* (PDB 5ZLU) were compared to Arb1 by rigid-body fitting of NBD1 into the density of the Arb1 NBD1. **g**, Steric clash of Arb1–$tRNA_{Vms1}$ with Rqc2–P-$tRNA_{Rqc2}$ on the 60S subunit. Arb1, $tRNA_{Vms1}$ and Vms1 LRS–VLRF1 domain are shown as models and Rqc2, A-$tRNA_{Rqc2}$ and P-$tRNA_{Rqc2}$ as densities. See Methods for the contour levels. **h**, Overexpression of Arb1–Myc does not lead to displacement of Rqc2 on 60S subunits. Lysates of cells expressing Rqc2–3HA from its endogenous promoter with or without overexpression of Arb1–1×Myc were analysed by sucrose-gradient centrifugation. Fractions were analysed by SDS–PAGE and immunoblotting using HA and Myc antibodies. 60S and 80S ribosomes were detected using anti-Rpl3 antibody. T, top and B, bottom of the gradient. **i**, Density and molecular model of Vms1, $tRNA_{Vms1}$, uL16 and Arb1 of the Vms1–60S pre-state in the presence of Arb1. The density of 25S A2971 is displayed at 5.07σ, Arb1 at 4.55σ, Vms1 at 4.34σ, tRNA at 3.87σ and uL16 at 3.76σ. **j**, Model illustrating the rotation of 25S A2971 (A2602 in *E. coli*) by 180° upon Arb1 binding. **k**, The *vms1*Δ *arb1*Δ shuffle strain was complemented either with an Arb1(WT) construct or an Arb1-sAid-HA degron plasmid (Arb1::degron). Growth on YPD and YPD + auxin (500 μM final concentration) plates was monitored after two days at 30 °C (left). Arb1 protein level of the *vms1*Δ *arb1*::degron strain before and after treatment with auxin (500 μM final concentration) for 60 min at 30 °C (right). Cell lysates were analysed by immunoblotting using the HA antibody. **l**, Yeast in vitro release reaction of arrested peptides translated from the NS-3×Flag RQC reporter mRNA in *vms1*Δ*ski2*Δ lysate. Buffer (−), Arb1, Vms1 or Vms1 together with Arb1 were added to cycloheximide-stopped translation reactions. Incubation time: 5 min (lane 1 and 2) at 25 °C; 0, 2 or 5 min, respectively (lanes 3–12). Molar ratios of Vms1 and Arb1 are 1 to 25 (Vms1 + Arb1) and 1 to 50 (Vms1 1/5 + Arb1), respectively. Bottom, longer exposure of the relatively weak bands. CCA, CCA from tRNA 3′ end; pep: peptidyl or peptide; * and ** indicate peptidyl-tRNA and free peptide from the colliding ribosome, respectively. **m**, Overexpression of Arb1 suppresses aggregation of a NS-cGFP reporter construct. Cell extracts of *ltn1*Δ cells expressing NS-cGFP and overexpressing Myc-tagged Arb1 or indicated Arb1 mutants were analysed by immunoblotting using anti-GFP and anti-Myc antibodies. **n**, Cell lysates of *vms1*Δ*arb1*Δ cells expressing Arb1–HA or indicated Arb1 mutants without or with expression of Vms1–3×Myc were analysed by immunoprecipitation using Myc antibody. The inputs and the immunoprecipitates were analysed by Coomassie brilliant blue staining and immunoblotting using HA antibody. Asterisks indicate IgG heavy and light chains. **o**, Densities and molecular models of Vms1, $tRNA_{Vms1}$ and uL16 loop in the two pre-states either without Arb1 (left) or with Arb1 (middle). Right, the superposition of the uL16 loop in the Arb1 containing pre-state and in the eIF5A-bound 60S ribosomal subunit (PDB 5GAK) in purple and pink, respectively. The density of uL16 left structure is displayed at 4.06σ; the rest remains the same as in **i**. **p**, Model of tRNA positioning and dislocation by Arb1. See Supplementary Fig. 1 for gel source images.

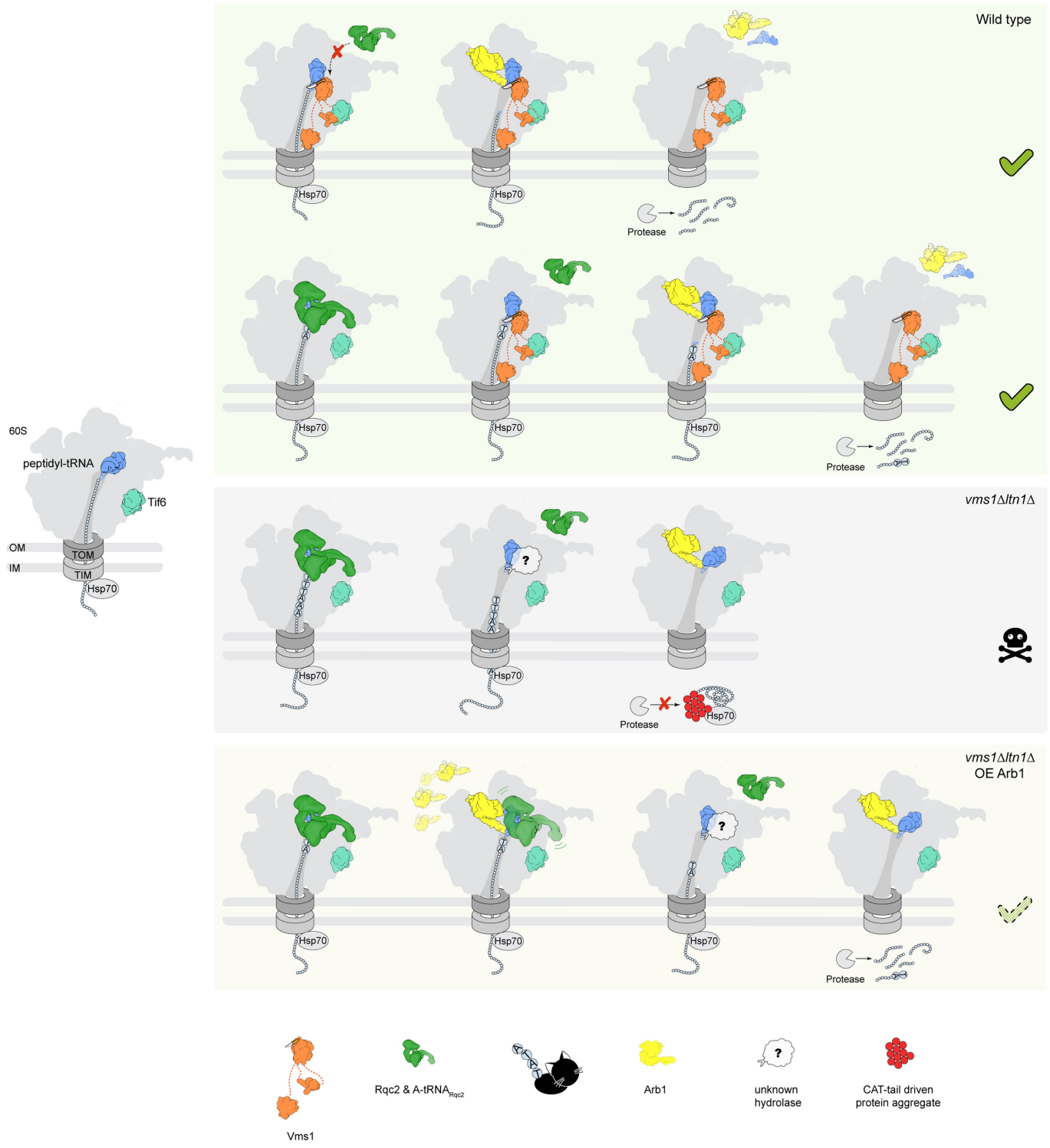

Extended Data Fig. 4 | Schematic model of the structural roles of Vms1 and Arb1 in counteracting CAT-tailing of toxic faulty mitochondrial proteins by Rqc2 and promoting their release into the mitochondria. Top two rows: in wild-type cells, 60S subunits accumulate in close proximity to the protein import complex (TOM) of the outer membrane because import can occur co-translationally, especially when translation is stalled. Vms1 and Arb1 interfere sterically with binding of Rqc2 on the 60S subunits and thereby with CAT-tailing, accelerating peptidyl-tRNA release. The released polypeptides are imported into the mitochondria and degraded by the intramitochondrial chaperone and protease system. Middle row: in the absence of Vms1 and Ltn1, CAT-tailed mitochondrial proteins are released into the mitochondria where they aggregate with pre-existing proteins, leading to breakdown of mitochondrial functions in oxidative phosphorylation and other essential processes such as mitochondrial protein synthesis. Bottom row: overexpression of Arb1 can partially compensate for deficiency of Vms1 and Ltn1 by impairing Rqc2 dependent CAT-tailing and promoting peptidyl-tRNA release.

Extended Data Table 1 | Cryo-EM data collection, refinement and validation statistics

	#1 Pre-state (without Arb1) (EMDB-4753) (PDB 6R87)	#2 Pre-state (with Arb1) (EMDB-4751) (PDB 6R84)	#3 Post-state (EMDB-4752) (PDB 6R86)
Data collection and processing			
Magnification	129,151	129,151	129,151
Voltage (kV)	300	300	300
Electron exposure ($e^-/Å^2$)	28	28	28
Defocus range (μm)	-1.1 to -2.3	-1.1 to -2.3	-1.1 to -2.3
Pixel size (Å)	1.084	1.084	1.084
Symmetry imposed	C1	C1	C1
Initial particle images (no.)	1,293,500	1,293,500	757,224
Final particle images (no.)	52,740	31,822	115,812
Map resolution (Å)	3.4	3.6	3.4
FSC threshold	0.143	0.143	0.143
Refinement			
Initial model used (PDB code)	5GAK	5GAK	5GAK
Model resolution (Å)	3.1	3.1	3.1
FSC threshold	0.5	0.5	0.5
Map sharpening *B* factor ($Å^2$)	-70	-50	-100
Model composition			
Non-hydrogen atoms	135,256	138,805	132,447
Protein residues	7,237	7,688	7,238
Ligands	1	1	1
B factors ($Å^2$)			
Protein	104.65	72.81	69.00
Ligand	265.70	147.46	156.11
R.m.s. deviations			
Bond lengths (Å)	0.0125	0.009	0.0071
Bond angles (°)	1.34	1.106	1.14
Validation			
MolProbity score	1.91	1.82	1.71
Clashscore	7.42	5.81	4.61
Poor rotamers (%)	0.66	0.51	0.39
Ramachandran plot			
Favored (%)	91.45	91.44	92.22
Allowed (%)	8.23	8.20	7.42
Disallowed (%)	0.32	0.36	0.37

Summary of relevant parameters used during cryo-EM data collection and processing. Refinement and validation statistics are provided for the molecular models of the Vms1–60S particles in pre-state and post-state as well as for the Arb1-containing pre-state particle.

Extended Data Table 2 | *S. cerevisiae* strains used in this study

Name	Relevant genotype	Source
vms1Δ	*vms1*::kanMX4	Izawa *et al*., 2017
ltn1Δ	*ltn1*::kanMX4	Izawa *et al*., 2017
vms1Δltn1Δ	*vms1*::HIS3MX6 *ltn1*::kanMX4	Izawa *et al*., 2017
vms1Δltn1Δrqc2Δ	*vms1*::His3MX6 *ltn1*::kanMX4 *rqc2*::*LEU2*	Izawa *et al*., 2017
RQC2-3HA	*RQC2*-3xHA::HIS3MX6	Izawa *et al*., 2017
vms1Δarb1Δ	*vms1*::kanMX4 *arb1*::*LEU2*	This study
vms1Δarb1Δ shuffle	*vms1*::kanMX4 *arb1*::natNT2, pRS316-*ARB1*	This study
vms1Δski2Δ	*vms1*::kanMX4 *ski2*::*LEU2*	This study

Extended Data Table 3 | *S. cerevisiae* plasmids used in this study

Name	Relevant information	Source
p416GPD-*VMS1*-3C-3xMyc	CEN, *URA3*, P*GPD*	This study
p416GPD-*VMS1* ΔVIM-3C-3xMyc	CEN, *URA3*, P*GPD*, (Δ613- 632)	This study
p416GPD-*VMS1* Q295L ΔVIM-3C-3xMyc	CEN, *URA3*, P*GPD*, (Δ613- 632)	This study
pRS415-*VMS1*-3xMyc	CEN, *LEU2*, P*VMS1*	Izawa *et al.*, 2017
pRS415-*VMS1* Q295L-3xMyc	CEN, *LEU2*, P*VMS1*	This study
pRS415-*VMS1* Y285A-3xMyc	CEN, *LEU2*, P*VMS1*	This study
pRS415-*VMS1* Q295L Y285A-3xMyc	CEN, *LEU2*, P*VMS1*	This study
p415GPD-*VMS1*-3xMyc	CEN, *LEU2*, P*GPD*	Izawa *et al.*, 2017
p415GPD-*VMS1* Q295L-3xMyc	CEN, *LEU2*, P*GPD*	This study
p415GPD-*VMS1* Y285A-3xMyc	CEN, *LEU2*, P*GPD*	This study
p415GPD-*VMS1* Q295L Y285A-3xMyc	CEN, *LEU2*, P*GPD*	This study
pRS415-*VMS1* ΔZnF-3xMyc	CEN, *LEU2*, P*VMS1*, (Δ74-116)	This study
pRS415-*VMS1* ΔAnkR-3xMyc	CEN, *LEU2*, P*VMS1*, (Δ446-511)	This study
pRS415-*VMS1* ΔZnF ΔAnkR-3xMyc	CEN, *LEU2*, P*VMS1*, (Δ74-116, Δ446-511)	This study
p415GPD-*VMS1* ΔZnF-3xMyc	CEN, *LEU2*, P*GPD*, (Δ74-116)	This study
p415GPD-*VMS1* ΔAnkR-3xMyc	CEN, *LEU2*, P*GPD*, (Δ446-511)	This study
p415GPD-*VMS1* ΔZnF ΔAnkR-3xMyc	CEN, *LEU2*, P*GPD*, (Δ74-116, Δ446-511)	This study
p415GPD-*VMS1* ΔCC-3xMyc	CEN, *LEU2*, P*GPD*, (Δ544-583)	This study
p415GPD-*ARB1*-1xMyc	CEN, *LEU2*, P*GPD*	This study
p415GPD-*ARB1* G229D G230E G519D-1xMyc	CEN, *LEU2*, P*GPD*	This study
p415GPD-*ARB1* (Δ343-348)-1xMyc	CEN, *LEU2*, P*GPD*	This study
p415GPD-*ARB1* Y346A-1xMyc	CEN, *LEU2*, P*GPD*	This study
pRS313-*ARB1*-1xHA	CEN, *HIS3*, P*ARB1*, T*ARB1*	This study
pRS313-*ARB1* G229D G230E G519D -1xHA	CEN, *HIS3*, P*ARB1*, T*ARB1*	This study
pRS313-*ARB1* (Δ343-348)-1xHA	CEN, *HIS3*, P*ARB1*, T*ARB1*	This study
p416GPD-NS-mtGFP-3xHA	CEN, *URA3*, P*GPD*	Izawa *et al.*, 2017
p416GAL1-NS-cGFP	CEN, *URA3*, P*GAL1*	Izawa *et al.*, 2017
pRS316-*ARB1*	CEN, *URA3*, P*ARB1*, T*ADH1*	This study
YCplac111-*ARB1*	CEN, *Leu2*, P*ARB1*, T*ADH1*	This study
YCplac111-OsTIR1-3xMyc-*ARB1*-sAid-1xHA	CEN, *Leu2*, P*ADH1*-OsTIR1-3xMyc, P*ARB1*-*ARB1*-sAid-1xHA	This study

nature research

Corresponding author(s): Walter Neupert and Roland Beckmann

Reporting Summary

Nature Research wishes to improve the reproducibility of the work that we publish. This form provides structure for consistency and transparency in reporting. For further information on Nature Research policies, see Authors & Referees and the Editorial Policy Checklist.

Statistical parameters

When statistical analyses are reported, confirm that the following items are present in the relevant location (e.g. figure legend, table legend, main text, or Methods section).

n/a	Confirmed	
☐	☒	The exact sample size (*n*) for each experimental group/condition, given as a discrete number and unit of measurement
☐	☒	An indication of whether measurements were taken from distinct samples or whether the same sample was measured repeatedly
☒	☐	The statistical test(s) used AND whether they are one- or two-sided *Only common tests should be described solely by name; describe more complex techniques in the Methods section.*
☒	☐	A description of all covariates tested
☒	☐	A description of any assumptions or corrections, such as tests of normality and adjustment for multiple comparisons
☒	☐	A full description of the statistics including central tendency (e.g. means) or other basic estimates (e.g. regression coefficient) AND variation (e.g. standard deviation) or associated estimates of uncertainty (e.g. confidence intervals)
☒	☐	For null hypothesis testing, the test statistic (e.g. *F*, *t*, *r*) with confidence intervals, effect sizes, degrees of freedom and *P* value noted *Give P values as exact values whenever suitable.*
☒	☐	For Bayesian analysis, information on the choice of priors and Markov chain Monte Carlo settings
☒	☐	For hierarchical and complex designs, identification of the appropriate level for tests and full reporting of outcomes
☒	☐	Estimates of effect sizes (e.g. Cohen's *d*, Pearson's *r*), indicating how they were calculated
☒	☐	Clearly defined error bars *State explicitly what error bars represent (e.g. SD, SE, CI)*

Our web collection on statistics for biologists may be useful.

Software and code

Policy information about availability of computer code

Data collection	semi-automated software EM-TOOLS (TVIPS)
Data analysis	MotionCor2, Gctf v1.06, Relion 2.1-beta-1, Gautomatch v0.56, PSIPRED v3.3, SWISS-MODEL, CCP4 v7.0, Phenix 1.13 (including MolProbity) and Phenix 1.15 (used for calculating the B factors), Chimera 1.12, ChimeraX v0.7, Coot 0.8.8, MacPyMOL 1.3.

For manuscripts utilizing custom algorithms or software that are central to the research but not yet described in published literature, software must be made available to editors/reviewers upon request. We strongly encourage code deposition in a community repository (e.g. GitHub). See the Nature Research guidelines for submitting code & software for further information.

Data

Policy information about availability of data

All manuscripts must include a data availability statement. This statement should provide the following information, where applicable:

- Accession codes, unique identifiers, or web links for publicly available datasets
- A list of figures that have associated raw data
- A description of any restrictions on data availability

The three reported cryo-EM density maps have been deposited in the EM Data Bank under the accession codes EMD-4753, EMD-4751 and EMD-4752. The corresponding atomic models have been deposited in the Protein Data Bank under the accession codes 6R87, 6R84 and 6R86.

Field-specific reporting

Please select the best fit for your research. If you are not sure, read the appropriate sections before making your selection.

☒ Life sciences ☐ Behavioural & social sciences ☐ Ecological, evolutionary & environmental sciences

For a reference copy of the document with all sections, see nature.com/authors/policies/ReportingSummary-flat.pdf

Life sciences study design

All studies must disclose on these points even when the disclosure is negative.

Sample size	No statistical methods were applied to pre-determine sample sizes. Single particle analyses averaged 31,832, 52,740 and 115,812 particles for the reported three reconstructions and all reached overall high resolution (3.4 - 3.6 Å).
Data exclusions	No biochemical data were excluded from the analysis.
Replication	Critical biochemical experiments were successfully and reliably reproduced. Cryo-EM sample preparation and image data collection of Vms1 Q295L ΔVIM and Vms1 ΔVIM pullouts reported in the paper were performed once (n = 1). More than two grids were used for each data collection. Moreover, preparation of Vms1 Q295L and Vms1 ΔVIM pullouts with or without fixing reagent had similar results. The quality check of the purified sample (Extended Data Figure 1a) was performed once (n = 1) serving as a confirmation before the cryo-EM analysis. In addition, the absence of Cdc48 in Vms1 ΔVIM was reported previously (Izawa et al., 2017). In vitro release assays in Figure 2c-d were biologically repeated twice (n = 2); release assays in Figure 3f and Extended Data Figure 3l were both performed once (n = 1) as the results were similar in the different strains and each of them covered two combinations of protein concentrations. In vivo assays in Figure 2f-g, Figure 3g-i, Extended Data Figure 2g-j and Extended Data Figure 3h, 3m-n were all biologically repeated twice (n = 2). The growth analysis of vms1Δ arb1::degron strain (Extended Data Figure 3k, left) was biologically repeated twice (n = 2), and the Arb1 protein level (Extended Data Figure 3k, right) was checked once (n = 1). Representative data from one experiment are shown in the paper.
Randomization	No randomization was required for the reported experiments as no allocation into experimental groups were needed. For single particle analyses, particles were divided into two random seeds for reconstruction in order to calculate the resoluion via fourier shell correlation. Each final maps are joined reconstructions.
Blinding	Blinding to group allocation was not required for the reported experiments as no allocation into experimental groups were needed.

Reporting for specific materials, systems and methods

Materials & experimental systems

n/a	Involved in the study
☒	☐ Unique biological materials
☐	☒ Antibodies
☒	☐ Eukaryotic cell lines
☒	☐ Palaeontology
☒	☐ Animals and other organisms
☒	☐ Human research participants

Methods

n/a	Involved in the study
☒	☐ ChIP-seq
☒	☐ Flow cytometry
☒	☐ MRI-based neuroimaging

Antibodies

Antibodies used

Mouse monoclonal anti-Myc antibodies
Source:
1) Izawa et al. 2017 (home made)
2) Santa Cruz Biochemistry (Cat.# sc-40; Lot# K2707)

Mouse monoclonal anti-HA antibody
Source: Santa Cruz Biochemistry (Cat.# sc-7392; Lot# 10616)

Rabbit polyclonal anti-HA antibody
Source: Santa Cruz Biochemistry (Cat.# -805; Lot# A0807)

Mouse monoclonal anti-GFP antibody
Source: Roche (Cat.# 11814460001; Lot# 36405300)

Mouse monoclonal anti-FLAG M2-Peroxidase (HRP) antibody
Source: Sigma-Aldrich (Cat.# A8592)

Rabbit polyclonal anti-Rip1 antibodies
Source:
1) Izawa et al. 2017 (home made)
2) Sawamura et al. 2014 DOI:10.1016/j.bbrc.2013.12.084 (a gift from Masatoshi Esaki)

Mouse monoclonal anti-Rpl3 antibody
Source: Developmental Studies Hybridoma Bank

Validation

All the employed commercial antibodies were verified by their manufacturers, including the specie specificity, noisy signaling, and applications. The data of validations are available on the manufacturers' website with the indicated Cat #. Home-made antibodies were validated and used in the indicated published papers.

Figure 2c

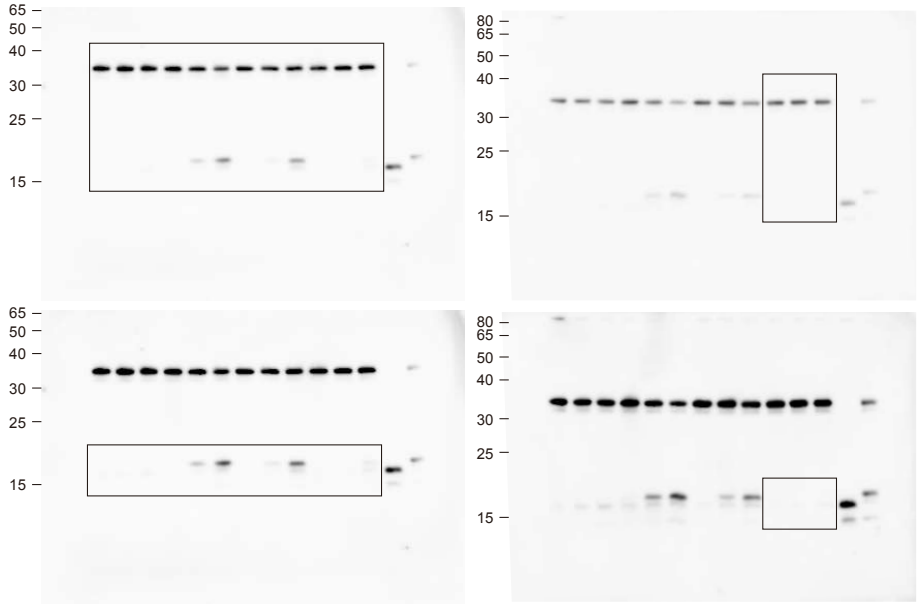

Figure 2d

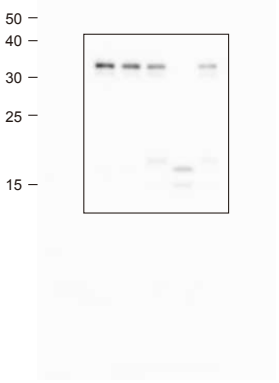

Figure 2g

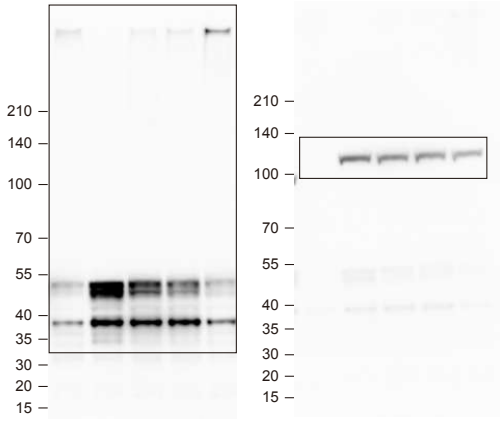

Figure 3f

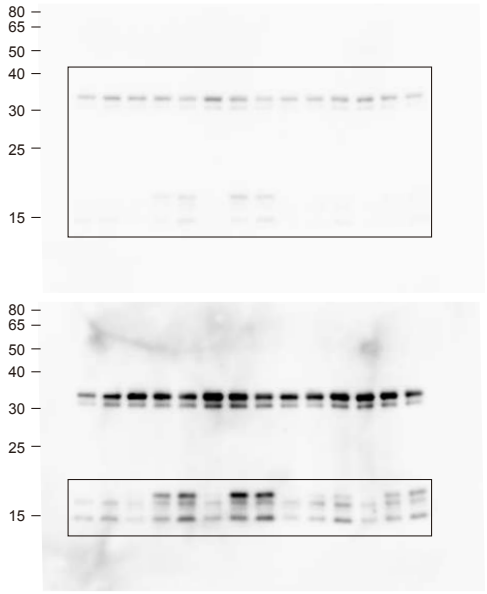

Figure 3h

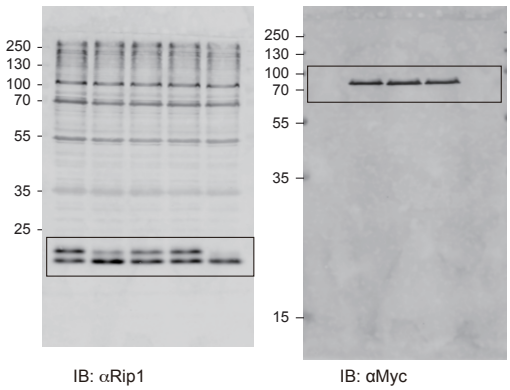

Figure 3i

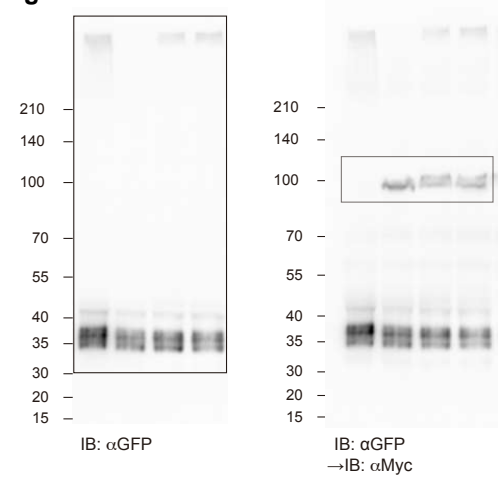

Extended Figure 2i

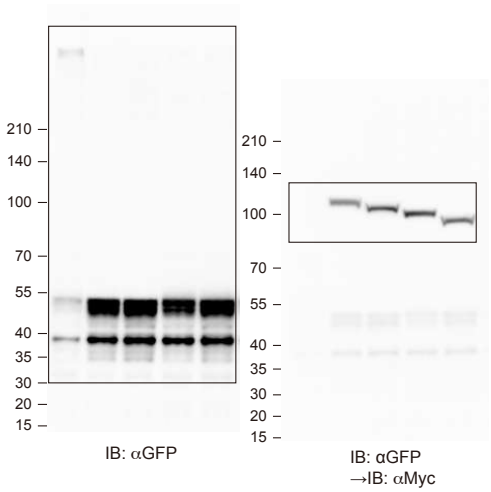

Extended Figure 2j Top panel

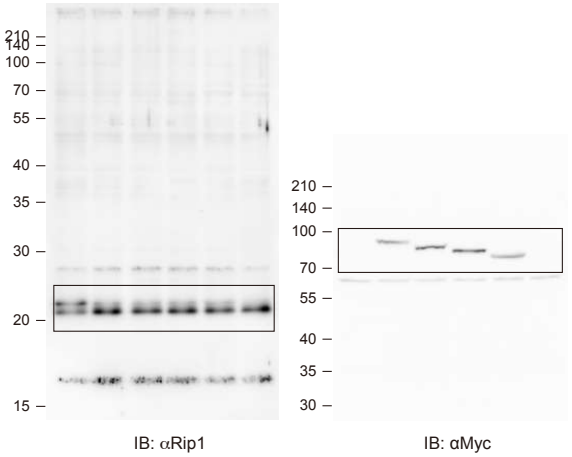

Extended Figure 2j Bottom panel

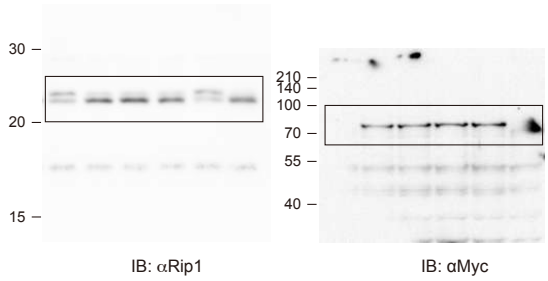

Extended Figure 3h (For Rqc2-3HA)

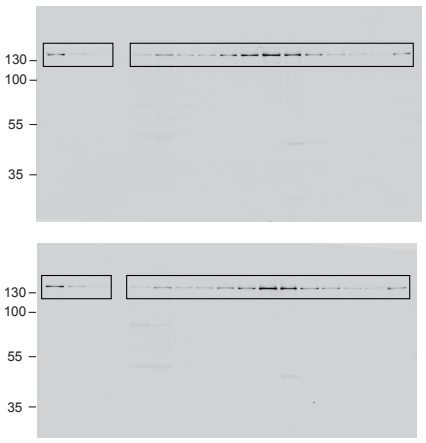

IB: αHA

Extended Figure 3h (For Rpl3)

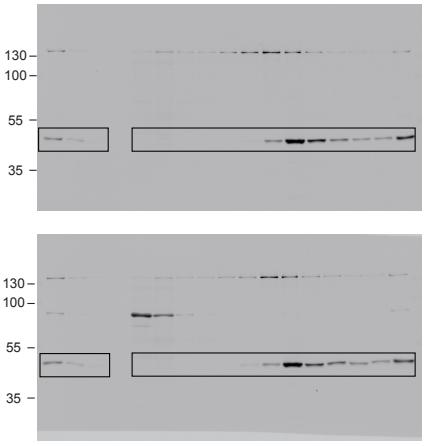

IB: αHA
→IB: αMyc, αRpl3

Extended Figure 3h (For Arb1-Myc)

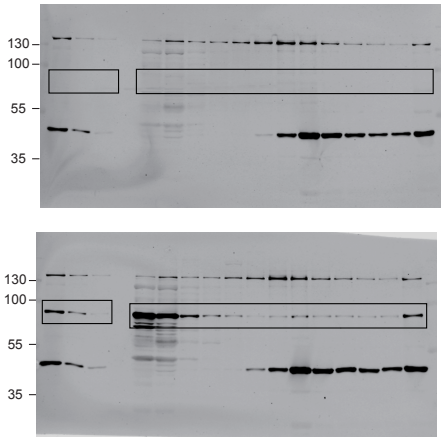

IB: αHA
→IB: αMyc, αRpl3

Extended Figure 3k

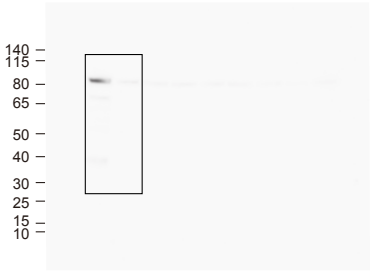

Extended Figure 3l

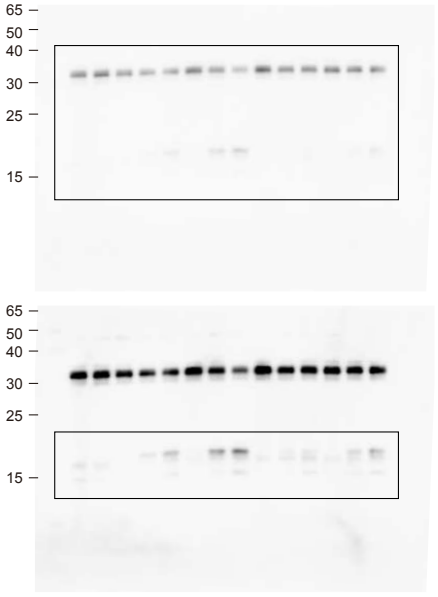

Extended Figure 3m

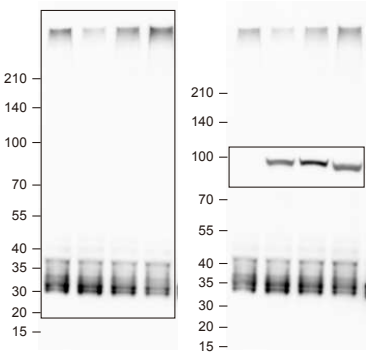

IB: αGFP

IB: αGFP
→IB: αMyc

Extended Figure 3n

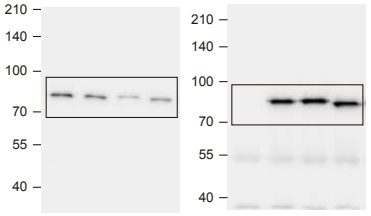

IB: αHA

IB: αHA

Chapter 3

Discussion and Outlook

3.0.1 VemP, a fresh tip of the iceberg

The ribosomal tunnel provides an approximately 100-Å long environment for newly synthesized polypeptide chains to pass through. This ribosomal interior provides a direct ground for specific nascent chains like RAPs to modulate the translation rate, resulting in immediate and significant downstream consequences for co-translational protein targeting and folding.

The discovery of the force-sensing VemP has widened the scope of the stalling modes. The 2.9-Å structure of VemP-mediated ribosome stalling revealed a novel strategy of arresting a ribosome. When stalled in the ribosome tunnel, it forms an extensive secondary structure which further extends towards the PTC and disrupts its catalytic function by steric hindrance. This finding explains why VemP possesses the longest known arrest stretch to date.

VemP is an elegant modulator that V. alginolyticus employs to switch protein synthesis between the SecDF1/SecDF2 paralogs, consequently enabling it to adapt to salinity change in marine-estuarine environment. The switch mechanism depends on the absence or existence of a translocon force, which serves as an indicator of protein translocation capacity. This mode of regulation can be considered a stress response to the dysfunction of a protein delivery machine (Ishii et al., 2015).

Thus, one of the next questions is whether more RAPs act in various stressful conditions such as heat/cold (temperature) shock, changes to salt concentration or

oxygen level, fluctuation of pH, or viral infection. In the future, we need to integrate high-throughput screening methods into current biochemical and structural analyses on RAPs. For instance, to detect particular patterns of cis-regulatory events in open reading frames by comparing the genome-wide ribosome profiles of bacteria cultured under optimal and stressful conditions.

Although only about 20 RAPs have been discovered so far, it is widely accepted that cis-acting modulators may be more commonly utilized in translation (Ito and Chiba, 2013). Previous ribosome profiling experiments have looked for multiple translation stalling and pause sites in general (Ingolia, Lareau, and Weissman, 2011). However, studies applying conditional ribosome-profiling to identify novel stalling sites that are of regulatory importance are lacking.

Moreover, compared to the bacterial RAPs, fewer eukaryotic RAPs have been characterized; nevertheless, identified eukaryotic RAPs have exhibited distinct biologic outputs to those in bacteria—for example, repression of metabolite biosynthesis and splicing of the RAP mRNA (Ito and Chiba, 2013). Furthermore, ribosome profiling on eukaryotic cells has revealed many functionally unassigned uORFs that may play a regulatory role (Brar and Weissman, 2015). Thus, identifying translated uORFs in vivo under a condition of interest could be one of the future objectives.

3.0.2 Why does Vms1 cut the tRNA?

The translation machinery may encounter any misprocessed translational components that can lead to an aberrantly stalled ribosome with the incompletely synthesized nascent polypeptides. The failure to rescue the ribosome and eliminate the mRNA and nascent polypeptides in time can be proteotoxic and neurodegenerative disease-related (Choe et al., 2016). The rescue mechanism, the RQC pathway, undergoes non-canonical nascent chain extension, i.e., CAT-tailing. However, the puzzle piece of which enzyme is responsible for releasing the nascent chain was only recently revealed, i.e., Vms1 in yeast (ANKZF1 in human) (Verma et al., 2018;

Rendón et al., 2018). This finding is vitally crucial since unlimited CAT-tailing of nuclear-encoded mitochondrial proteins compromises mitochondrial and cellular homeostasis, whereas Vms1 counteracts CAT-tailing by steric hindrance and peptide release (Izawa et al., 2017).

Surprisingly, despite Vms1 VLRF1 adopting a similar fold and motif to eRF1, it does not cut the peptidyl-tRNA at the ester bond like what conventional release factors do. What's more, the here presented 3.4 Å cryo-electron microscopy structure of the native Vms1-60S pullout revealed striking remodeling of the tRNA backbone at the base 73 by Vms1. This position is next to the tRNA CCA-end and thus coincides nicely with the latest biochemical research clarifying the cutting location, which is precisely between base 73 and the CCA-end (Yip et al., 2019).

However, why does Vms1 cut the tRNA instead of performing conventional hydrolysis of the nascent chain? It is reasonable to hypothesize that RQC might force the principal translational components' rechecking by going through the last steps of component biogenesis. Remarkably, the tRNA cut by Vms1/ANKZF1 produces a unique 2,3-cyclic phosphate that differentiates from the canonical tRNA substrate for the addition of the CCA-end. This phosphate must be removed before the rehab by CCA-adding tRNA biogenesis factor, TRNT1 (Yip et al., 2019).

Interestingly, during the investigation of Vms1, a new RQC player was identified, which is the previously described ribosome biogenesis factor Argonaute-binding protein 1 (Arb1). This factor promotes the Vms1 release efficiency by further stabilizing the Vms1-mediated tRNA backbone remodeling. As Arb1 is an ABCF-type ATPase, it might also support the disassociation of Vms1 followed by the cutting. Such moonlighting behavior of translational machinery biogenesis factors may indicate the assumption of rehab checkpoints employed by the RQC pathway, which needs future investigations.

Another intriguing aspect of the RQC pathway is that it had been thought to be eukaryotic specific due to a. the existence of the trans-translation system in bacteria

and b. the principal difference of the input mRNA and the localization of translation. Surprisingly, recently a similar RQC system was discovered in bacteria (Lytvynenko et al., 2019), where the non-canonical extension to the nascent chain is a CA tail instead of CAT, presumably due to CAT tails are highly toxic to non-eukaryotic environments. One of the questions to ask is that why in eukaryotes, such a tail composition was evolved.

Collectively, a novel mechanistic model of Vms1, Rqc2, and Arb1 activities in RQC was proposed, in which nucleolytic Vms1 and Arb1 can terminate Rqc2-dependent CAT-tailing and cooperate in antagonizing CAT-tail-driven mitochondrial toxicity.

References

Agirrezabala, Xabier and Joachim Frank (2009). "Elongation in translation as a dynamic interaction among the ribosome, tRNA, and elongation factors EF-G and EF-Tu". In: *Quarterly Reviews of Biophysics* 42.3, pp. 159–200. ISSN: 0033-5835. DOI: 10.1017/s0033583509990060.

Arenz, Stefan et al. (2014). "Molecular basis for erythromycin-dependent ribosome stalling during translation of the ErmBL leader peptide". In: *Nature Communications* 5.1, p. 3501. DOI: 10.1038/ncomms4501.

Arenz, Stefan et al. (2016). "Structures of the orthosomycin antibiotics avilamycin and evernimicin in complex with the bacterial 70S ribosome". In: *Proceedings of the National Academy of Sciences* 113.27, pp. 7527–7532. ISSN: 0027-8424. DOI: 10.1073/pnas.1604790113.

Becker, Thomas et al. (2012). "Structural basis of highly conserved ribosome recycling in eukaryotes and archaea". In: *Nature* 482.7386, pp. 501–506. ISSN: 0028-0836. DOI: 10.1038/nature10829.

Beckmann, Roland et al. (2001). "Architecture of the Protein-Conducting Channel Associated with the Translating 80S Ribosome". In: *Cell* 107.3, pp. 361–372. ISSN: 0092-8674. DOI: 10.1016/s0092-8674(01)00541-4.

Bengtson, Mario H. and Claudio A. P. Joazeiro (2010). "Role of a ribosome-associated E3 ubiquitin ligase in protein quality control". In: *Nature* 467.7314, pp. 470–473. ISSN: 0028-0836. DOI: 10.1038/nature09371.

Bhushan, Shashi et al. (2010). "-Helical nascent polypeptide chains visualized within distinct regions of the ribosomal exit tunnel". In: *Nature Structural & Molecular Biology* 17.3, pp. 313–317. ISSN: 1545-9993. DOI: 10.1038/nsmb.1756.

Bischoff, Lukas, Otto Berninghausen, and Roland Beckmann (2014). "Molecular Basis for the Ribosome Functioning as an L-Tryptophan Sensor". In: *Cell Reports* 9.2, pp. 469–475. ISSN: 2211-1247. DOI: 10.1016/j.celrep.2014.09.011.

Blanchard, Scott C et al. (2004). "tRNA selection and kinetic proofreading in translation". In: *Nature Structural & Molecular Biology* 11.10, pp. 1008–1014. ISSN: 1545-9993. DOI: 10.1038/nsmb831.

Brandman, Onn and Ramanujan S Hegde (2016). "Ribosome-associated protein quality control". In: *Nature Structural & Molecular Biology* 23.1, pp. 7–15. ISSN: 1545-9993. DOI: 10.1038/nsmb.3147.

Brandman, Onn et al. (2012). "A Ribosome-Bound Quality Control Complex Triggers Degradation of Nascent Peptides and Signals Translation Stress". In: *Cell* 151.5, pp. 1042–1054. ISSN: 0092-8674. DOI: 10.1016/j.cell.2012.10.044.

Brar, Gloria A. and Jonathan S. Weissman (2015). "Ribosome profiling reveals the what, when, where and how of protein synthesis". In: *Nature Reviews Molecular Cell Biology* 16.11, pp. 651–664. ISSN: 1471-0072. DOI: 10.1038/nrm4069.

Brown, Alan et al. (2015). "Structural basis for stop codon recognition in eukaryotes". In: *Nature* 524.7566, pp. 493–496. ISSN: 0028-0836. DOI: 10.1038/nature14896.

Buskirk, Allen R. and Rachel Green (2017). "Ribosome pausing, arrest and rescue in bacteria and eukaryotes". In: *Philosophical Transactions of the Royal Society B: Biological Sciences* 372.1716, p. 20160183. ISSN: 0962-8436. DOI: 10.1098/rstb.2016.0183.

Butkus, Martha E., Lucia B. Prundeanu, and Donald B. Oliver (2003). "Translocon "Pulling" of Nascent SecM Controls the Duration of Its Translational Pause and Secretion-Responsive secA Regulation". In: *Journal of Bacteriology* 185.22, pp. 6719–6722. ISSN: 0021-9193. DOI: 10.1128/jb.185.22.6719-6722.2003.

Chiba, Shinobu, Anne Lamsa, and Kit Pogliano (2009). "A ribosome–nascent chain sensor of membrane protein biogenesis in Bacillus subtilis". In: *The EMBO Journal* 28.22, pp. 3461–3475. ISSN: 1460-2075. DOI: 10.1038/emboj.2009.280.

Chiba, Shinobu et al. (2011). "Recruitment of a species-specific translational arrest module to monitor different cellular processes". In: *Proceedings of the National Academy of Sciences* 108.15, pp. 6073–6078. ISSN: 0027-8424. DOI: 10.1073/pnas.1018343108.

Choe, Young-Jun et al. (2016). "Failure of RQC machinery causes protein aggregation and proteotoxic stress". In: *Nature* 531.7593, pp. 191–195. ISSN: 0028-0836. DOI: 10.1038/nature16973.

Cruz-Vera, Luis Rogelio et al. (2011). "Nascent polypeptide sequences that influence ribosome function". In: *Current Opinion in Microbiology* 14.2, pp. 160–166. ISSN: 1369-5274. DOI: 10.1016/j.mib.2011.01.011.

Defenouillère, Quentin et al. (2013). "Cdc48-associated complex bound to 60S particles is required for the clearance of aberrant translation products". In: *Proceedings of the National Academy of Sciences* 110.13, pp. 5046–5051. ISSN: 0027-8424. DOI: 10.1073/pnas.1221724110.

Defenouillère, Quentin et al. (2016). "Rqc1 and Ltn1 Prevent C-terminal Alanine-Threonine Tail (CAT-tail)-induced Protein Aggregation by Efficient Recruitment of Cdc48 on Stalled 60S Subunits*". In: *Journal of Biological Chemistry* 291.23, pp. 12245–12253. ISSN: 0021-9258. DOI: 10.1074/jbc.m116.722264.

Degnin, C R et al. (1993). "Translational inhibition mediated by a short upstream open reading frame in the human cytomegalovirus gpUL4 (gp48) transcript." In: *Journal of Virology* 67.9, pp. 5514–5521. ISSN: 0022-538X. DOI: 10.1128/jvi.67.9.5514-5521.1993.

Dever, Thomas E. and Rachel Green (2012). "The Elongation, Termination, and Recycling Phases of Translation in Eukaryotes". In: *Cold Spring Harbor Perspectives in Biology* 4.7, a013706. DOI: 10.1101/cshperspect.a013706.

Franckenberg, Sibylle, Thomas Becker, and Roland Beckmann (2012). "Structural view on recycling of archaeal and eukaryotic ribosomes after canonical termination and ribosome rescue". In: *Current Opinion in Structural Biology* 22.6, pp. 786–796. ISSN: 0959-440X. DOI: 10.1016/j.sbi.2012.08.002.

Frank, Joachim and Rajendra Kumar Agrawal (2000). "A ratchet-like inter-subunit reorganization of the ribosome during translocation". In: *Nature* 406.6793, pp. 318–322. ISSN: 0028-0836. DOI: 10.1038/35018597.

Gao, Xiangwei et al. (2015). "Quantitative profiling of initiating ribosomes in vivo". In: *Nature Methods* 12.2, pp. 147–153. ISSN: 1548-7091. DOI: 10.1038/nmeth.3208.

Gong, Feng and Charles Yanofsky (2001). "Reproducing tna Operon Regulation in Vitro in an S-30 System TRYPTOPHAN INDUCTION INHIBITS CLEAVAGE OF TnaC PEPTIDYL-tRNA". In: *Journal of Biological Chemistry* 276.3, pp. 1974–1983. ISSN: 0021-9258. DOI: 10.1074/jbc.m008892200.

— (2002). "Instruction of Translating Ribosome by Nascent Peptide". In: *Science* 297.5588, pp. 1864–1867. ISSN: 0036-8075. DOI: 10.1126/science.1073997.

Gualerzi, Claudio O. and Cynthia L. Pon (2015). "Initiation of mRNA translation in bacteria: structural and dynamic aspects". In: *Cellular and Molecular Life Sciences* 72.22, pp. 4341–4367. ISSN: 1420-682X. DOI: 10.1007/s00018-015-2010-3.

Gumbart, James et al. (2012). "Mechanisms of SecM-Mediated Stalling in the Ribosome". In: *Biophysical Journal* 103.2, pp. 331–341. ISSN: 0006-3495. DOI: 10.1016/j.bpj.2012.06.005.

Heo, Jin-Mi et al. (2010). "A Stress-Responsive System for Mitochondrial Protein Degradation". In: *Molecular Cell* 40.3, pp. 465–480. ISSN: 1097-2765. DOI: 10.1016/j.molcel.2010.10.021.

Heuer, André et al. (2017). "Structure of the 40S–ABCE1 post-splitting complex in ribosome recycling and translation initiation". In: *Nature Structural & Molecular Biology* 24.5, pp. 453–460. ISSN: 1545-9993. DOI: 10.1038/nsmb.3396.

Horinouchi, Sueharu and Bernard Weisblum (1980). "Posttranscriptional modification of mRNA conformation: Mechanism that regulates erythromycin-induced resistance". In: *Proceedings of the National Academy of Sciences* 77.12, pp. 7079–7083. ISSN: 0027-8424. DOI: 10.1073/pnas.77.12.7079.

Ingolia, Nicholas T., Liana F. Lareau, and Jonathan S. Weissman (2011). "Ribosome Profiling of Mouse Embryonic Stem Cells Reveals the Complexity and Dynamics

of Mammalian Proteomes". In: *Cell* 147.4, pp. 789–802. ISSN: 0092-8674. DOI: 10.1016/j.cell.2011.10.002.

Ishii, Eiji et al. (2015). "Nascent chain-monitored remodeling of the Sec machinery for salinity adaptation of marine bacteria". In: *Proceedings of the National Academy of Sciences* 112.40, E5513–E5522. ISSN: 0027-8424. DOI: 10.1073/pnas.1513001112.

Ismail, Nurzian et al. (2012). "A biphasic pulling force acts on transmembrane helices during translocon-mediated membrane integration". In: *Nature Structural & Molecular Biology* 19.10, pp. 1018–1022. ISSN: 1545-9993. DOI: 10.1038/nsmb.2376.

Ito, Koreaki and Shinobu Chiba (2013). "Arrest Peptides: Cis-Acting Modulators of Translation". In: *Annual Review of Biochemistry* 82.1, pp. 171–202. ISSN: 0066-4154. DOI: 10.1146/annurev-biochem-080211-105026.

Izawa, Toshiaki et al. (2017). "Cytosolic Protein Vms1 Links Ribosome Quality Control to Mitochondrial and Cellular Homeostasis". In: *Cell* 171.4, 890–903.e18. ISSN: 0092-8674. DOI: 10.1016/j.cell.2017.10.002.

Jackson, Richard J., Christopher U. T. Hellen, and Tatyana V. Pestova (2010). "The mechanism of eukaryotic translation initiation and principles of its regulation". In: *Nature Reviews Molecular Cell Biology* 11.2, pp. 113–127. ISSN: 1471-0072. DOI: 10.1038/nrm2838.

Joazeiro, Claudio A.P. (2015). "Ribosomal Stalling During Translation: Providing Substrates for Ribosome-Associated Protein Quality Control". In: *Annual Review of Cell and Developmental Biology* 33.1, pp. 1–26. ISSN: 1081-0706. DOI: 10.1146/annurev-cellbio-111315-125249.

Johansson, Magnus et al. (2014). "Sequence-Dependent Elongation Dynamics on Macrolide-Bound Ribosomes". In: *Cell Reports* 7.5, pp. 1534–1546. ISSN: 2211-1247. DOI: 10.1016/j.celrep.2014.04.034.

Kaminishi, Tatsuya et al. (2007). "A Snapshot of the 30S Ribosomal Subunit Capturing mRNA via the Shine-Dalgarno Interaction". In: *Structure* 15.3, pp. 289–297. ISSN: 0969-2126. DOI: 10.1016/j.str.2006.12.008.

Karcher, Annette, Alexandra Schele, and Karl-Peter Hopfner (2008). "X-ray Structure of the Complete ABC Enzyme ABCE1 from Pyrococcus abyssi". In: *Journal of Biological Chemistry* 283.12, pp. 7962–7971. ISSN: 0021-9258. DOI: 10.1074/jbc.m707347200.

Kisselev, Lev, Måns Ehrenberg, and Ludmila Frolova (2003). "Termination of translation: interplay of mRNA, rRNAs and release factors?" In: *The EMBO Journal* 22.2, pp. 175–182. ISSN: 1460-2075. DOI: 10.1093/emboj/cdg017.

Knorr, Alexandra G. et al. (2019). "Ribosome–NatA architecture reveals that rRNA expansion segments coordinate N-terminal acetylation". In: *Nature Structural & Molecular Biology* 26.1, pp. 35–39. ISSN: 1545-9993. DOI: 10.1038/s41594-018-0165-y.

Korostelev, Andrei et al. (2007). "Interactions and dynamics of the Shine–Dalgarno helix in the 70S ribosome". In: *Proceedings of the National Academy of Sciences* 104.43, pp. 16840–16843. ISSN: 0027-8424. DOI: 10.1073/pnas.0707850104.

Korostelev, Andrei et al. (2008). "Crystal structure of a translation termination complex formed with release factor RF2". In: *Proceedings of the National Academy of Sciences* 105.50, pp. 19684–19689. ISSN: 0027-8424. DOI: 10.1073/pnas.0810953105.

Korostelev, Andrei A. (2011). "Structural aspects of translation termination on the ribosome". In: *RNA* 17.8, pp. 1409–1421. ISSN: 1355-8382. DOI: 10.1261/rna.2733411.

Kostova, Kamena K. et al. (2017). "CAT-tailing as a fail-safe mechanism for efficient degradation of stalled nascent polypeptides". In: *Science* 357.6349, pp. 414–417. ISSN: 0036-8075. DOI: 10.1126/science.aam7787.

Kuroha, Kazushige et al. (2018). "Release of Ubiquitinated and Non-ubiquitinated Nascent Chains from Stalled Mammalian Ribosomal Complexes by ANKZF1 and Ptrh1". In: *Molecular Cell* 72.2, 286–302.e8. ISSN: 1097-2765. DOI: 10.1016/j.molcel.2018.08.022.

Lovett, P S and E J Rogers (1996). "Ribosome regulation by the nascent peptide." In: *Microbiological reviews* 60.2, pp. 366–85. ISSN: 0146-0749.

Lytvynenko, Iryna et al. (2019). "Alanine Tails Signal Proteolysis in Bacterial Ribosome-Associated Quality Control". In: *Cell* 178.1, 76–90.e22. ISSN: 0092-8674. DOI: 10.1016/j.cell.2019.05.002.

Lyumkis, Dmitry et al. (2014). "Structural basis for translational surveillance by the large ribosomal subunit-associated protein quality control complex". In: *Proceedings of the National Academy of Sciences* 111.45, pp. 15981–15986. ISSN: 0027-8424. DOI: 10.1073/pnas.1413882111.

Matheisl, Sarah et al. (2015). "Structure of a human translation termination complex". In: *Nucleic Acids Research* 43.18, pp. 8615–8626. ISSN: 0305-1048. DOI: 10.1093/nar/gkv909.

McNicholas, Paul, Reza Salavati, and Donald Oliver (1997). "Dual regulation of Escherichia coli secA translation by distinct upstream elements11Edited by M. Gottesman". In: *Journal of Molecular Biology* 265.2, pp. 128–141. ISSN: 0022-2836. DOI: 10.1006/jmbi.1996.0723.

Melnikov, Sergey et al. (2012). "One core, two shells: bacterial and eukaryotic ribosomes". In: *Nature Structural & Molecular Biology* 19.6, pp. 560–567. ISSN: 1545-9993. DOI: 10.1038/nsmb.2313.

Nakatogawa, Hitoshi and Koreaki Ito (2001). "Secretion Monitor, SecM, Undergoes Self-Translation Arrest in the Cytosol". In: *Molecular Cell* 7.1, pp. 185–192. ISSN: 1097-2765. DOI: 10.1016/s1097-2765(01)00166-6.

— (2002). "The Ribosomal Exit Tunnel Functions as a Discriminating Gate". In: *Cell* 108.5, pp. 629–636. ISSN: 0092-8674. DOI: 10.1016/s0092-8674(02)00649-9.

Nielson, Jason R. et al. (2017). "Sterol Oxidation Mediates Stress-Responsive Vms1 Translocation to Mitochondria". In: *Molecular Cell* 68.4, 673–685.e6. ISSN: 1097-2765. DOI: 10.1016/j.molcel.2017.10.022.

Noble, C. G. and H. Song (2008). "Structural studies of elongation and release factors". In: *Cellular and Molecular Life Sciences* 65.9, pp. 1335–1346. ISSN: 1420-682X. DOI: 10.1007/s00018-008-7495-6.

Noller, Harry F. et al. (2002). "Translocation of tRNA during protein synthesis". In: *FEBS Letters* 514.1, pp. 11–16. ISSN: 0014-5793. DOI: 10.1016/s0014-5793(02)02327-x.

Peske, Frank, Marina V. Rodnina, and Wolfgang Wintermeyer (2005). "Sequence of Steps in Ribosome Recycling as Defined by Kinetic Analysis". In: *Molecular Cell* 18.4, pp. 403–412. ISSN: 1097-2765. DOI: 10.1016/j.molcel.2005.04.009.

Pisarev, Andrey V., Christopher U.T. Hellen, and Tatyana V. Pestova (2007). "Recycling of Eukaryotic Posttermination Ribosomal Complexes". In: *Cell* 131.2, pp. 286–299. ISSN: 0092-8674. DOI: 10.1016/j.cell.2007.08.041.

Pisareva, Vera P et al. (2011). "Dissociation by Pelota, Hbs1 and ABCE1 of mammalian vacant 80S ribosomes and stalled elongation complexes". In: *The EMBO Journal* 30.9, pp. 1804–1817. ISSN: 1460-2075. DOI: 10.1038/emboj.2011.93.

Preis, Anne et al. (2014). "Cryoelectron Microscopic Structures of Eukaryotic Translation Termination Complexes Containing eRF1-eRF3 or eRF1-ABCE1". In: *Cell Reports* 8.1, pp. 59–65. ISSN: 2211-1247. DOI: 10.1016/j.celrep.2014.04.058.

Ramu, Haripriya, Alexander Mankin, and Nora Vazquez-Laslop (2009). "Programmed drug-dependent ribosome stalling". In: *Molecular Microbiology* 71.4, pp. 811–824. ISSN: 1365-2958. DOI: 10.1111/j.1365-2958.2008.06576.x.

Rendón, Olga Zurita et al. (2018). "Vms1p is a release factor for the ribosome-associated quality control complex". In: *Nature Communications* 9.1, p. 2197. DOI: 10.1038/s41467-018-04564-3.

Seidelt, Birgit et al. (2009). "Structural Insight into Nascent Polypeptide Chain–Mediated Translational Stalling". In: *Science* 326.5958, pp. 1412–1415. ISSN: 0036-8075. DOI: 10.1126/science.1177662.

Shao, Sichen and Ramanujan S. Hegde (2016). "Target Selection during Protein Quality Control". In: *Trends in Biochemical Sciences* 41.2, pp. 124–137. ISSN: 0968-0004. DOI: 10.1016/j.tibs.2015.10.007.

Shao, Sichen et al. (2015). "Structure and Assembly Pathway of the Ribosome Quality Control Complex". In: *Molecular Cell* 57.3, pp. 433–444. ISSN: 1097-2765. DOI: 10.1016/j.molcel.2014.12.015.

Shen, Peter S. et al. (2015). "Rqc2p and 60S ribosomal subunits mediate mRNA-independent elongation of nascent chains". In: *Science* 347.6217, pp. 75–78. ISSN: 0036-8075. DOI: 10.1126/science.1259724.

Shine, J. and L. Dalgarno (1974). "The 3-Terminal Sequence of Escherichia coli 16S Ribosomal RNA: Complementarity to Nonsense Triplets and Ribosome Binding Sites". In: *Proceedings of the National Academy of Sciences* 71.4, pp. 1342–1346. ISSN: 0027-8424. DOI: 10.1073/pnas.71.4.1342.

Shivakumar, A G et al. (1980). "Posttranscriptional regulation of an erythromycin resistance protein specified by plasmic pE194". In: *Proceedings of the National Academy of Sciences* 77.7, pp. 3903–3907. ISSN: 0027-8424. DOI: 10.1073/pnas.77.7.3903.

Shoemaker, Christopher J., Daniel E. Eyler, and Rachel Green (2010). "Dom34:Hbs1 Promotes Subunit Dissociation and Peptidyl-tRNA Drop-Off to Initiate No-Go Decay". In: *Science* 330.6002, pp. 369–372. ISSN: 0036-8075. DOI: 10.1126/science.1192430.

Sohmen, Daniel et al. (2015). "Structure of the Bacillus subtilis 70S ribosome reveals the basis for species-specific stalling". In: *Nature Communications* 6.1, p. 6941. DOI: 10.1038/ncomms7941.

Song, Haiwei et al. (2000). "The Crystal Structure of Human Eukaryotic Release Factor eRF1—Mechanism of Stop Codon Recognition and Peptidyl-tRNA Hydrolysis". In: *Cell* 100.3, pp. 311–321. ISSN: 0092-8674. DOI: 10.1016/s0092-8674(00)80667-4.

Tran, Joseph R., Lauren R. Tomsic, and Jeffrey L. Brodsky (2011). "A Cdc48p-associated Factor Modulates Endoplasmic Reticulum-associated Degradation, Cell Stress, and Ubiquitinated Protein Homeostasis*". In: *Journal of Biological Chemistry* 286.7, pp. 5744–5755. ISSN: 0021-9258. DOI: 10.1074/jbc.m110.179259.

Tsuboi, Tatsuhisa et al. (2012). "Dom34:Hbs1 Plays a General Role in Quality-Control Systems by Dissociation of a Stalled Ribosome at the 3 End of Aberrant mRNA". In: *Molecular Cell* 46.4, pp. 518–529. ISSN: 1097-2765. DOI: 10.1016/j.molcel.2012.03.013.

Vazquez-Laslop, Nora, Celine Thum, and Alexander S. Mankin (2008). "Molecular Mechanism of Drug-Dependent Ribosome Stalling". In: *Molecular Cell* 30.2, pp. 190–202. ISSN: 1097-2765. DOI: 10.1016/j.molcel.2008.02.026.

Verma, Rati et al. (2013). "Cdc48/p97 promotes degradation of aberrant nascent polypeptides bound to the ribosome". In: *eLife* 2, e00308. DOI: 10.7554/elife.00308.

Verma, Rati et al. (2018). "Vms1 and ANKZF1 peptidyl-tRNA hydrolases release nascent chains from stalled ribosomes". In: *Nature* 557.7705, pp. 446–451. ISSN: 0028-0836. DOI: 10.1038/s41586-018-0022-5.

Voss, N.R. et al. (2006). "The Geometry of the Ribosomal Polypeptide Exit Tunnel". In: *Journal of Molecular Biology* 360.4, pp. 893–906. ISSN: 0022-2836. DOI: 10.1016/j.jmb.2006.05.023.

Weixlbaumer, Albert et al. (2008). "Insights into Translational Termination from the Structure of RF2 Bound to the Ribosome". In: *Science* 322.5903, pp. 953–956. ISSN: 0036-8075. DOI: 10.1126/science.1164840.

Wethmar, Klaus (2014). "The regulatory potential of upstream open reading frames in eukaryotic gene expression". In: *Wiley Interdisciplinary Reviews: RNA* 5.6, pp. 765–768. ISSN: 1757-7012. DOI: 10.1002/wrna.1245.

Wilson, Daniel N, Stefan Arenz, and Roland Beckmann (2016). "Translation regulation via nascent polypeptide-mediated ribosome stalling". In: *Current Opinion in Structural Biology* 37, pp. 123–133. ISSN: 0959-440X. DOI: 10.1016/j.sbi.2016.01.008.

Wilson, Daniel N and Roland Beckmann (2011). "The ribosomal tunnel as a functional environment for nascent polypeptide folding and translational stalling".

In: *Current Opinion in Structural Biology* 21.2, pp. 274–282. ISSN: 0959-440X. DOI: 10.1016/j.sbi.2011.01.007.

Wilson, Daniel N. and Jamie H. Doudna Cate (2012). "The Structure and Function of the Eukaryotic Ribosome". In: *Cold Spring Harbor Perspectives in Biology* 4.5, a011536. DOI: 10.1101/cshperspect.a011536.

Yip, Matthew C. J. et al. (2019). "Mechanism for recycling tRNAs on stalled ribosomes". In: *Nature Structural & Molecular Biology* 26.5, pp. 343–349. ISSN: 1545-9993. DOI: 10.1038/s41594-019-0211-4.

Yonashiro, Ryo et al. (2016). "The Rqc2/Tae2 subunit of the ribosome-associated quality control (RQC) complex marks ribosome-stalled nascent polypeptide chains for aggregation". In: *eLife* 5, e11794. DOI: 10.7554/elife.11794.

Zavialov, A. V. et al. (2002). "Donor strand complementation mechanism in the biogenesis of non-pilus systems". In: *Molecular Microbiology* 45.4, pp. 983–995. ISSN: 1365-2958. DOI: 10.1046/j.1365-2958.2002.03066.x.

List of Abbreviations

aa-tRNA	**A**mino**a**cyl-tRNA
ABCE	**A**TP-**B**inding **C**assette sub-family **E**
Arb1	**Ar**gonaute-**B**inding protein 1
A-site	**A**minoacyl site
ATP	**A**denosine **Tri**phosphate
B. subtilis	***B**acillus subtilis*
CAT tail	**C**-terminal **A**lanine **T**hreonine tail
e (prefix)	**E**ukaryotic
E. coli	***E**scherichia coli*
EF	**E**longation **F**actor
E-site	**E**xit site
ES	**E**xpension segment
FeS	**Iron**-**S**ulfur cluster
GTP	**G**uanosine **Tri**phosphate
IF	**I**nitiation **F**actor
mRNA	**m**essenger RNA
NBD	**N**ucleotide-**B**inding **D**omain
P-site	**P**eptidyl site
PTC	**P**eptidyl-**T**ransferase **C**enter
RAP	**R**ibosome **A**rrest **P**eptide
RF	**R**elease **F**actor
RRF	**R**ibosome **R**ecycling **F**actor
r-proteins	**r**ibosomal proteins

RQC	**R**ibosome-associated protein **Q**uality **C**ontrol
rRNA	**r**ibosomal RNA
S (unit)	**S**vedberg unit
SD	**S**hine Dalgarno
tRNA	**t**ransfer RNA
VemP	*Vibrio* **E**xport **M**onitoring **P**olypeptide
V. alginolyticus	***V**ibrio alginolyticus*
VLRF1	**V**ms1-**L**ike **R**elease **F**actor 1
Vms1	**V**alosin-containing protein/Cdc48-associated **M**itochondrial **S**tress-responsive 1

Acknowledgements

I had an unforgettable adventure through my Ph.D. time. Firstly, I appreciate Prof. Roland Beckmann accepting me to his lab despite my distinct previous background (eels vs. ribosomes). His supportive and optimal spirit encouraged me in a long way.

Secondly, I want to thank Prof. Daniel N. Wilson for the closest collaboration and all-angle support and Prof. Gunnar von Heijne for the smooth collaboration and prompt replies. I want to express my most profound respect to Prof. Walter Neupert and thank him for the lovely experience of working with him. I shall never forget your spirit towards science, excellence, and responsibilities. Sadly, you left us before the publication of the Vms1 paper.

Next, I cannot thank enough Dr. Thomas Becker for correcting this dissertation and kindly providing me a place to sleep in the long winter of 2018 and summer of 2019. Without his support, the revision of the Vms1 paper would not be successful. Likewise, I want to thank Dr. Toshiaki Izawa and Matthias Thoms for their extreme excellence in completing the Vms1 story together. I also want to thank Dr. Renuka Kudva. She is not only a fantastic collaborator but also a good friend willing to support me anytime. I will never forget the generous help from Dr. Daniel Sohmen, Dr. Yui Yamashita, Dr. Jacobo Marino, and Dr. Sarah Matheisl in my early times, especially Dr. Daniel Sohmen, for guiding me through the EM project pipeline. I thank the "office squad" for the timely help in data processing, including Clara, Andre, Lukas, and Michi. I cherish my colleagues/friends, like Yui, Jen, Clara, Alex, Jingdong, Shuangshuang, Vivek, Anne, Maxi, and Petar, who created the best research atmosphere and laughter. Moreover, I am grateful to have all of you for discussing science together, Katharina, Hanna, Tsai, Marko, Lukas, Stephan, and so on.

Furthermore, many thanks to Dr. Otto Berninghausen, Susi Rieder, and Charlotte Ungewickell for their dispensable care of the microscopy sample preparation

and data collection; to Heidi Sieber, Andera Gilmozzi, Joana Musial for the excellent job they provide to the lab; and to everyone on the 3rd floor of the Gene Center, especially the ones on the same corridor side of us, for the enjoyable working environment.

My experience through the Graduate school of Quantitative Biosciences Munich (QBM) is precious. QBM offered me cross- and interdisciplinary education and broadened my perspectives in biophysics and bioinformatics, and allowed me to attend international conferences, valuable workshops, and enjoyable yearly retreats where I earned multiple first awards. I want to give my special thanks to our beloved QBM speaker Prof. Ulrike Gaul, who sadly left us too soon. You not only accepted me to the Ph.D. program but also kindly suggested which lab to join. QBM would look different without you. I also want to thank Dr. Michael Mende and Mara Kieke for helping me with enormous things when I moved to Munich, and lecturers Dr. Filiz Civril and Dr. Markus Hohle for giving excellent biochemistry, biophysics, and bioinformatics courses.

Finally, I appreciate the unconditional love and support in all possible ways from my parents, grandparents, and my dear husband.